Formation and Evolution of Galactic Structures Using Gas and Stellar Kinematics

by

Takafumi Tsukui

Dissertation

submitted to the Department of Astronomical Science

in partial fulfillment of the requirements for the degree of

Doctor of Philosophy

The Graduate University for Advanced Studies, SOKENDAI

January 2022

Acknowledgments

First of all, I would like to greatly thank my main supervisor, Prof. Satoru Iguchi for his tremendous supports and encouragement during my entire Ph.D. program. The success of this study would not have been possible without insightful discussions with him. His continuous encouragement also gave me the confidence to overcome any challenges.

I am also grateful to Hiroshi Nagai and Yuichi Matsuda, who took a lot of time to discuss with me the current understanding and framework of galaxy formation, for their valuable discussions and constructive advice. I would like to greatly thank my collaborators, Kyoko Onishi, Marc Sarzi, Boris Nedelchev, Dieu Nguyen and Michele Cappellari, Junichi Baba for their kind supports and constructive guidance for my work. I also thank Fornax3D team for kindly giving me the stellar kinematics data of NGC1380.

I would also thank Daisuke Iono, Kenichi Tadaki, Tomonari Michiyama, Misato Fukagawa, Gonzalez Alvaro, Masayuki Tanaka, Masa Imanishi, Junko Ueda, Koichiro Nakanishi, Kazuya Saito, Takuma Izumi, Seiji Fujimoto for having scientific discussions with me and giving me valuable feedback for my study.

This thesis would not have been completed without the tremendous support of referees, Prof. Masayuki Tanaka, Prof. Masami Ouchi, Prof. Junichi Baba, Prof.

Kentaro Nagamine, and Prof. Kotaro Kouno. I would like to thank them all for valuable feedback and constructive discussions.

Outside the work, I would like to thank all the students who spent with me in the ALMA building at NAOJ, especially, Yuta Kato, Kazuki Sato, Tako Ishikawa, Ko hosokawa, Jinshi Sai, Masayuki Yamaguchi, Ikki Mitsuhashi, Ryota Ikeda, and Kosuke Namekata.

Finally, I would like to thank my parents and a younger brother and sister for their unconditional supports. This thesis is dedicated to my parents because I cannot thank them enough for their supports in all aspects.

Data analysis were in part carried out on common use data analysis computer system at the Astronomy Data Center, ADC, of the National Astronomical Observatory of Japan. This study was partially supported by Overseas Travel Fund for Students (2019) of the Department of Astronomical Science, the Graduate University for Advanced Studies, SOKENDAI.

Abstract

Galaxies have internal structures such as a central black hole, bulge, disk, and stellar and dark matter halos. Identifying these structures across cosmic history and measuring their physical parameters (e.g., size and detailed mass distribution) are crucial in revealing galaxies' past formation and evolution history, as each structure is suggested to drive and regulate the galaxy evolution dynamically. To accurately derive the mass distribution of galaxies, it is essential to have both (1) high-resolution observations required to derive central mass distribution and (2) wide-field observations covering the radius where dark matter starts to dominate. The recent development of ALMA allows us to obtain gas kinematics with sufficient angular resolution to measure the central black hole mass and stellar mass distribution separately in nearby galaxies and mass distribution of galaxies at high redshift galaxies at a redshift of >4.

No spectroscopic imaging instrument can simultaneously archive such a high resolution and wide field of view for a nearby galaxy (i.e., z ~ 0). NGC 1380 has a wealthy data set that includes: stellar kinematics measured from the atomic absorption features in a stellar continuum obtained by Multi-Unit Spectroscopic Explorer (MUSE) on the Very Large Telescope (VLT); and stellar surface brightness distribution obtained by Advanced

Camera for Survey(ACS) on Hubble Space Telescope (HST); and high-resolution CO(2-1) molecular gas kinematics by Band 6 receiver on ALMA. The stellar kinematics and surface brightness data cover the large area of the galaxy out to 120 arcsec. In contrast, the high-resolution molecular gas kinematics allows us to accurately trace the central mass distribution. We identified galactic structures: a central black hole, bulge, disk, stellar, and dark matter halos in the early-type galaxy NGC 1380 and accurately measured these mass distributions, exploiting and combining these archival data. We first directly measured the black hole mass in NGC1380, which was consistent with the known black hole and host galaxies scaling relations. Our measurements of each galactic structure in NGC1380 locate the galaxy's disk in the stable regime in the bar-like instability, which may explain the absence of significant substructure in the disk in NGC1380.

With the developed methods and experiences, we also investigated galactic structures more than 12 billion years ago, which was an unexplored epoch for detailed galactic structure. The luminous [CII] emission from an extreme star formation and ALMA's high sensitivity allow us to obtain the most detailed [CII] gas kinematics for an unlensed, hyper luminous infrared galaxy (HyLIRG) at redshift 4.4, BRI 1335-0417. Analyzing the spatially resolved [CII] gas and dust kinematics, we have identified a rotating disk, a central compact structure like a bulge, and spiral structures on the disk in BRI 1335-0417. HyLIRGs are thought to be formed mainly through major mergers, in which we expect the presence of highly disturbed structures. But surprisingly, the dust-obscured internal structures revealed in this study are similar to those of a spiral disk galaxy. This may give us a clue to the detailed formation scenario of HyLIRGs and massive galaxies in cosmic history.

Contents

1 Introduction

1.1 Formation of Galactic Structures in ΛCDM universe

1.1.1 General Introduction

Galaxies are fundamental building blocks of the universe, and mostly through their electromagnetic radiation, we can probe the evolution of matter distribution in the universe. A key result in galaxy formation is the evidence of dark matter, which was

revealed for the first time by an observation of a galaxy cluster in the 1930s (Zwicky, 1933) and galaxy rotation curves in the 1970s (Rubin et al., 1978, 1980). The most accepted standard model of the universe is the one in which dark energy and dark matter are the major components of the universe, the universe initially experiences an exponential expansion (i.e., Big Bang), and initial density fluctuations amplified due to self-gravity and grow hierarchically by merging. This model reproduces successfully the large-scale distribution of observed galaxies, as well as the cosmic microwave background radiation (Bennett et al., 2014). The evolution of the matter distribution over a broader range of cosmic epoch has still been explored with advanced observational instruments, testing the current standard model of the universe (Ouchi et al., 2018).

On the other hand, at the scale of individual galaxies, we can observe common distinct structures: a bulge; a flat, extended rotating disk; non-axisymmetric bar structures and spiral arms on the disk; and stellar and dark matter haloes in the outer part of the galaxy. When and how these structures were formed is one of the major questions in modern astronomy. Although several scenarios have been proposed so far, gaining a full understanding is challenging because of the incompleteness of observations (we can only observe a particular galaxy from a given direction at a given moment in time) and the number of baryonic processes involved. The main focus of this paper is to explore the formation and evolutionary processes of galaxies through the dynamics of these structures, which allow us to recover their distribution and kinematics with currently available rich but ultimately limited information. In this chapter, we will summarise the current understanding of the galactic structures. The main references for this chapter are Binney & Tremaine (2008), Longair (2008) and Mo et al. (2010).

1.1.2 Galaxy Formation in Dark Matter Halo

Zwicky (1933) showed for the first time the evidence of dark matter by analyzing the motion of individual galaxies in the Coma cluster. The kinetic energy far exceeds the gravitational potential energy expected from visible matter: stars, gas, and dust in the cluster, suggesting the presence of invisible matter is necessary for the cluster to be gravitationally bound. A few decades later, more evidences of dark matter were found in galaxies. Rubin et al. (1978, 1980) found the flat rotation velocity ($v_{rot} \propto$ const) of neutral hydrogen (HI) in galaxies even at the radius well beyond the visible part of galaxies. This is contrary to the expectation that the rotational velocity decreases with the radius to the power of 1/2 (i.e., Keplerian rotation $v_{rot} \propto 1/r^{\frac{1}{2}}$) under the assumption that the galaxy is composed of only visible matter, which manifests the presence of invisible matter enveloping the galaxy. These results are exemplified by Figure 1.1.

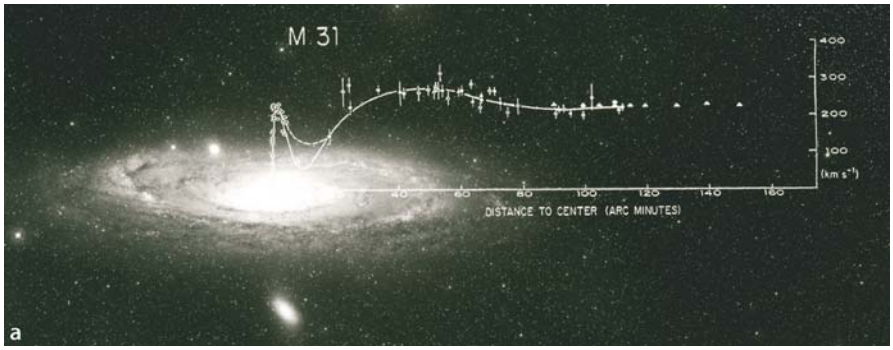

Figure 1.1: The rotation curve for nearby spiral galaxy M31 as presented in Longair (2008) with courtesy of Dr. Vera Rubin. Constant rotation velocity can be seen at the radius well beyond the visible region of the galaxy, which manifests the existence of an extended dark matter halo in this galaxy.

Although dark matter is still hypothetical and its physical nature is not yet known, it is widely accepted that the cold (move slow compared to the speed of light) and dark (have a very small cross-section for electromagnetic interaction and interact mainly

through gravity) hypothetical matter play an essential role in the formation and evolution of galaxies (Peebles, 1982; Blumenthal et al., 1984), with the development of the ΛCDM model of the universe,

In the cosmic epoch prior to the recombination, baryons in the plasma state are strongly coupled to photons. The growth of density fluctuations of baryons was suppressed by the pressure of photons (i.e., silk damping; Silk 1968), while dark matter can already grow density fluctuations in this period. As the temperature of the thermal equilibrium decrease gradually, baryons become neutral and decouple from photons (i.e., recombination) and then condense into the gravitational potential well of dark matter, forming the first stars and galaxies in the center of the halo. In addition, Ostriker & Peebles (1973) showed that, in the absence of dark matter, disk galaxies are subject to a bar instability due to strong differential rotation and that a dark matter halo is necessary for the stable disk galaxy.

Navarro et al. (1997) show that the density profile of the dark matter halos found in N body numerical simulation can be described by the following double power law profile (which is called NFW profile after Navarro, Frenk and White), independent of the mass of the halo, the spectrum of the initial density fluctuations, and the cosmological parameters;

$$\rho(r) = \frac{4\rho_{\rm s}}{(r/r_{\rm s})(1+r/r_{\rm s})^2}, \tag{1.1}$$

where $r_{\rm s}$ is the scale radius, and $\rho_{\rm s}$ is the density at the scale radius. This function contains two free parameters, $r_{\rm s}$ and $\rho_{\rm s}$. Navarro et al. (1997) found that there are tight correlation between halo mass $M_{200} = 200\rho_{\rm c}\frac{4}{3}\pi r_{200}^3$ and concentration of the halo $c \equiv r_{200}/r_{\rm s}$ [1] so that we can consider this formula to have one free parameter, as the

[1] radius r_{200} is such that the average density of the halo surrounded by that radius is 200 times the critical density of the universe $\rho_{\rm c}$.

enclosed mass within r is given by

$$M_{\rm DM}(<r) = 16\pi\rho_s r_s^3 \left[\ln\left(1+\frac{r}{r_s}\right) - \frac{r/r_s}{1+r/r_s}\right] \tag{1.2}$$

The detailed distribution of dark matter is the most fundamental parameter of galaxies, but it has not yet been established, and continuous research is being conducted. While the total mass (baryon + dark matter) distribution of the galaxy can be derived using stellar kinematics and the rotational curve of the gas, measuring the detailed distribution of dark matter requires the precise mass distribution of baryon (stars, gas, and dust). Deriving the stellar mass distribution from the stellar surface brightness distribution is a major uncertainty (Courteau & Dutton, 2015) since the exact conversion factor (i.e., stellar mass to luminosity ratio) depends on the initial mass function, star formation history, and ages, which are still difficult to completely recover with the current instruments. Furthermore, in a more realistic galaxy formation scenario with baryon physics, the outflow of gas due to star formation and AGN would inject energy into the dark matter particle via gravity, and the density profile of dark matter would be flatter than the NFW model (Navarro et al., 1996; Mashchenko et al., 2008; Pontzen & Governato, 2012). In competition with this effect, gas inflows into the galactic center will lead to a centrally concentrated dark matter profile (adiabatic contraction; Blumenthal et al. 1986; Cautun et al. 2019). It has also been suggested that there is a substructure in the Milky Way halo (Bonaca et al., 2019). Even in the Milky Way, the detailed density distribution of dark matter is still not well understood (Hattori et al., 2020). In order to disentangle these effects and to understand the interaction history between dark matter and baryons across cosmic history, it is essential to explore the methodology to derive dark matter with higher accuracy and to derive and compare dark matter distribution for

a sample of galaxies with various masses and morphologies (Wasserman et al., 2018).

1.1.3 Galaxy's Morphologies and Hubble Classification

Galaxies have a great variety of shapes and forms. Hubble classified the galaxies according to their morphology as shown in Figure 1.2 (Hubble, 1936). This morphological classification, called a tuning fork diagram, shows a continuous sequence of elliptical galaxies on the left and spiral galaxies on the right. The spiral galaxies are separated like tuning forks into ordinary spirals and barred spiral galaxies with bar-like structures. These morphological classifications are correlated with the overall physical properties of the galaxy (e.g., color and gas content; Roberts & Haynes 1994). As van den Bergh (1998) emphasized that the original Hubble classification was for intrinsically bright galaxies, it has been updated to include the majority of less luminous galaxies (e.g., Kormendy 1982; van den Bergh 1998). The idea of the Hubble sequence remains as an essential galaxy classification, and nowadays, machine learning is being used to classify a huge number of galaxy photometric images (e.g., Vega-Ferrero et al. 2021; Dieleman et al. 2015).

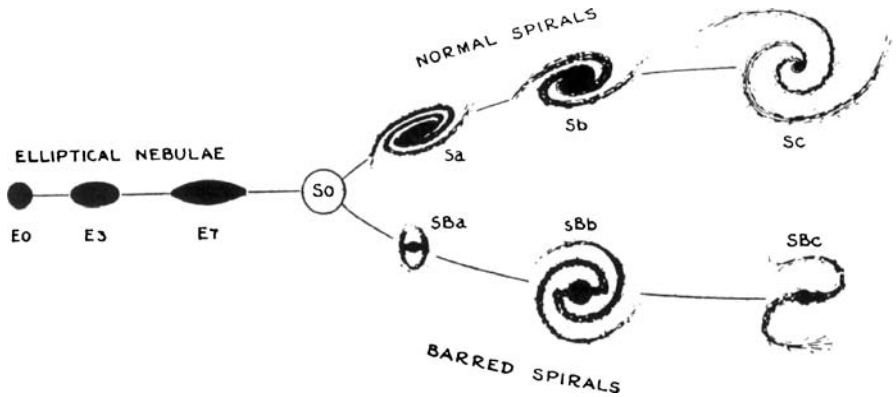

Figure 1.2: Hubble's morphological classification of galaxies as presented in *The Realm of the Nebulae* (Hubble, 1936)

Elliptical Galaxies

Elliptical galaxies have a featureless, elliptical luminosity distribution and are thought to have an ellipsoidal structure in three dimensions. They are classified according to their observed flattening, labeled as a letter E followed by $10 \times (a - b)/a$, where a and b are the major and minor axes, respectively. Galaxies, flatter than E7, are called lenticular galaxies (S0) because they all show disk and bulge structures. Surface brightness of elliptical galaxies are well described by de Vaucouleurs's $r^{1/4}$ law as a special case ($n = 4$) of the Sérsic profile (Sersic, 1968)

$$I(R) = I_{\rm e} \exp\left\{-b_n \left[\left(\frac{R}{R_e}\right)^{1/n} - 1\right]\right\}, \tag{1.3}$$

where $R_{\rm e}$ is the radius within which half of the total luminosity enclosed, and b_n is the value such that $\Gamma(2n) = 2\gamma(2n, b_n)$ (Γ is the gamma function and $\gamma(2n, x)$ is the incomplete gamma function; Graham & Driver 2005). Elliptical galaxies are typically supported by the random motion of stars rather than their rotation motions. Galaxy mergers are likely to play a role in forming elliptical galaxies by transporting stars' angular momentum outward. Recent numerical calculations have shown that merging in a gas-rich disk does not effectively remove angular momentum (e.g., Hopkins et al. 2009) and gas accretion leading to the reformation of disk (Zeng et al., 2021). Therefore, AGN feedback might be necessary to remove the gas from the galaxy before merging and to prevent the cooling of new gas from accretion to form the disk-less elliptical galaxies (Somerville & Davé, 2015).

Spiral Galaxies

Spiral galaxies have distinct structures: stellar bulge; a flat, extended rotating disk consisting of stars, gas, and dust; non-axisymmetric features on the disk such as spiral arms and bars as the schematic picture is shown in Figure 1.3. Spiral galaxies are classified as either "normal" spiral galaxies (S) or barred spiral galaxies (SB), depending on the presence of a bar structure. S and SB galaxies are further classified in a sequence from a (through b) to c as the spiral becomes more open and the relative size of the bulge or bar to the disk decreases (Figure 1.2). These structures are thought to have a complex influence on each other (Fujii et al., 2018), and the expected correlation is confirmed quantitatively (central bulge mass vs. arm pitch angle Davis et al. 2018a). The Hubble classification (see Figure 1.2) is regarded as a continuous sequence based on the relative importance of the bulge and disk as the sequence goes accordingly, from elliptical galaxies at the leftmost, which have a dominant bulge and no disk, through intermediate S0 galaxies, which have both a bulge and a featureless disk, to spiral galaxies at the rightmost, which have dominant disk and smaller bulge, with spiral arms on the disk. Therefore, disks, bulges, arm and bar structures are the fundamental structures of galaxies, and a brief review of these structures will be given in the next subsection.

1.1.4 Galactic Structures

Disk

The galactic disk is a flat structure supported by rotation, consisting of stars, gas, and dust. The disk typically shows an exponential surface brightness and density distribution (Gadotti, 2009).

$$I(R) = I_0 \exp(-R/R_d), \tag{1.4}$$

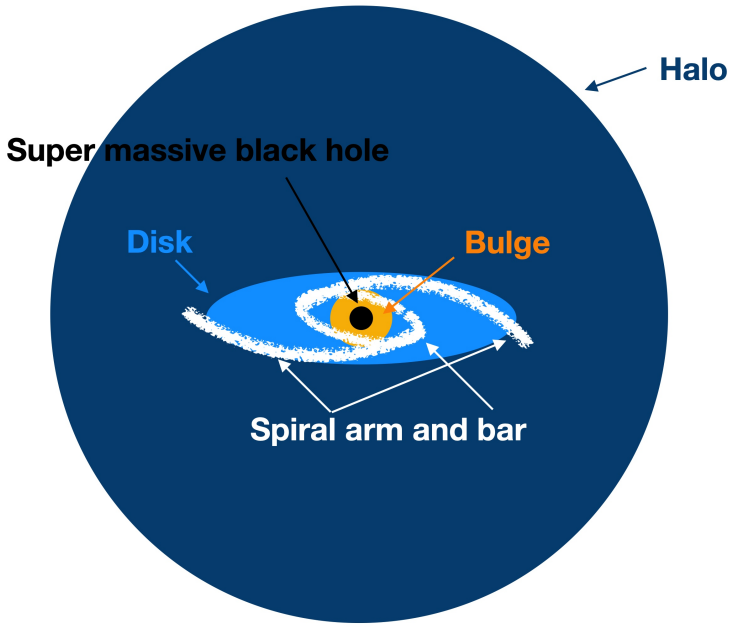

Figure 1.3: Schematic picture of typical structures of spiral galaxies.

where R_d is a disk-scale radius and I_0 is the central surface brightness. The flat galactic disk structure is naturally expected to form where an isolated gas cloud collapses under the dark matter potential, conserving its initial angular momentum. The gas releases energy outside via radiative cooling, while the angular momentum is conserved. The gas particles subsequently archive the lowest energy state with the initial angular momentum conserved, namely, a rotating disk where the angular momentum of all gas particles is aligned in one direction. A stellar disk may form as some fraction of the gas disk cools further and then collapse to form stars by local disk instability (Toomre, 1964; Goldreich & Lynden-Bell, 1965). Afterward, dust disk may form as dust component being ejected from asymptotic-giant-branch stars and core-collapse supernovae (Gall et al., 2011). In an attempt to reproduce the galactic structure using numerical simulations, disk formation and its physical properties (e.g., degree of rotation over random velocity,

clumpiness, gas, and stellar fraction) are sensitive to sub-grid model assumed (For a review, see Somerville & Davé 2015). Therefore, observationally constraining the disk characteristics and formation time is essential to test and improve our galaxy formation models.

Bulge

Although the bulge refers to a dense stellar cluster in the center of the galaxy, there are several types of bulges that show different structures, possibly due to different formation scenarios. One type of bulge is called a classical bulge, which has a surface brightness typically described by Sérsic profile $n > 2$, and a structure supported by pressure due to random motion rather than rotation, similar to elliptical galaxies (Sérsic n $\sim$ 4, dispersion dominated system). It is thought to have been formed by violent galaxy mergers. The other type is called "pseudo bulge" which has a flat, rotationally supported spheroidal structure with the surface brightness typically described by Sérsic profile of $n < 2$. "Pseudo bulges" are thought to have been formed by secular processes, such as gas inflow to the center by angular momentum transport driven by non-axisymmetric structures like a bar. Classical bulges lie on the same $\langle\mu_e\rangle$-r_e relation of the elliptical galaxies while "pseudo bulge" not (Figure 1.4). As exemplified by this plot, differences in the detailed distribution of structures may tell us different formation histories, and measuring detailed structures can provide clues to reveal the galaxy formation history (Gadotti, 2009). See also Athanassoula (2005); Kormendy & Kennicutt (2004) for a review of bulge types and their possible formation scenarios.

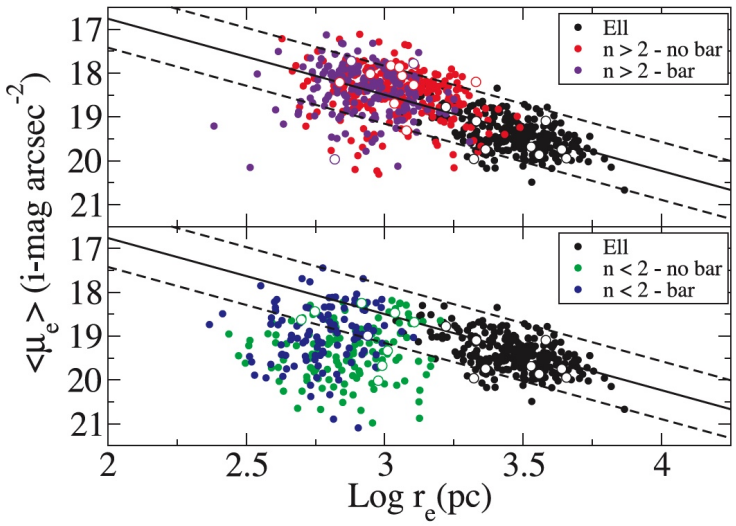

Figure 1.4: $\langle\mu_e\rangle$-r_e relation for $n > 2$ bulges, typically occupied by classical bulge (top) and $n > 2$ bulge, typically occupied by pseudo bulge (bottom) as presented in (Gadotti, 2009). Note that the $n > 2$ bulges lie on the same relation of the elliptical galaxies while $n < 2$ bulges deviate from the relation.

Black Hole

The gravitationally dominant region of a black hole in a galaxy (i.e., sphere of influence $r_g \equiv GM_{BH}/\sigma_*^2$, where σ_* is stellar velocity dispersion of the galaxy nucleus [2] is typically small $\sim 1 - 100$pc (Kormendy & Ho, 2013), and its detection and confirmation requires high spatial and spectral resolutions. The mass of black holes has been measured in various ways since the 1990s due to the progress of observation technology. Despite the significant order of difference between the gravitational radius of a black hole and the

[2]In zeroth-order approximations (assuming spherical symmetry and neglecting the detailed stellar mass distribution), r_g can be derived as follows. From the Virial theorem, the kinetic energy and potential energy of a stellar system in equilibrium are related by $\Omega + 2K = 0$. We can find radius r where the potential energy due to the central black hole dominates over (or is numerically less than) the potential energy of galaxies (stars) by $-GMM_{BH}/r < \Omega = -2K \sim -M\sigma_*^2$, leading to $r < GM_{BH}/\sigma_*^2 \equiv r_g$. This nice explanation can be found at https://physics.stackexchange.com/questions/578665/formula-of-black-hole-gravitational-sphere-of-influence.

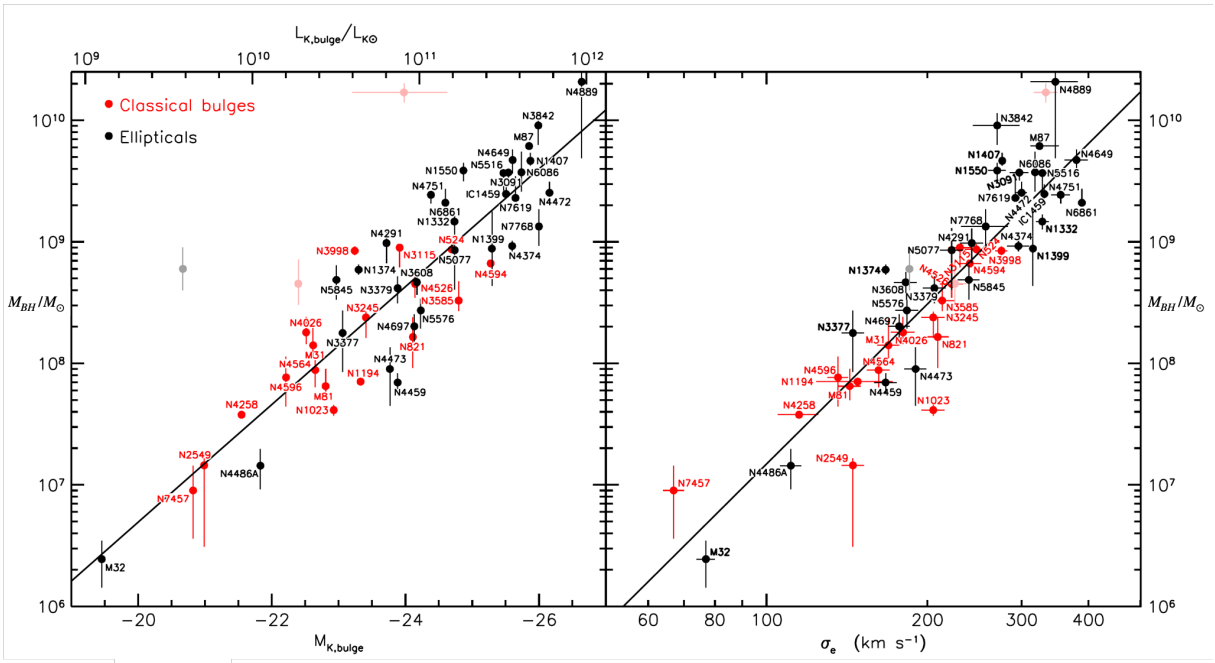

Figure 1.5: Scaling relation of black hole mass $M_{\rm BH}$ with K-band absolute magnitude $M_{\rm K,bulge}$ (left) and luminosity $L_{\rm K,bulge}$ and velocity dispersion σ_e (right) for classical bulges (red points) and elliptical galaxies (black points) as presented in Kormendy & Ho (2013). The lines are least-square fits excluding extreme outliers (transparent points).

physical scale of the galactic structure [3], a strong correlation is suggested between the mass of the central black hole and properties of the host galaxy (e.g., the velocity dispersion and mass of the classical bulge, see Figure 1.5 and Kormendy & Ho 2013 for a review). Thus, the galaxy evolution is thought to be closely related to the central black hole formation. Several scenarios have been proposed for the co-evolution of the black hole and its host galaxies (e.g., feedback between galaxies and AGN; Fabian 2012 and hierarchical galaxy mergers; Jahnke & Macciò 2011), but they have not yet been fully understood. To distinguish various co-evolution scenarios, it is essential to accurately measure both the mass of central black hole and host galactic structures, constraining

[3]Typical bulge size is several hundred pc to a few kpc, while typical disk size is a few to several kpc (e.g. Gadotti 2009).

accurate measurements of the slope, intrinsic scatter, and shape of these correlations (Kormendy & Ho, 2013).

Spiral Arms and Bar

Spiral arms serve as the main site of star formation and shape the properties of the disk. Disk galaxies can violently change shape in a short period of time due to galaxy mergers. On the other hand, non-axisymmetric structures such as spiral arms and bars drive the long-term evolution of galactic disks through scattering and migration of stars as well as radial transport of the angular momentum of the gas (through its gravitational torque), driving gas inflow to the center and nuclear starburst, leading to the growth of bulges and feeding central black hole. However, understanding the evolution and formation of spiral structures is one of the long-standing questions in astronomy. "Stationary Spiral Density Wave" (Lin & Shu, 1964) is a hypothetical theory based on the belief that the shape of the spiral arms remains unchanged throughout their long-lived duration (i.e., stationary spiral structure hypothesis). The proposed theory does not consider spiral arms as a solid material but as regions of excess density with gas and stars moving through. Although the static spiral density wave theory provides a useful framework to study spiral arms, numerical simulation has not yet reproduced such stable spiral density waves. Recently, rather dynamic pictures have been proposed, in which the spiral arms are transient and recurrently reform Baba et al. (2013); Baba (2015), induced by tidal interactions, and/or driven by a bar (see Dobbs & Baba 2014 for a review.) To reveal whether the spiral arms are stable, tidally induced transient, or dynamic structure which is repeatedly generated and destroyed, it is important to compare the distribution and kinematics of the stars and gas with the numerical simulation Dobbs & Baba (2014) resembling the typical properties of galaxies at the given cosmic epoch such as gas fraction and accretion rates.

1.2 Dynamical Model of Galaxies

The construction of a dynamical model of galaxies is essential to recover the 3d structure and kinematics of galaxies and to estimate the underlying gravitational potential (mass distribution of galaxies) from observations that are limited in principle (line of sight velocity distribution and luminosity distribution which are projected in the sky). In this section, we summarize the commonly used methods for building dynamical models for stars and gas. The main reference for this section is Binney & Tremaine (2008).

1.2.1 Modeling Stellar Systems

The gravity is a long-range force ($\propto r^{-2}$, where r is the distance from the mass). For stellar systems with homogeneous number density, the force on a single star is contributed from the most distant location (the net force from stars in a volume at a distance of r is $\propto r$). In a galaxy, the time scale (i.e., relaxation time $t_{\rm relax}$), after which the cumulative effects of encounters between two stars significantly change the orbit of stars, is larger than the age of the universe. Therefore, when we model galaxies, we can ignore the gravitational interactions between individual stars (e.g., collisionless) and approximate the gravitational potential set by an ensemble of stars as smooth potentials rather than peaked potentials created by myriads of individual stars. In the following, we summarize the basic framework for modeling collisionless stellar systems.

Distribution Function and Observables

When modeling collisionless stellar systems, a useful concept is the distribution function f, where $f(\mathbf{x}, \mathbf{v}, t)d^3\mathbf{x}d^3\mathbf{v}$ is the probability that a star exists in a given volume of phase

space at a given time t. By definition, f is normalized as

$$\int d^3\mathbf{x}d^3\mathbf{v}f(\mathbf{x},\mathbf{v},t) = 1 \tag{1.5}$$

From the condition of probability conservation in phase space, the time evolution of f satisfies the equation (i.e., collisionless Boltzmann equation),

$$\frac{\partial f}{\partial t} + \mathbf{v}\cdot\frac{\partial f}{\partial \mathbf{x}} - \frac{\partial \Phi}{\partial \mathbf{x}}\cdot\frac{\partial f}{\partial \mathbf{v}} = 0 \tag{1.6}$$

under the Hamiltonian $H = \frac{1}{2}v^2 + \Phi(\mathbf{x},t)$ with gravitational potential $\Phi(\mathbf{x},t)$, in terms of Cartesian coordinates. Constraining the distribution function f and gravitational potential Φ from observable is one of the main objectives in galactic dynamics.

In relating the distribution function f to the observable, the probability of finding a star per unit volume regardless of its velocity $\nu(\mathbf{x})$ is

$$\nu(\mathbf{x}) \equiv \int \mathrm{d}^3\mathbf{v}f(\mathbf{x},\mathbf{v}). \tag{1.7}$$

$\nu(\mathbf{x})$ is related to luminosity density distribution by $j(\mathbf{x}) = L\nu(\mathbf{x})$ where L is total luminosity of stars under the assumption that a single population of stars makes up the stellar system (also related to mass density distribution by $\rho_{\mathrm{star}}(\mathbf{x}) = M_{\mathrm{star}}\nu(\mathbf{x})$ where M is the total mass of stars). The surface brightness of galaxies which can be obtained by photometric observation, is

$$I(\mathbf{x}_\perp) = \int dx_\parallel j(\mathbf{x}), \tag{1.8}$$

where $x_\parallel$ is components of $\mathbf{x}$ parallel to the line of sight and $\mathbf{x}_\perp$ is perpendicular to the line of sight. Estimating the 3 dimensional (3D) luminosity density $j(\mathbf{x})$ from

the observed 2D surface brightness $I(\mathbf{x}_\perp)$ is important task for modeling galaxies. However there is no unique solution $j(\mathbf{x})$ for a given $I(\mathbf{x}_\perp)$ (e.g. Rybicki 1987; Franx 1988), except for spherical system and axisymmetric system with edge-on configuration (Kochanek & Rybicki, 1996; Gerhard & Binney, 1996). A simple and robust method for giving one possible solution is to expand a photometric stellar image in multiple two dimensional (2D) Gaussian functions, and then de-project each 2D Gaussian function into a 3D Gaussian functions using the mathematical property that 2D projection of 3D Gaussian function is a 2D Gaussian function (see Bendinelli 1991 for an original conceptualization; Monnet et al. 1992 for generalization for non-spherical case; and Emsellem et al. 1994a and Cappellari 2002 for further development and its efficient implementation).

The line-of-sight velocity distribution $F(\mathbf{x}_\perp, v_\parallel)$ which can be obtained by spectroscopic observation is

$$F(\mathbf{x}_\perp, v_\parallel) = \frac{\int dx_\parallel d^2\mathbf{v}_\perp f(\mathbf{x}, \mathbf{v})}{\int dx_\parallel d^3\mathbf{v} f(\mathbf{x}, \mathbf{v})}. \tag{1.9}$$

Mean velocity and velocity dispersion are useful quantities to quantify the line-of-sight velocity distribution and compare the model with the observed data, which are respectively related to the distribution function f as,

$$\langle v_\parallel \rangle \equiv \int \mathrm{d}v_\perp F(\mathbf{x}_\perp, v_\parallel) = \frac{\int \mathrm{d}x_\parallel \mathrm{d}^3\mathbf{v} v_\parallel f(\mathbf{x}, \mathbf{v})}{\int \mathrm{d}x_\parallel \mathrm{d}^3\mathbf{v} f(\mathbf{x}, \mathbf{v})}; \tag{1.10}$$

$$\begin{aligned} \sigma_\parallel^2 &\equiv \int \mathrm{d}v_\parallel (v_\parallel - \langle v_\parallel \rangle)^2 F(\mathbf{x}_\perp, v_\parallel) \\ &= \frac{\int \mathrm{d}x_\parallel \mathrm{d}^3\mathbf{v} (v_\parallel - \langle v_\parallel \rangle)^2 f(\mathbf{x}, \mathbf{v})}{\int \mathrm{d}x_\parallel \mathrm{d}^3\mathbf{v} f(\mathbf{x}, \mathbf{v})}. \end{aligned} \tag{1.11}$$

Gravitational Potentials

Gravitational poential $\Phi(\mathbf{x})$ and mass density distribution $\rho(\mathbf{x})$ is related by Poisson's equation;

$$\nabla^2\Phi = 4\pi G\rho. \tag{1.12}$$

This linear equation allows us to consider the potential of the entire galaxy Φ_{Galaxy} as the sum of the gravitational potential created by the density distribution of each component of the galaxy.

$$\Phi_{\text{Galaxy}} = \Phi_{\text{BH}} + \Phi_{\text{star}} + \Phi_{\text{gas}} + \Phi_{\text{dust}} + \Phi_{\text{dark matter}} + \text{etc.} \tag{1.13}$$

Schwarzschild's Orbit-based Method

Schwarzschild's method was first devised by Schwarzschild (1979) as a way to show the existence of stable systems with a triaxial density distribution under its self-gravity as suggested by the observed luminosity distribution of elliptical galaxies. In this subsection, we will briefly describe the basic idea of this method, which is widely used to construct a dynamical model (equivalently finding f) under the assumed gravitational potential, which reproduces the observed surface brightness and line of sight velocity distributions (e.g., Van Den Bosch et al. 2008).

First, the space occupied by the galaxy is divided into K cells (jth cell has volume V_j). Then, we integrate a large number N of orbits under an assumed gravitational potential for a time T much longer than the crossing time with a range of initial conditions of the orbits to ensure that the set of orbits samples all the phase space that the galaxy would occupy. Finally, orbits are weighted and added together to reproduce the observed surface brightness of the galaxy and the velocity distribution in the line of sight. The

weighting w_i (> 0) for ith orbit is optimized to reproduce observables, for example, the luminosity density ν_j in jth cell;

$$0 = \Delta_j \equiv \nu_j - L \sum_{i=1}^{N} w_i p_{i,j}, \tag{1.14}$$

where $p_{i,j}$ is the fraction of time for which the i-th orbit spend in the jth cell to the total orbit integration time T. N-dimensional vector $\mathbf{w}$ can be found by quadratic programming by maximizing the objective function $\phi(\mathbf{w}) = -\chi^2$, where χ^2 describes the difference between the model and the observed line of sight velocity distribution at various positions of the sky.

Although Schwarzshild's method gives full generality for representing distribution functions f, it has much larger degrees of freedom N than constraints imposed by observation as each orbit has a free weight parameter w_i. As a result, there are delicate problems: the resulting confidence interval is unrealistically small (Magorrian, 2006; Vasiliev & Valluri, 2019); and f is not unique for a given condition. In order to avoid this problem, we need some regularization methods (Lipka & Thomas, 2021), which are under active investigation and development. Moreover, it is computationally demanding as we must compute a sufficiently large number of orbits for a possible range of gravitational potentials. Therefore, to investigate a wide range of possible shapes of the gravitational potential with an increased number of parameters, the modeling method based on the Jeans equation, which we will discuss in the following subsection, is often used rather than the computationally expensive Schwarzschild's methods.

Jean's Equation-based Method

As seen above, the distribution function cannot be entirely constrained by observables and is not uniquely determined. In this subsection, we introduce a method that does not recover the distribution function but instead estimates the moment of the distribution function directly related to the observables.

For simplicity, we consider the case where the galaxy is axisymmetric and static ($\frac{\partial f}{\partial t} = 0$, $\frac{\partial f}{\partial \phi} = 0$). In cylindrical coordinates, the collisionless Boltzmann equation 1.6 becomes (Binney & Tremaine 2008, equation 4.12)

$$v_R \frac{\partial f}{\partial R} + v_z \frac{\partial f}{\partial z} + \left(\frac{v_\phi^2}{R} - \frac{\partial \Phi}{\partial R} \right) \frac{\partial f}{\partial v_R} - \frac{\partial \Phi}{\partial z} \frac{\partial f}{\partial v_z} - \frac{v_R v_\phi}{R} \frac{\partial f}{\partial v_\phi} = 0. \tag{1.15}$$

Multiplying by v_R and v_z, and integrating over all velocity components, we obtain Jeans equations (Jeans, 1922; Cappellari, 2008)

$$\begin{aligned} \frac{\nu\langle v_R^2\rangle - \nu\langle v_\phi^2\rangle}{R} + \frac{\partial\left(\nu\langle v_R^2\rangle\right)}{\partial R} + \frac{\partial(\nu\langle v_R v_z\rangle)}{\partial z} &= -\nu \frac{\partial \Phi}{\partial R} \\ \frac{\nu\langle v_R v_z\rangle}{R} + \frac{\partial\left(\nu\langle v_z^2\rangle\right)}{\partial z} + \frac{\partial(\nu\langle v_R v_z\rangle)}{\partial R} &= -\nu \frac{\partial \Phi}{\partial z}, \end{aligned} \tag{1.16}$$

with the notation

$$\nu\langle v_k v_j\rangle \equiv \int v_k v_j f d^3\mathbf{v}. \tag{1.17}$$

Assuming that the potential is known, the Jeans equations relate four functions, and for these equations to be closed, at least two additional functions of (R,z) are needed. v_R, v_z, $\langle v_R v_z\rangle$ can be fully specified in terms of $\theta_{\rm ellipse}$ and $q_{\rm ellipse}$, which characterize the velocity dispersion ellipse as follows: $\theta_{\rm ellipse}$ is the angle between the major axis of the ellipse and the equatorial plane, and $q_{\rm ellipse}$ is the axial ratio of the ellipse,

$$\tan 2\theta_{\text{ellipse}} = \frac{2\langle v_R v_z \rangle}{\langle v_R^2 \rangle - \langle v_z^2 \rangle}, \tag{1.18}$$

$$q^2 = \frac{\langle v_R^2 \rangle + \langle v_z^2 \rangle - \sqrt{\left(\langle v_R^2 \rangle - \langle v_z^2 \rangle\right)^2 + 4\langle v_R v_z \rangle^2}}{\langle v_R^2 \rangle + \langle v_z^2 \rangle + \sqrt{\left(\langle v_R^2 \rangle - \langle v_z^2 \rangle\right)^2 + 4\langle v_R v_z \rangle^2}}. \tag{1.19}$$

Cappellari et al. (2007) found that the shape of the velocity dispersion ellipsoid in fast-rotators (galaxies which have significant angular momentum, e.g., disk galaxy) is (i) spherically aligned within the effective radius and (ii) the axial ratio depends on the polar angle and is flattened along z-direction at the axis of symmetry and the equatorial plane (where the density is maximum). See the qualitative description of velocity ellipsoids of real galaxies in the meridional plane (R, z) in Figure 1.6. From these observations, it may be reasonable to assume that the ellipse of the overall velocity dispersion of galaxies is flattened along the z-axis direction and aligned on the equatorial planes (Cappellari, 2008).

Assuming the velocity ellipsoid aligned with the cylindrical coordinates ($\theta_{\text{ellipse}} = 0$, thus $\langle v_R v_z \rangle = 0$ and $\langle v_R^2 \rangle = b\langle v_z^2 \rangle$), Cappellari (2008) provides the efficient (single numerical quadrature) solutions of equation 1.16 (cylindrically-aligned Jeans Anisotropic Modelling method JAM_{cyl}; Cappellari 2008);

$$\begin{aligned} \nu\overline{v_z^2}(R, z) &= \int_z^\infty v \frac{\partial \Phi}{\partial z} \mathrm{d}z \\ \nu\overline{v_\phi^2}(R, z) &= b\left[R\frac{\partial\left(\nu\overline{v_z^2}\right)}{\partial R} + \nu\overline{v_z^2}\right] + Rv\frac{\partial \Phi}{\partial R} \end{aligned} \tag{1.20}$$

The second velocity moment projected in the line of sight $\langle v_{\text{los}^2} \rangle$ is

$$\Sigma\langle v_{\rm los}^2\rangle = \int_{-\infty}^{\infty} \left\{ \nu\langle v_z^2\rangle \cos^2 i + \left(\nu\langle v_R^2\rangle \sin^2\phi + \nu\langle v_\phi^2\rangle \cos^2\phi \right) \sin^2 i \right\} {\rm d}x_\parallel, \tag{1.21}$$

where Σ is normalized surface brightness, $I(\mathbf{x}_\perp)/L$ of stars. To avoid confusion, note again that (R, ϕ, z) denote the galaxy coordinate where z axis is normal to the galactic plane, while $(\mathbf{x}_\perp, x_{\parallel})$ denote the sky coordinate where $x_\parallel$ is along the line of sight. Inclination i is defined as the angle between the vector normal to the galactic plane (z axis) and the line of sight ($x_\parallel$ axis). $\langle v_{\rm los}^2\rangle$ can be directory compared to the observable $\sqrt{\langle v_\parallel\rangle^2 + \sigma_\parallel^2}$.

The assumption that the velocity dispersion ellipse is aligned with the cylindrical coordinate in the disk plane is expected to be violated, especially at the significant height above the disk plane. This is because the motion of the star only under the plane-parallel potential can be described by oscillatory motion in vertical and radial directions in addition to the circular motion (i.e., epicyclic motions). Stellar motion in the bulge and halo regions is dominated by a near-spherical potential. In such a potential, the orbit of a star is nearly on a plane determined by its angular momentum with random direction. Thus the velocity dispersion ellipse is expected to be spherically aligned. Recent observations of Milky Way stars by Gaia (Gaia Collaboration, 2018) found that the velocity ellipse is approximated as being aligned with the spherical coordinates in halo region (Wegg et al., 2019) and disk region (Hagen et al., 2019; Everall et al., 2019). Motivated by these observations and expectations, Cappellari (2020) presented an efficient general solution of the axisymmetric Jeans equations under the assumption of the velocity ellipsoid being aligned to the spherical coordinates (spherically-aligned Jeans Anisotropic Modelling method $\rm JAM_{sph}$; Cappellari 2020).

For convenience, we also briefly summarize the formula and solution of Jeans equation under the assumption of the spherically aligned velocity ellipsoid and axial symmetry ($\partial\Phi/\partial\phi = \partial f/\partial\phi = 0$) (Cappellari, 2020, JAM$_{\rm sph}$). To begin with, the collisionless Boltzmann equation 1.6 can be written in spherical coordinates as (Binney & Tremaine 2008, equation 4.14)

$$\begin{aligned} 0 =& v_r \frac{\partial f}{\partial r} + \frac{v_\theta}{r}\frac{\partial f}{\partial \theta} + \left(\frac{v_\phi^2 + v_\theta^2}{r} - \frac{\partial \Phi}{\partial r}\right)\frac{\partial f}{\partial v_r} \\ &+ \left(\frac{v_\phi^2}{\tan\theta} - v_r v_\theta - \frac{\partial \Phi}{\partial \theta}\right)\frac{\partial f}{\partial v_\theta} - \frac{v_\phi}{r}\left(v_r + \frac{v_\theta}{\tan\theta}\right)\frac{\partial f}{\partial v_\phi}. \end{aligned} \tag{1.22}$$

Multiplying equation 1.22 by v_r and by v_θ and then integrating over all velocities, we obtain two Jeans equations in spherical coordinates (de Zeeuw et al. 1996)

$$\begin{aligned} \frac{\partial(\nu\langle v_r^2\rangle)}{\partial r} + \frac{1}{r}\left[\frac{\partial(\nu\langle v_r v_\theta\rangle)}{\partial\theta} + 2\nu\langle v_r^2\rangle - \nu\langle v_\theta^2\rangle - \nu\langle v_\phi^2\rangle + \frac{\nu\langle v_r v_\theta\rangle}{\tan\theta}\right] &= -\nu\frac{\partial\Phi}{\partial r} \\ r\frac{\partial(\nu\langle v_r v_\theta\rangle)}{\partial r} + \frac{\partial(\nu\langle v_\theta^2\rangle)}{\partial\theta} + 3\nu\langle v_r v_\theta\rangle + \frac{\nu\langle v_\theta^2\rangle - \nu\langle v_\phi^2\rangle}{\tan\theta} &= -\nu\frac{\partial\Phi}{\partial\theta}. \end{aligned} \tag{1.23}$$

with the notation 1.17. By assuming the spherically aligned velocity ellipsoid ($\langle v_r v_\theta\rangle = 0$), and introduction of the anisotropy parameter $\beta = 1 - \frac{\langle v_\theta^2\rangle}{\langle v_r^2\rangle}$ which parametrizes the ratio between $\langle v_\theta^2\rangle$ and $\langle v_r^2\rangle$. Jeans equations 1.23 become (e.g. Bacon et al. 1983)

$$\begin{aligned} \frac{\partial(\nu\langle v_r^2\rangle)}{\partial r} + \frac{(1+\beta)\nu\langle v_r^2\rangle - \nu\langle v_\phi^2\rangle}{r} &= -\nu\frac{\partial\Phi}{\partial r} \\ (1-\beta)\frac{\partial(\nu\langle v_r^2\rangle)}{\partial\theta} + \frac{(1-\beta)\nu\langle v_r^2\rangle - \nu\langle v_\phi^2\rangle}{\tan\theta} &= -\nu\frac{\partial\Phi}{\partial\theta}. \end{aligned} \tag{1.24}$$

Eliminating $\nu\langle v_\phi^2\rangle$ between two equations yields a linear first order partial differential equation for $\nu\langle v_r^2\rangle$,

$$\frac{(1-\beta)\tan\theta}{r}\frac{\partial(\nu\langle v_r^2\rangle)}{\partial\theta} - \frac{2\beta\nu\langle v_r^2\rangle}{r} - \frac{\partial(\nu\langle v_r^2\rangle)}{\partial r} = \Psi(r,\theta) \tag{1.25}$$

where

$$\Psi(r,\theta) \equiv \nu(r,\theta) \times \left(\frac{\partial \Phi}{\partial r} - \frac{\tan\theta}{r} \frac{\partial \Phi}{\partial r} \right). \tag{1.26}$$

Under the boundary condition that $\langle v_r^2 \rangle = 0$ as $r \to \infty$, the explicit solution of equation 1.25 is

$$\begin{aligned} \nu\langle v_r^2 \rangle(r,\theta) &= \int_r^\infty \left(\frac{r'}{r}\right)^{2\beta} \Psi\left(r',\theta'\right) \mathrm{d}r' \\ \theta' &= \arcsin\left[\left(\frac{r'}{r}\right)^{\beta-1} \sin\theta \right] \end{aligned} \tag{1.27}$$

After $\langle v_r^2 \rangle = 0$ is obtained, $\nu\langle v_\phi^2 \rangle$, $\nu\langle v_\theta^2 \rangle$ can also be derived as

$$\nu\langle v_\phi^2 \rangle(r,\theta) = (1-\beta)\left[\nu\langle v_r^2 \rangle + \frac{\partial\left(\nu\langle v_r^2 \rangle\right)}{\partial\theta} \tan\theta \right] + \nu \frac{\partial \Phi}{\partial \theta} \tan\theta \tag{1.28}$$

By definition, $\langle v_\theta^2 \rangle$ can be derived as well,

$$\langle v_\theta^2 \rangle = (1-\beta)\langle v_r^2 \rangle. \tag{1.29}$$

Finally, projecting from the spherical coordinate (the coordinate with $\theta = 0$ on the axis of symmetry) to observer coordinate ($x_\parallel$ is aligned with line of sight) and integrating over the line of sight, we obtain the second moment velocity moment $\langle v_{\mathrm{los}}^2 \rangle$, which can be compared with the observable $\sqrt{\langle v_\parallel \rangle^2 + \sigma_\parallel^2}$, as

$$\begin{aligned} \Sigma\langle v_{los}^2 \rangle(\mathbf{x}_\perp) = \int_{-\infty}^{\infty} [&\langle v_r^2 \rangle(\sin\theta \sin\phi \sin i + \cos\theta \cos i)^2 + \langle v_\theta^2 \rangle(\cos\theta \sin\phi \sin i - \sin\theta \cos i)^2 \\ &+ \langle v_\phi^2 \rangle \cos^2\phi \sin^2 i] \mathrm{d}x_\parallel \end{aligned} \tag{1.30}$$

where the inclination i is defined as the angle between z axis ($\theta = 0$) aligned with axis of symmetry and $x_\parallel$ parallel to the line of sight.

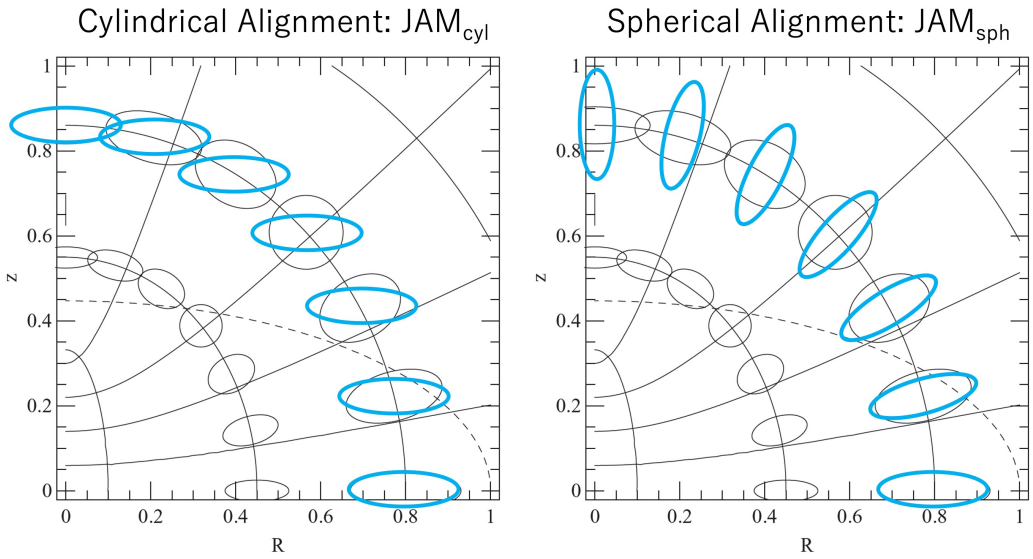

Figure 1.6: comparison of two alignments of velocity ellipsoid (blue ellipses) typically assumed to solve Jeans equation: cylindrical alignment (left) and spherical alignment (right). Black ellipses show qualitative descriptions of velocity ellipsoid for fast rotator galaxies. The black dashed line denotes the contour of the typical stellar luminosity density. The solid black line shows the prolate spheroidal coordinates. Cylindrical alignment can mimic the typical velocity ellipsoid near the disk plane and symmetry axis (z-axis). However, it cannot reproduce the expected spherical alignment near the galactic center and halo region, where the shape of gravitational potential is close to spherical due to the bulge, central black hole, and dark matter halo. The spherical alignment can reproduce the typical velocity ellipsoid near the disk and the expected spherical alignment near the Galactic center and halo region. Figure is adopted from Cappellari (2008).

1.2.2 Modeling Gas Dynamics

In galaxies, cold gas takes a thin disk configuration as the lowest energy state with conserved angular momentum. Cold molecular and atomic gas typically has small velocity dispersion ($\lessapprox$ 10 km s^{-1}; Mogotsi et al. 2015) compared to the rotation velocity and is on nearly circular orbits. For gas disks for which this thin disk approximations are valid, the

rotational velocity $V_{\rm rot}(R)$ of the gas at R is approximated to the circular velocity [4] $V_{\rm circ}(R)$ which directly links to the gravitational potential via $V^2_{\rm rot}(R) \sim V^2_{\rm circ}(R) = -R\frac{\partial\Phi}{\partial R}$. The line of sight velocity distribution $V_{\parallel}(x, y)$ on the sky coordinate (x, y) for the disk which has inclination i and position angle Γ can be described by

$$V_{\parallel}(x, y) = V_{\rm sys} - V_{\rm rot}(R)\cos\left(\text{atan2}(y/x) + \Gamma\right)\sin(i), \tag{1.31}$$

where atan2 is 2-argument arctangent function which gives the angle in radians between the positive x axis and the ray to the point (x,y) and $V_{\rm sys}$ is systemic velocity. All parameters $V_{\rm sys}$, $V_{\rm rot}(R)$, i and Γ can be sufficiently recovered from the data (2D line-of-sight velocity distribution $V_{\parallel}(x, y)$) typically obtained by interferometric observation at radio to sub-millimeter wavebands or IFU observation at optical to infrared wavebands. If the gravitational potential is spherically symmetric, enclosed mass $M(R)$[5] and density profile $\rho(R)$ can be derived from the rotational velocity as (i.e. Newton's second theorem).

$$V^2_{\rm rot}(R) \sim V^2_{\rm circ}(R) = -R\frac{\partial\Phi(R)}{\partial R} = \frac{M(R)G}{R} = \frac{G\int_0^R 4\pi R^2\rho(R)dR}{R} \tag{1.32}$$

If the gravitational potential deviates from the spherical symmetry, the rotational velocity for a given enclosed mass, depends on the 3D structure and shape of the potential (Noordermeer, 2008; Binney & Tremaine, 2008). Figure 1.7 compared the circular velocity due to an infinitely thin exponential disk[6] and the spherical mass distribution with the same enclosed mass. The velocity difference around a peak is about 15%. If the

[4] Circular velocity is defined to be the speed of a test particle in a circular orbit

[5] total mass enclosed within radius R

[6] given by the freeman's equation (Freeman, 1970): $v^2_{\rm disk}(r) = 4G\Sigma_0 R_d y^2[I_0(y)K_0(y) - I_1(y)K_1(y)]$, where $y = r/(2R_d)$. I_0, K_0, I_1 and K_1 are modified Bessel functions.

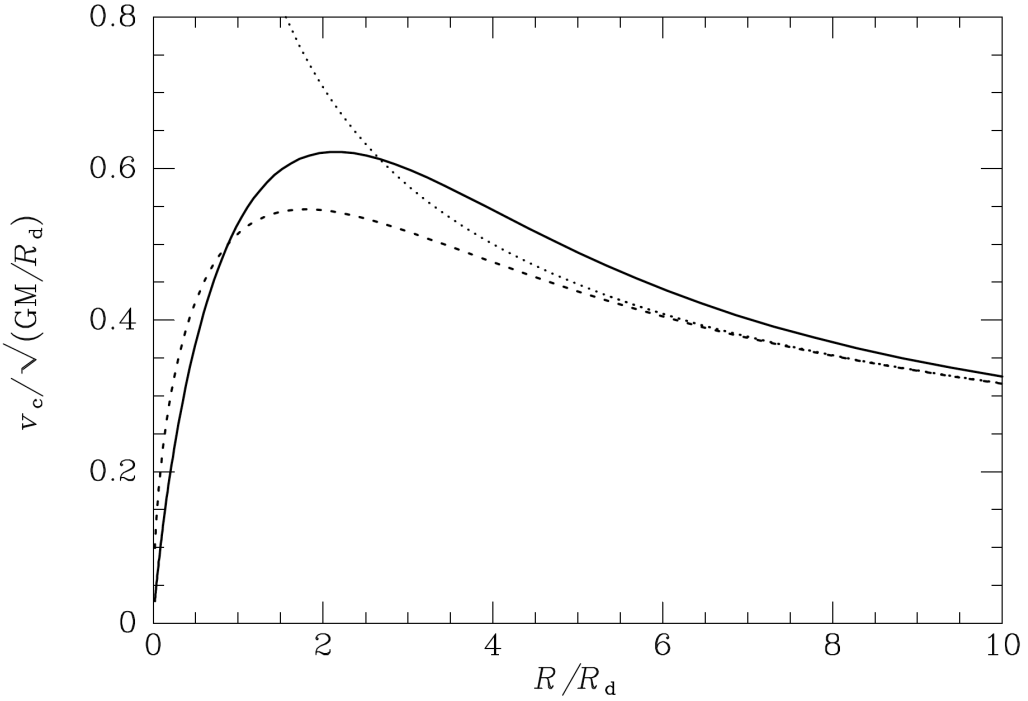

Figure 1.7: Circular velocities for exponential disk (solid line), spherical mass distribution with the same enclosed mass (dashed line) as the exponential disk and point mass with the same total mass(dotted line), as presented in Binney & Tremaine (2008)

deviation from spherical symmetry is not large (minor to major axis ratio of greater than 0.5), the difference can be negligible (Sofue et al., 2009).

1.3 The Problems and Challenges Addressed by This Thesis

We have summarized our understanding of the diverse morphology of the galaxies observed (e.g., Hubble sequence) and the internal structure of galaxies that form the basis for the morphological classification: bulges, disks, spiral, and bar structures. In addition to those visible structures, galaxies have formed and are embedded in a dark

matter halo, which dominates the mass of galaxies and has a significant impact on galactic dynamics. The dynamics of galaxies are governed by the gravity of the internal structures of the galaxy, each of which is suggested to drive or regulate the galaxy evolution. For example, flat disk structures can be gravitationally unstable to serve as the main site for star formation and form bar and spiral structures, while the dark matter halo and bulge structures are suggested to stabilize the disk and suppress the spiral and bar formation (Ostriker & Peebles, 1973; Efstathiou et al., 1982; **?**). Developed bar and spiral structures act as gravitational torques, transporting gas and stars to the center of the galaxy, which leads to central star formation and bulge growth (Athanassoula, 1992; Wada & Habe, 1992). The disk-bulge fraction seems to dynamically control the shape of the spiral via determining the shear rate, the degree of differential rotation, suggested by observations (Seigar et al., 2006; Davis et al., 2019) and numerical simulations (Fujii et al., 2018). Therefore, as galaxies evolve via gravitational instability determined by the galactic dynamics, measuring the mass distribution of internal structures of galaxies is most fundamental to uncover the galaxy evolution and address the question *how galaxies came to have diverse morphology as we observe today?*. Figure 1.8 shows the evolution of galaxies depending on the contribution of the bulge, disk, dark matter halo to galactic dynamics. Delineating the physical conditions of different galaxy morphology and property may be archived by studying the dynamical stability of galaxies through measuring their mass distributions and kinematics and comparing them across different cosmic ages. As we summarize below, there are practical challenges in identifying the structure of galaxies and measuring their mass distribution.

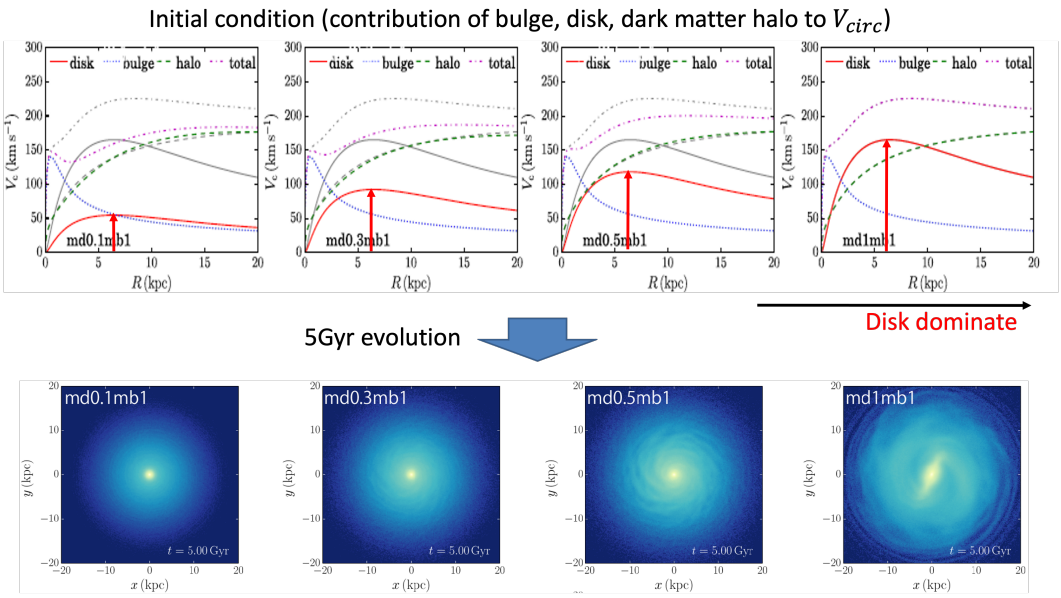

Figure 1.8: Snapshots at 5 Gyrs for galaxies with different initial conditions obtained in N-body numerical simulation. The first row shows the initial conditions between five models, indicating the contributions of bulge, disk, dark matter halo to the galactic dynamics (i.e., circular velocity). The second row shows the 5 Gyrs snapshots. Disk dominated galaxy immediately forms the bar structure and grand design spiral. On the other hand, in galaxies with lesser disk contribution, bar and spiral formation is progressively suppressed. Figure is adapted from Fujii et al. (2018)

Challenge 1: Uncertainty in Stellar Mass to Light Ratio

The kinematics of gas and stars in galaxies allow us to derive the total mass distribution of all internal structures of galaxies(a central black hole, bulge, disk, and dark matter). However, it is challenging to decompose the total mass distribution into that of each internal structure. The black hole is much smaller than any other galactic structure, so it can be regarded as a particle (i.e., the circular velocity can be described as $V_{circ} \propto 1/r$). In order to separate the black hole mass from the rest of other extended structures, we need sufficient resolution to resolve the black hole gravitational influence (Davis, 2014). The stellar mass distribution can be estimated to some extent from its light since stars

radiate energy from internal nuclear reactions, and this radiation from an ensemble of stars can be obtained as a photometric image in the visible to the near-infrared band. However, there is a factor of two uncertainty at best in the conversion factor to derive stellar mass from stellar light (stellar mass to light ratio, $M/L*$) because it relies on the correctness of the stellar evolution model, stellar initial mass function, star formation history, and chemical enrichment history, which are barley accessible by the current observations (Courteau et al., 2014). This uncertainty is large enough to encompass a wide range of unknown dark matter density in a given radius.

Challenge 2: Mass - Anisotropy Degeneracy

In an attempt to derive mass distributions for galaxies with a wide range of morphologies and masses, it is not always possible to obtain the information necessary to trace the gravitational potentials of galaxies. Early-type galaxies typically do not have enough neutral hydrogen (HI) to detect the emission and measure the velocity with sufficient signal-to-noise ratio and high spatial resolution. We need to rely on the kinematics of stars or globular clusters to derive the total mass distribution of galaxies, which is subject to the uncertainty of the orbital anisotropy (i.e., so-called mass-anisotropy degeneracy; Courteau & Dutton 2015). The velocity dispersions, σ_x, σ_y, and σ_z for the three spatial directions are not necessarily the same (i.e. isotropic, $\sigma_x = \sigma_y = \sigma_z$), but in general anisotropic $\sigma_x \neq \sigma_y \neq \sigma_z$. It is difficult to determine the anisotropy which quantifies the fraction of two components to close the Jeans equation (for example, $\beta = 1 - (\sigma_z/\sigma_R)^2$ in cylindrical coordinates (R, θ, z)) since we can only measure the velocity dispersion projected along the line of sight with the specific viewing angle. Furthermore, the velocity anisotropy may vary with the location of the galaxy and take different values depending on the stellar structures (i.e., bulge and disk) or stellar

population. The general prescription for dealing with this degeneracy is to use multiple kinematic tracers (e.g., different stellar populations): each can effectively constrain the mass at its characteristic radius (Zhu et al., 2016).

Challenge 3: Photometric Decomposition vs. Kinematic Decomposition

Decomposing the stellar surface brightness distribution into main stellar components such as a bulge and disk has been widely conducted to study the structure of galaxies. The decomposition is usually done by fitting the 2d stellar surface brightness with a Sérsic profile for bulge (Sersic, 1968) and an exponential profile for disk (Freeman, 1970). So, it is model-dependent and can be largely affected by substructures (Gao & Ho, 2017). Moreover, we can only obtain the two-dimensional stellar luminosity distribution, a projection of light to a certain line of sight. For example, it is not clear whether the exponential nature of the disk conserves down to the center of galaxies where the bulge structure dominates (Breda et al., 2020), or to the outer radius (Erwin et al., 2005) where stellar halo starts to dominate. Therefore, the decomposition result is not necessarily unique, and its interpretation is challenging. The stellar structure may be better recognized and more physically characterized with the kinematic information of the stars because the shape of the structure is determined by the stellar orbits that comprise it. For example, a round bulge and stellar halo consist of stars on radial orbits with random orientation, while the flat disk consists of stars on nearly circular orbits with a common rotating axis (e.g., Zhu et al. 2018b). Integral field spectroscopy (IFS) surveys such as SAURON, ATRAS3d, CALIFA, SAMI and MaNGA provide the information of stellar kinematics for a large sample of galaxies (see details in de Zeeuw et al., 2002; Cappellari et al., 2011; Sánchez et al., 2012; Croom et al., 2012; Bundy et al., 2015, respectively), which has led to ideas to decompose the galactic structure with the help

of stellar kinematics (Taranu et al., 2017; Zhu et al., 2018a). Du et al. (2019, 2020) developed a method to automatically decompose the galactic structures of simulated galaxies based on their stellar kinematics in the phase space using unsupervised machine learning. The studies suggest that the structures identified by stellar kinematics do not necessarily correspond to the structures identified by surface brightness. Some studies decomposed stellar spectra into a bulge and disk based on the photometric decomposition and studied their kinematics (Tabor et al., 2019, 2017; Oh et al., 2020), suggesting the overall kinematics of galaxies can be interpreted as the combination of two kinematically distinct components, bulge, and disk. Further investigations are required to identify and interpret the galactic structure in terms of both stellar kinematics and morphology.

Challenge 4: Galactic Structure in High Redshift Galaxies

The internal structure of distant massive galaxies (z>3), which are rapidly building up their stellar masses and usually heavily dust-obscured, has remained to be unknown due to the heavy dust attenuation of stellar radiation as well as the sensitivity and resolution limitations of the current telescopes at optical to near-infrared wavebands. Even with high-resolution HST images, it is challenging to study the internal structures of massive star-forming galaxies, and the results are largely inconclusive.

Structure of This Thesis

In chapter 2, we collect various observational data for NGC 1380 (i.e., large-field-of-view stellar photometric image by HST, and stellar kinematics by VLT/MUSE and central molecular gas kinematics by ALMA). We use both stellar kinematics and photometric data to identify and interpret the galaxy's stellar structures (i.e., bulge, disk, stellar halo). In terms of photometric data, we decompose the observed stellar light into spherical

(like a bulge and halo) and flat (like a disk) structures non-parametrically by fitting the stellar surface brightness with multiple Gaussians with two axial ratios ($q_{\rm flat}$<$q_{\rm spherical}$). In terms of stellar kinematics, we infer the stellar structure by studying the variation of velocity anisotropy and the ratio of rotational motion to velocity dispersion. The identified structures of bulge (within ~ 20 arcsec), disk (from ~20 to ~100 arcsec), and stellar halo (from ~100 arcsec) in NGC1380 are concordant with both the stellar kinematics and photometric data (**Challenge 3**). The molecular gas kinematics shows a velocity rise towards the center, which manifests the presence of a black hole. By modeling the rotating disk kinematics, we, for the first time, measure the black hole mass in NGC 1380 and the extended stellar mass distribution, independent of the assumption of star formation history, initial mass function, and chemical enrichment history (**Challenge 1**). The distribution of dark matter is estimated by modeling the stellar kinematics, which covers a large area of the galaxy. Previous studies modeling early-type galaxies simply assumed the constant orbital anisotropy over the galaxy (Cappellari et al., 2013). We allow the spatial variation of orbital anisotropy by assigning different velocity anisotropies to the bulge and disk structures identified. The degeneracy between velocity anisotropy and the mass distribution was further mitigated by using the central mass distribution (i.e., stars and black hole mass 5 arcsec) measured by molecular gas modeling as a prior distribution (**Challenge 2**).

The recent development of the ALMA telescope with high sensitivity and resolution has allowed us to spatially resolve far-infrared radiation of dust near the peak of black body radiation in the rest frame. Since the radiation from massive stars mainly heats dust, it can map out star-forming regions and investigate the ongoing formation of substructures in galaxies. The [CII] emission line (158 microns) in the far-infrared band is typically the brightest emission line in star-forming galaxies (Jones et al., 2017). The

[CII] line is considered to be emitted from a variety of gas phases, from ionized to neutral and molecular gas, which makes its interpretation difficult (Pineda et al., 2013). However, it allows us to trace the kinematics of the entire disk, allowing us to derive the mass distribution of the galaxy. **In Chapter 3**, we aim to apply the method developed in Chapter 2 to a further distant galaxy and identify its internal structure and ongoing formation. The luminous [CII] emission from an extreme star formation and ALMA's high sensitivity allow us to obtain the most detailed [CII] gas kinematics for an unlensed, hyper luminous infrared galaxy (HyLIRG) at redshift 4.4, BRI 1335-0417. Analyzing the [CII] gas kinematics, we discovered a rotating disk, a central compact structure like a bulge, and a spiral structure on the disk in a galaxy at a redshift of 4.4, long before the peak of cosmic star formation (Tsukui & Iguchi, 2021). HyLIRGs are thought to be formed mainly through major mergers, but surprisingly the dust-obscured internal structure revealed in this study is similar to those of a spiral disk galaxy, which may give us a clue to the detailed formation scenario of HyLIRGs and massive galaxies in cosmic history (**Challenge4**).

In chapter 4, we conclude our work and discuss the prospects based on our results obtained throughout this thesis.

2

Measurement of Mass Distribution of Galactic Structures

We have developed a method to measure the mass distribution of galactic structures: a central black hole, bulge, disk, and stellar and dark matter halos. In order to derive these structures with a high degree of accuracy, it is essential to have a high-resolution observation that allows us to dynamically derive the mass distributions of the central black hole, bulge, and disk in the center of the galaxy, which was difficult to do before

the operation of ALMA, as well as wide-field observations that cover the radius where dark matter starts to dominate. Otherwise, the indeterminacy of the baryon-dominated central mass will affect the determination of the dark matter mass distribution in the outer part of the galaxy (i.e., Newton's theorems). Although there is no spectroscopic imaging instrument that can archive such high resolution and wide field of view at the same time, NGC 1380 has a very rich data set that includes: stellar kinematics measured from the atomic absorption features in the stellar continuum obtained by Multi Unit Spectroscopic Explorer (MUSE) (Sarzi et al., 2018) on the Very Large Telescope (VLT); stellar surface distribution obtained by Advanced Camera for Surveys (ACS) on Hubble Space Telescope (HST); and high-resolution CO(2-1) molecular gas kinematics by ALMA Band 6 (Boizelle et al., 2017). In this chapter, we present our studies to identify distinct galactic structures: a central black hole, bulge, disk, stellar and dark matter halos in the early-type galaxy NGC 1380 and measure these mass distributions, exploiting and combining those archival data.

2.1 Introduction of This Chapter

Most galaxies form and are embedded in dark matter halos, which dominate the total mass of galaxies and have a significant impact on the stability and evolution of galaxies (Fujii et al., 2018). Therefore, the relative distribution of dark matter to baryon would be one of the useful predictions of galaxy formation models to be compared with observations. But it is still challenging to estimate the dark matter distribution observationally. Measuring dark matter mass distribution in galaxies requires a precise stellar mass to light ratio (M/L). However, stellar M/L is indirectly estimated from stellar population synthesis models, and the estimated stellar M/L carries an uncertainty of factor 2 at best due to

unknown star formation history and the initial stellar mass function (Courteau et al., 2014).

For disk dominated late-type galaxies (LTGs), various methods have been used to separate baryons from dark matter, e.g., Tully-fisher residuals (Courteau & Rix, 1999; Dutton et al., 2007; Courteau et al., 2007), gravitational lensing (Barnabè et al., 2012; Dutton et al., 2011), vertical disk kinematics (Martinsson et al., 2013a). For early-type galaxies (ETGs), on the other hand, it is more challenging to separate the total mass into baryons and dark matter since there is no means to do so dynamically. The prevalence of molecular gas in the central sub-kpc region of ETGs recently shown by Young et al. (2014) and Atacama Large Millimeter/ submillimeter Array (ALMA) allow us to measure the kinematics of molecular gas with sufficient resolution to measure the black hole mass and extended stellar mass distribution separately (Davis et al., 2013a; Onishi et al., 2015; Barth et al., 2016a,b; Boizelle et al., 2019; Davis & McDermid, 2017; Davis et al., 2018b; Smith et al., 2019). By separating the mass distribution into a central black hole and stars with the signature of quasi-Kepler rotation in the high-resolution molecular kinematics, these studies give stellar M/L ratio independent of assumptions on star-formation history and initial stellar mass function.

In order to break the degeneracy between baryons and dark matter in early-type galaxies, in this paper, we first dynamically measure the stellar mass to light ratio and black hole mass using high-resolution molecular gas kinematics detected in the central region where the contribution of dark matter can be negligible ($\ll R_e$). Then, with the derived mass to light ratio as prior information, we aimed to further constrain the fraction of dark matter by adding a wider field of view stellar kinematics that covers the outer region of the galaxy where dark matter starts to dominate.

In addition, the early-type galaxies typically do not have enough neutral hydrogen

(HI) to enable us to detect the emission with a sufficient signal-to-noise ratio and high spatial resolution. We need to rely on the kinematics of stars or globular clusters in order to derive the total mass distribution of galaxies, which is subject to the uncertainty of the stellar orbits (i.e., so-called mass-anisotropy degeneracy; e.g., Courteau & Dutton 2015). Our idea of combining rotating gas kinematics and stellar kinematics has merit on this point because the general prescription of dealing with this degeneracy is to use multiple kinematic tracers: each can effectively constrain mass at its characteristic radius.

This chapter is organized as follows. In the next subsection, we summarize the basic properties of our target NGC 1380, which is an optimal target for our purpose. In Section 2.2, we describe HST/ACS *I* band imaging, VLT/MUSE stellar kinematics and ALMA CO (2-1) molecular gas kinematics. In Section 2.3, we infer the galactic structure and decompose that into bulge plus stellar halo and disk in NGC 1380 based on HST/ACS *I* band imaging and VLT/MUSE stellar kinematics in terms of the dominance of velocity dispersion over mean rotation velocity of stars, the shape of velocity ellipsoids and morphological geometrical properties of stellar brightness distribution. In Section 2.4, we describe the method and result of dynamical modeling based on molecular gas kinematics and stellar kinematics to derive the mass of central black hole, stars, and dark matter halo. In Section 2.5, we discuss the results, implication of derived BH mass, stellar mass and dark matter halo mass in NGC 1380. In Section 2.6, conclusions in this chapter are summarized.

2.1.1 Target NGC 1380

Early type galaxy NGC 1380 resides in the Fornax cluster. The luminosity distance $D_{\rm L}$ is 21.2 ± 0.7 Mpc (Blakeslee & John, 2015). Adopting this distance, 1 arcsec corresponds

to 102.2 ± 3.4 pc. There has been no direct measurement of the black hole mass so far in NGC 1380. The empirical $M_{\rm BH} - \sigma$ relationship (Kormendy & Ho, 2013) provides a black hole mass $M_{\rm BH}$ of $3.9 \times 10^8 M_\odot$ (solar masses) and the estimated black hole sphere of influence $r_{\rm g} = GM_{\rm BH}/\sigma_*^2$ of 38 pc (0.37"). The sphere of influence $r_{\rm g}$ is used as an estimate of the radius within which the black hole mass dominates over stellar mass, and thus used as a measure of the angular resolution needed for accurate BH measurement. NGC 1380 was observed by Multi Unit Spectroscopic Explorer (MUSE) on the Very Large Telescope (VLT) as a part of Fornax 3D project, and its stellar kinematics is measured with the high-quality spectroscopic data (Sarzi et al., 2018). The I band image of the stellar surface distribution of NGC 1380 was obtained by Advanced Camera for Survey (ACS) on Hubble Space Telescope (HST). These data covered a large field of view out to 120", that is 3 effective radius R_e, where the dark matter starts to dominate. (R_e is the radius within which half of the total light of the galaxy is enclosed.) Also, the CO (2-1) emission in NGC 1380 is observed by ALMA (Boizelle et al., 2017) with superb angular resolution and sensitivity. Aiming to derive the dark matter distribution of NGC 1380, we present an analysis combining the high angular resolution ALMA data of CO (2-1) molecular gas kinematics in the central sub-kpc of the galaxy and MUSE stellar kinematics with a large field of view covering the halo of the galaxy. We derive the mass distribution of central BH, bulge, and disk, purely dynamically from molecular gas kinematics obtained as the ALMA data cube and then derive the mass distribution of dark matter from a large field of view stellar kinematics by properly taking into account the mass of BH, bulge, and disk.

#	Properties	Values
(1)	Alternative names	FCC 167, ESO 358-G28
(2)	Morphological Type	Early type, S0/a
(3)	Kinematical Type	Fast rotator
(4)	R.A. [h m s]	03 36 27.573
(5)	Dec. [° ’ "]	-34 58 33.84
(6)	Radial velocity [km s^{-1}]	1854.5
(7)	Distance [Mpc]	21.2 (0.7)
(8)	mB [mag]	11.3
(9)	I-band Re [arcsec]	36.6
(10)	Gas disk position angle [°]	182.1 (3.2)
(11)	Gas disk inclination [°]	75
(12)	Stellar position angle [°]	183.9
(13)	Velocity dispersion [km s^{-1}]	211

Table 2.1: Properties of NGC 1380 (1) Galaxy alternative names; (2) and (3) morphological type from Ferguson (1989) and kinematical type from Pota et al. (2013); (4) and (5) Right ascension and declination (J2000) reported in Boizelle et al. (2017) from ALMA nuclear continuum observation; (6) heliocentric radial velocity from Boizelle et al. (2017); (7) luminosity distance measured by the surface brightness fluctuation from Blakeslee et al. (2009); (8) B band magnitude from Ferguson (1989); (9); *I* band (F814W filter) effective radius along semimajor axis estimated from MGE components (see subection 2.3.2). (10) and (11) position angle and inclination of the gas disk based on the gas kinematics from Boizelle et al. (2017); (12) position angle of stellar kinematics from Sarzi et al. (2018); (13) central velocity dispersion of stars from the HyperLeda data base Makarov et al. (2014)

2.2 Observation Data

2.2.1 HST *I* band Image

NGC 1380 was observed with Advanced Camera for Surveys (ACS) Wide Field Channel F814W (*I* band) filter on HST (PI: Blakeslee) on 2006 August 3 as a part of program GO-10911. The calibrated data is available at Hubble Legacy Archive [1]. This filter choice provides a good tradeoff between angular resolution and amplitude of dust extinction. Also, ACS provides a large field of view (~ 105"). The effective point spread function is measured from the stellar images using ePSFbuilder in astropy package photutils (Bradley et al., 2019), resulting in FWHM ~ 0.15" which is sufficient to resolve the black hole sphere of influence r_g. The *I* band image and its inner 32 arcsec region is presented in Figure 2.1. Since the galaxy's light dominates the field of view of the HST image, it is impossible to estimate the sky background emission accurately. We estimated the background emission in HST image using data obtained with a ground-based telescope OmegaCam in which the background emission was accurately estimated and subtracted by Iodice et al. (2019). A surface brightness profile of *I* band image of HST is measured using the same procedure in Iodice et al. (2019). The resulting *I* band profile in the outer region of the galaxy is compared and matched with the sky subtracted *i* band profile from (Iodice et al., 2019), which gives us an estimate of the spatially constant sky background. After the sky background subtraction, there is a good agreement between *I* band profiles measured from HST and OmegaCam (Figure 2.2).

[1] https://hla.stsci.edu/hla_welcome.html

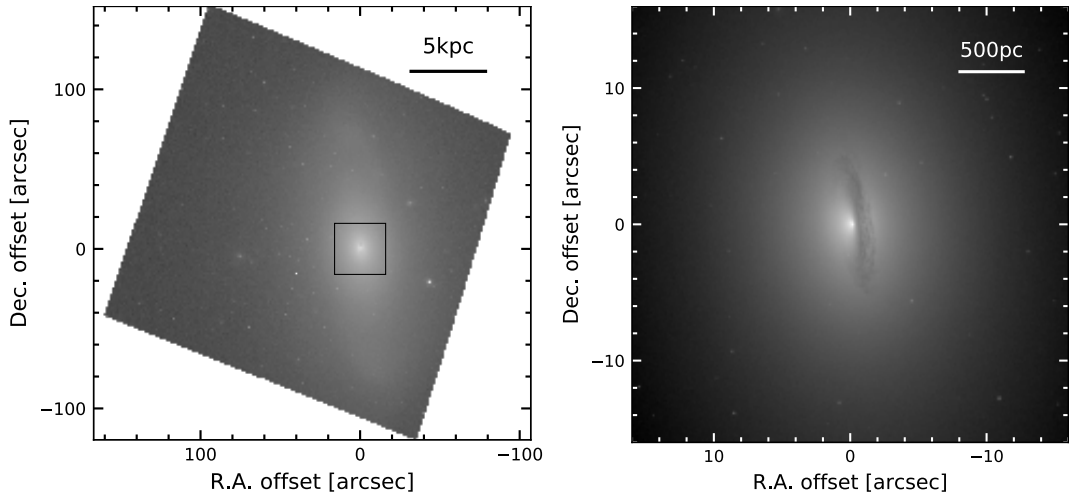

Figure 2.1: HST *I* band image of NGC 1380. Left panel: The HST Advanced Camera for Surveys (ACS) F814W image of roughly 200" × 200" (20.4 kpc × 20.4 kpc) region, displayed in logalithmic scale. Right panel : Same as left panel, but for a central 32" × 32" (3.3 kpc × 3.3 kpc) region around the nucleus, indicated by the black square in the left panel. The image clearly reveals the dust lane in this galaxy.

2.2.2 VLT/MUSE Spectroscopic Images - Atomic Absorption Lines in Stellar Continuum

NGC 1380 was observed with the MUSE instrument on ESO VLT as a part of the Fornax 3D project. The deep observation was conducted with 3 pointings of the field of view of 1×1 arcmin^2 with spatial sampling of 0.2×0.2 arcsec^2 under Wide Field Mode (Bacon et al., 2010), providing integral-field stellar spectra out to stellar halo region (~120"). A wavelength range is 4650-9300 Å with spectral resolution of ~ 2.5 Å (FWHM) at 7000 Å and spectral sampling of 1.25 Å pixel^{-1}. The details of the observation and the data reduction are described in Sarzi et al. (2018). The stellar kinematics were also measured by the Fornax 3D team (Sarzi et al., 2018) with a standard method briefly described

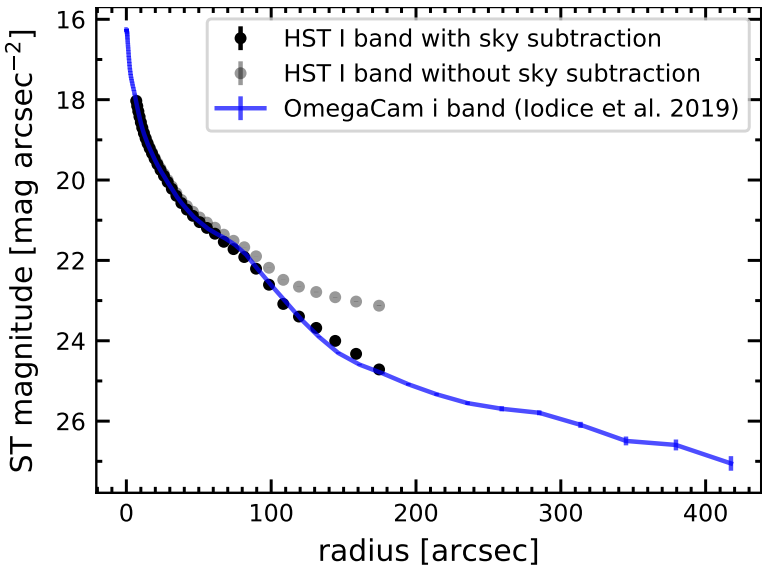

Figure 2.2: Azimuthally-averaged surface brightness profile of the HST *I* band image of NGC 1380 with the subtraction of the sky background emission (black points) and without (glay points and line). The sky background in HST image is estimated and subtracted by comparing with the OmegaCam *I* band data from Iodice et al. (2019) (blue points and line).

as follows. After the standard calibration, the data were binned to have a minimum S/N=40 per pixel by Voronoi binning method (Cappellari & Copin, 2003) for the reliable extraction of stellar kinematics. Then, stellar kinematics in each Voronoi bin is extracted by Penalised Pixel Fitting Code (pPXF; Cappellari & Emsellem 2004; Cappellari 2017). pPXF fits stellar templates to the observed spectra, providing the line of sight stellar kinematics parametrized by mean velocity V, velocity dispersion σ, and h_3 and h_4 (Cappellari & Emsellem, 2004; Cappellari, 2017). They used a representative subset of MIUSCAT models (Vazdekis et al., 2012) as a stellar template. The subset was taken by uniformly sampling 65 templates with age from 0.1 to 15.8Gyr and metallicity[2] from -2.32 to 0.22 dex. In Figure 2.3, we shows stellar kinematics maps of line of sight mean velocity V, velocity dispersion σ [see also Figure 7. in Sarzi et al. (2018)] and root-mean-square velocity $V_{\rm rms} = \sqrt{V^2 + \sigma^2}$. We carefully checked the data for any extreme outliers which may affect our result and applied sigma clipping to the data points where the root mean square velocity deviates more than 2.5 sigmas from the mean value of neighboring data points (within 4 times the distance to the nearest data point).

2.2.3 ALMA Band 6 Spectroscopic Images - CO(2-1) and Dust Continuum

NGC 1380 was observed in CO (2-1) line emission (230.538 GHz) using ALMA with the Band 6 receiver on 2015 Jun 11 as a part of program 2013.1.00229.S. The observation consisted of a single pointing with three spectral windows with a bandwidth of ~ 2GHz; one spectral window positioned to observe the redshifted CO (2-1) line emission, the remaining two positioned to observe the continuum emission at ~ 227 and ~ 245 GHz.

[2]Metallicity is defined as the mass fraction of elements heavier than helium typically in the unit of decimal exponent (dex) relative to the solar values $Z_{\rm sun} = 0.0134$.

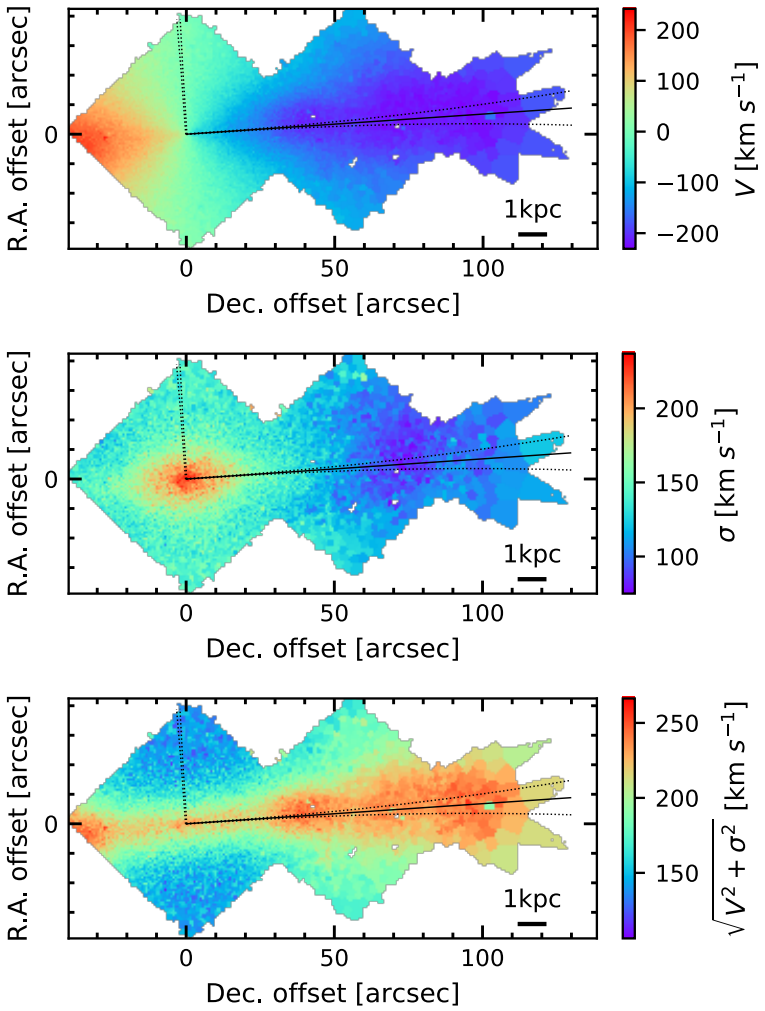

Figure 2.3: Stellar kinematic maps of the line of sight mean velocity V (top) and velocity dispersion σ (middle) for NGC 1380 derived from the Voronoi-binned MUSE data, which are adapted from Sarzi et al. (2018), Figure 7. In addition, the root mean square velocity $V_{\rm rms} = \sqrt{V^2 + \sigma^2}$ is computed and shown (bottom). The major axis is shown in black solid line. The width used to extract the 1 dimensional profile along major and minor axis (see Figure 2.7 for major axis)

The frequency channel width of spectral windows was 488kHz for line spectral window and 15.6MHz for continuum spectral window. The sampled spatial frequency of the observation (uv coverage) is shown in Figure 2.4 and the resulting point spread function is shown in Figure 2.5, although the effect of the side lobes of point spread function is removed by the task of TCLEAN in the imaging process. The same data set has been reduced and presented in Boizelle et al. (2017). We reduced the data similarly but independently and imaged with different parameters suited for our purpose of the gas dynamical modeling. The data reduction was performed using the version 4.3.1 of the Common Astronomy Software Applications (CASA; McMullin et al. 2007) pipeline. The flux density of the continuum emission was subtracted by fitting the first-order polynomial to the line-free channels of the bandpass response and subtracted its emission components from the visibility data in the uv-plane using a task of UVCONTSUB in CASA. After the continuum subtraction, we imaged the line spectral window into the observed cube with the three dimensions of right ascension, declination, and velocity using a task of TCLEAN in CASA with the velocity channel resolution of 10 km s^{-1} after binning about 16 frequency channels of 488kHz in order to improve the signal to noise ratio. The visibility data were weighted by the Briggs scheme with a robust parameter of 0.5, resulting in a synthesized beam with FWHM 0.25" $\times$ 0.18" at a position angle of 86°. The cell size of the image is set with one-third of the minor beamwidth. The root mean square noise of each velocity channel with a width of 10 km s^{-1} is about 0.54 mJy/beam, which agrees with that obtained in Boizelle et al. (2017) taking the difference of channel width into account. The moment maps of intensity, velocity, and velocity dispersion were made from the observed cube using moment mask method (Dame, 2011) and are shown in Figure 2.6.

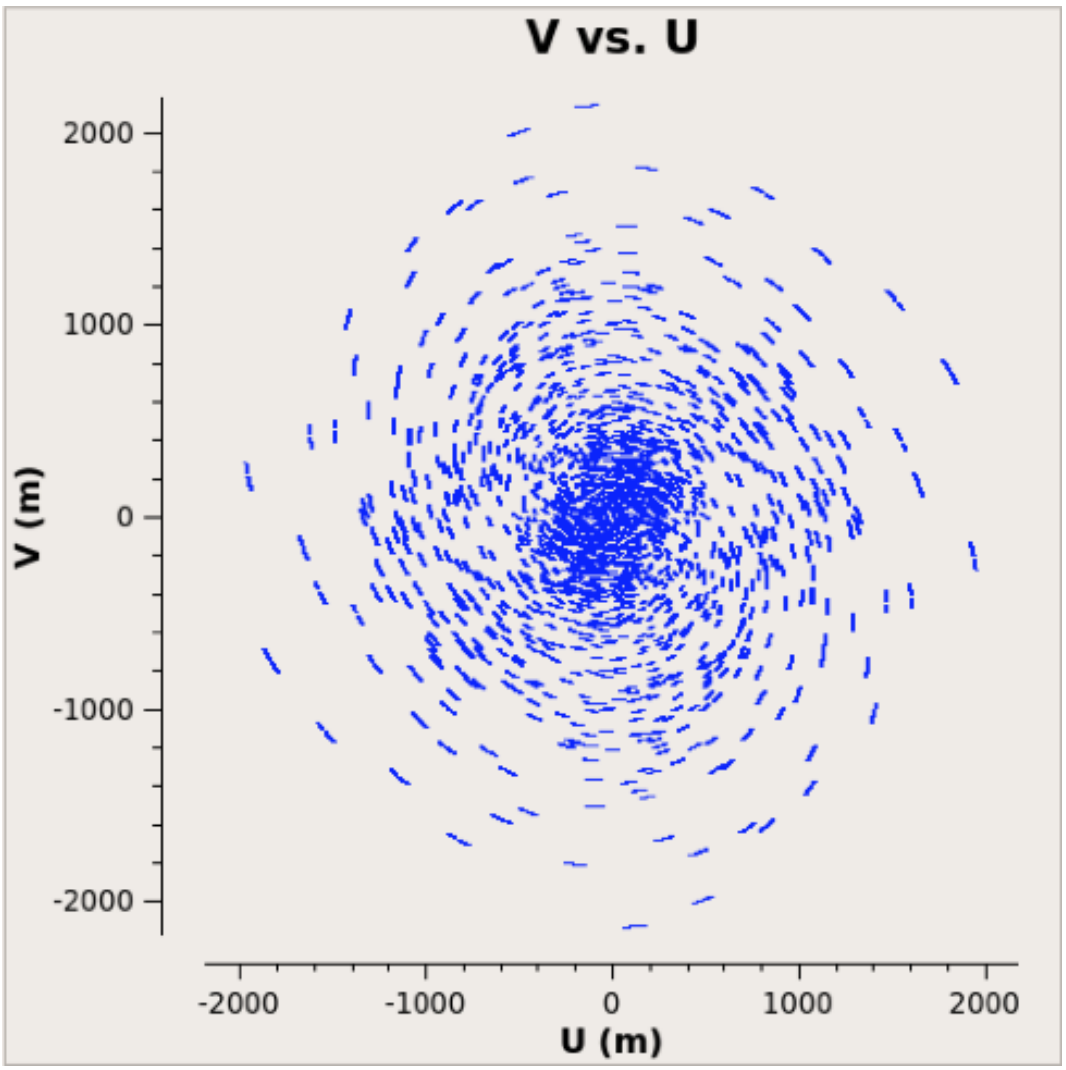

Figure 2.4: The relative position vectors (u, v) for each antenna pair are shown. The vectors are projected onto the sky plane orthogonal to the phase reference position (approximately the position of NGC 1380). These position vectors correspond to the spatial frequency components $(k_u, k_v) = (\lambda/u, \lambda/v)$ of intensity distribution sampled by the interferometer observation at an observing wavelength λ.

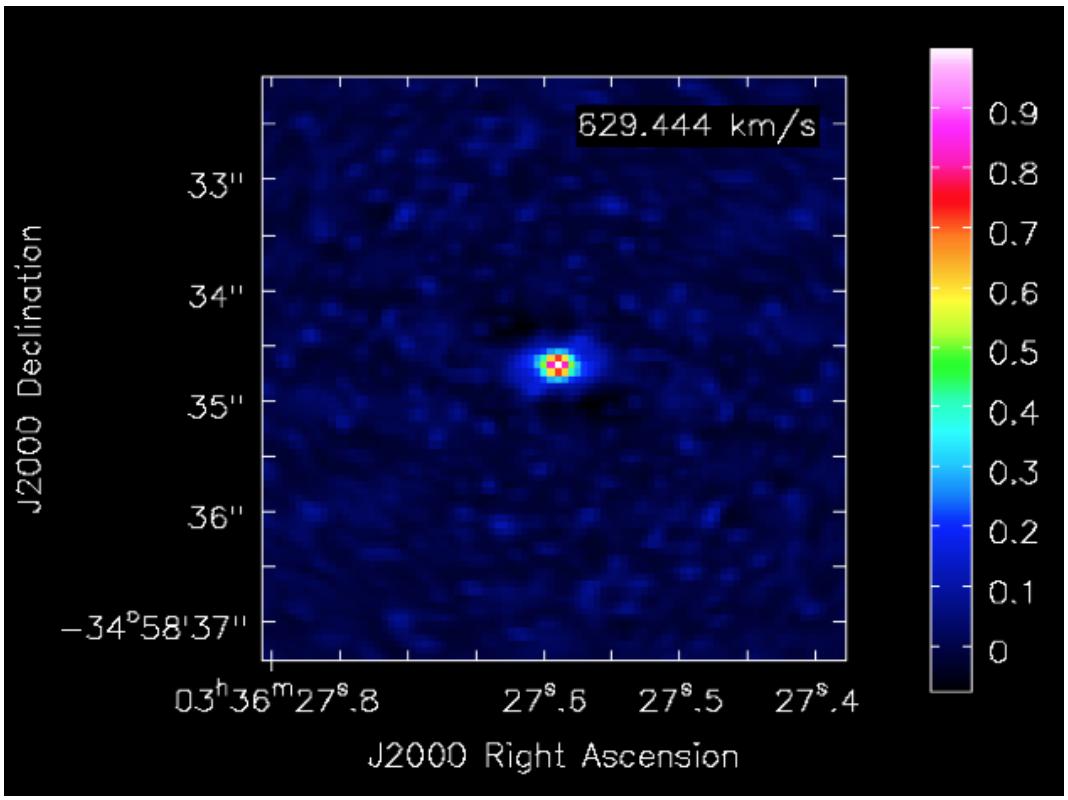

Figure 2.5: The point spread function (i.e. synthesized beam is shown). Note that the effect of the side lobes is removed by the imaging process of the task, TCLEAN.

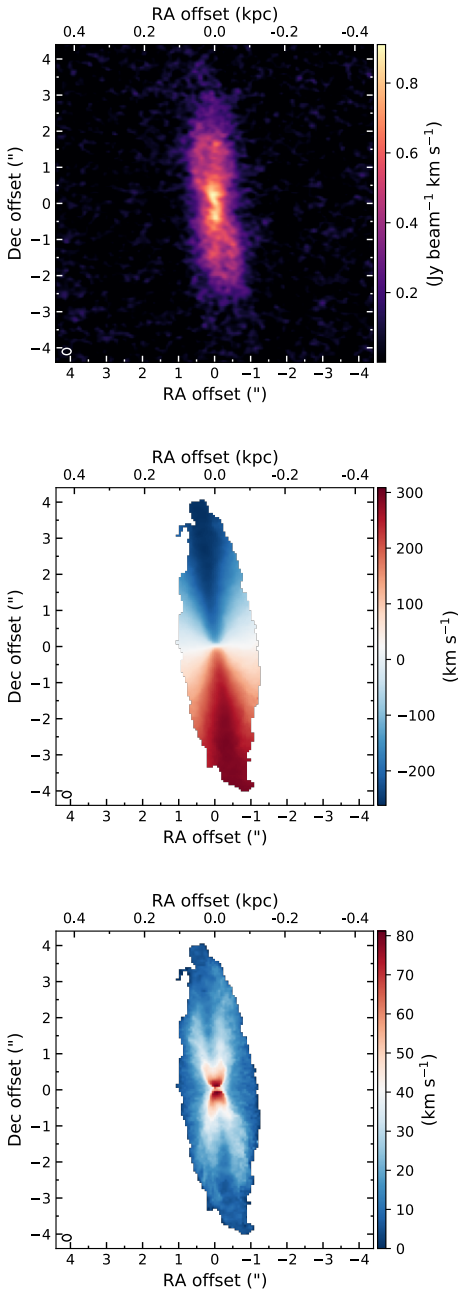

Figure 2.6: Morphology and kinematics of CO (2-1) line emission in NGC1380. Top, middle, bottom panels are respective CO (2-1) maps of intensity (moment 0), intensity-weighted velocity (moment 1) and intensity-weighted velocity dispersion (moment 2). The masked moment method (Dame 2011) is used to produce intensity weighted velocity and velocity dispersion map. The full width half maximum (FWHM) of the synthesized beam, 0.25" × 0.18" at a position angle of 86°, is shown by an ellipse in the left bottom corner of each panel.

2.3 Result I: Identifying Galactic Structures of NGC 1380

2.3.1 Distinct Galactic Structures with Stellar Kinematics

In Figure 2.7, we show the 1 dimensional profile of line of sight mean velocity V, velocity dispersion σ, and root-mean-square velocity $V_{\rm rms} = \sqrt{V^2 + \sigma^2}$ along the major axis (see Figure 2.3). In the central region within $\sim$ 20 arcsec, velocity dispersion σ exceeds the mean velocity V, suggesting that the galaxy has a bulge-like structure, which is supported by random motion rather than rotational motion. From the radius of about 20 arcsec, the mean velocity starts to dominate over the velocity dispersion, reaches the maximum velocity of 220 km s^{-1} at a radius of 40 arcsec, and remains constant up to a radius of about 105 arcsec. This indicates that the stars have a disk structure supported by rotational motion. Furthermore, from a radius of 105 arcsec, the rotational speed decreases, and the velocity dispersion increases again to about 110 km s^{-1}. There may be a transition from a disk structure to a stellar halo structure at this radius. These global trends of V and σ dominance are more clearly visible in the 1-dimensional profile of V/σ shown in Figure 2.8 since the V and σ are appeared to be anti-correlated with each other. On the other hand, root-mean-square velocity is almost constant over the galaxy. The root-mean-square velocity is a good tracer of total mass, like a circular velocity in a purely rotation supported system, regardless of whether the galaxy is supported by rotation or random motion of stars (Williams et al., 2009). The constant root-mean-square velocity indicates the existence of dark matter halo by the analogy to the flat rotation curve observed in spiral galaxies.

To corroborate these pictures, we also make the 1-dimensional profile of the axis

ratio of the intrinsic velocity ellipsoid, σ_ϕ/σ_R as shown in Figure 2.9. σ_ϕ and σ_R are the azimuthal and radial components of velocity ellipsoid. Those are related to the observed major and minor axis velocity dispersions, $\sigma_{\rm maj}$ and $\sigma_{\rm min}$ under the assumption of thin-disk geometry as (Noordermeer et al., 2008)

$$\begin{aligned}\sigma^2_{\rm maj} &= \sigma^2_\phi \sin^2 i + \sigma^2_z \cos^2 i \\ \sigma^2_{\rm min} &= \sigma^2_R \sin^2 i + \sigma^2_z \cos^2 i,\end{aligned} \tag{2.1}$$

where the σ_R is the vertical component of the velocity ellipsoid. Since the inclination of NGC 1380 is ~75° and $\cos^2 i \sim 0.07$, second term related to σ_z is negligible. Thus, the equations 2.1 reduce to

$$\begin{aligned}\sigma^2_\phi &= \sigma^2_{\rm maj}/\sin^2 i \\ \sigma^2_R &= \sigma^2_{\rm min}/\sin^2 i.\end{aligned} \tag{2.2}$$

The ratio σ_ϕ/σ_R can be computed as

$$\sigma_\phi/\sigma_R = \sigma_{\rm maj}/\sigma_{\rm min}. \tag{2.3}$$

Interestingly, in the region of 40 to 100 arcsec – inferred to have a rotation supported disk structure –, the value of σ_ϕ/σ_R takes $0.7 \sim 1/\sqrt{2}$. This value is expected from the epicyclic approximation for a stellar disk with a constant circular velocity, suggesting a flat, rotating disk structure in this region. In the central 20 arcsec region, which is considered to be a pressure supported bulge structure, the assumption of the thin disk may violate, and line of sight projection make it difficult to interpret the value of σ_ϕ/σ_R as the axis ratio of the velocity ellipsoid. Nevertheless, the obtained value of $\sigma_{\rm maj}/\sigma_{\rm min} \sim 1$ in the center can still be interpreted as the stellar structure being isotropic and nearly spherical. From 100 arcsec, σ_ϕ/σ_R starts to increase towards 1, implying the

transition from disk structure to spherical stellar halo structure.

In addition to the global trends of the velocity profile, as noted in Sarzi et al. (2018), there is a slight increase/decrease in velocity/velocity dispersion localized at 75 arcsec. That is more clearly seen in Figure 6 as a sudden decrease in V/σ. Sarzi et al. (2018) shows that there is a bright knot at this distance, and such substructure may produce the increase of velocity dispersion.

2.3.2 Distinct Galactic Structures with Luminosity Profile

We revealed the stellar structures such as a bulge, a disk, and a stellar halo from their line of sight kinematics. We here aim to model these stellar structures based on a photometric image. After carefully masking out the fore/background stars and galaxies, and the central dust extinction (see Figure 2.1), the surface brightness of the HST I band image is measured in the sector spaced uniformly in angle and logarithmically in radius using SECTORS_PHOTOMETRY package (Cappellari, 2002). Then, we parametrized the observed surface brightness distribution with two-dimensional (2D) multi-Gaussian expansion (MGE; Emsellem et al. 1994b; Cappellari 2002). MGE is widely used for reproducing the surface brightness profile of galaxies (Boizelle et al., 2019; Barth et al., 2016a; Onishi et al., 2015), and has the advantage that it provides an estimate of intrinsic luminosity density through the analytical deprojection.

As the galaxy is nearly edge-on, we performed a non-parametric bugle/disk decomposition. MGE allows us to divide Gaussians into two sets, each with a unique axial ratio ($q_{\rm bulge}$, $q_{\rm disk}$; $q_{\rm disk} < q_{\rm bulge}$). The two sets of Gaussians are meant to represent a round structure like a bulge with axis ratio $q_{\rm bulge}$ and a flatted disk structure with axis ratio $q_{\rm disk}$. While fitting the surface brightness of the galaxy by the MGE, we restricted

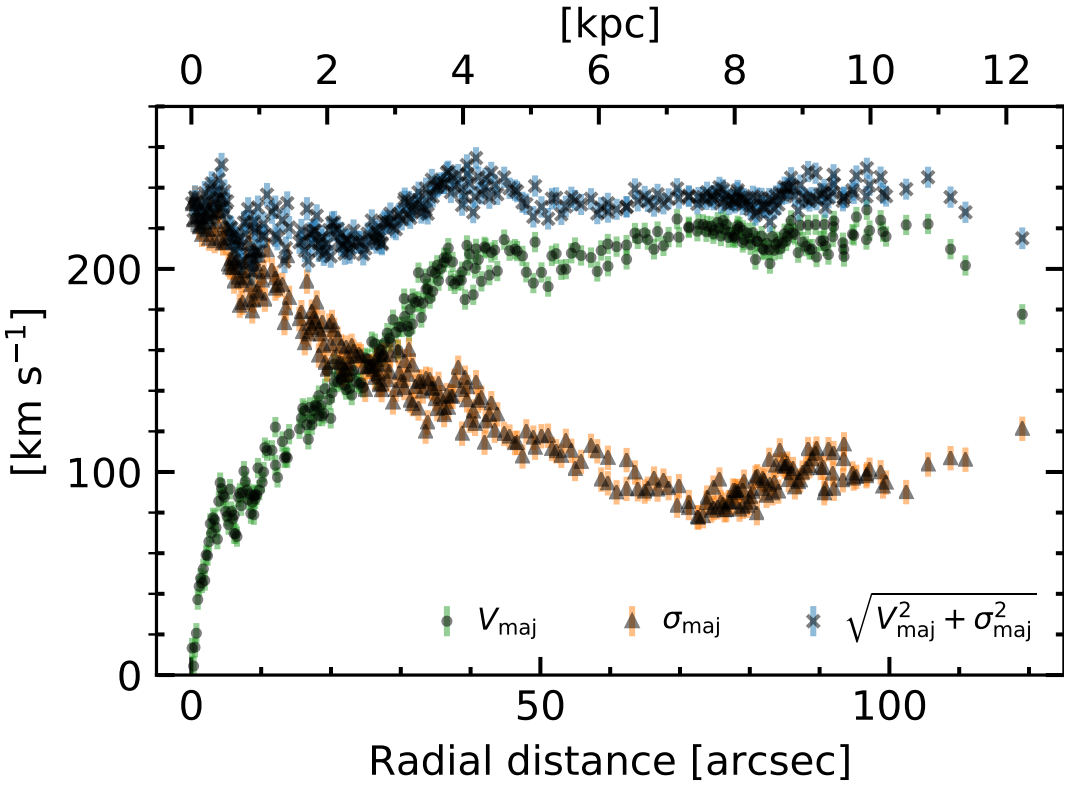

Figure 2.7: Stellar kinematics of NGC1380 extracted from the MUSE data along the major axis at P.A. = 3.9 degree. The mean velocity, the velocity dispersion, and the root mean square velocity are shown by black points with error bars in green, orange, and blue, respectively. The extraction aperture is shown in Figure 2.3. Its width is set to 0.0001 × (radius (arcsec)) 2.25 + 0.1 arcsec in order to include the data points at large radius, since the Voronoi-binned MUSE data is sparser at larger radii.

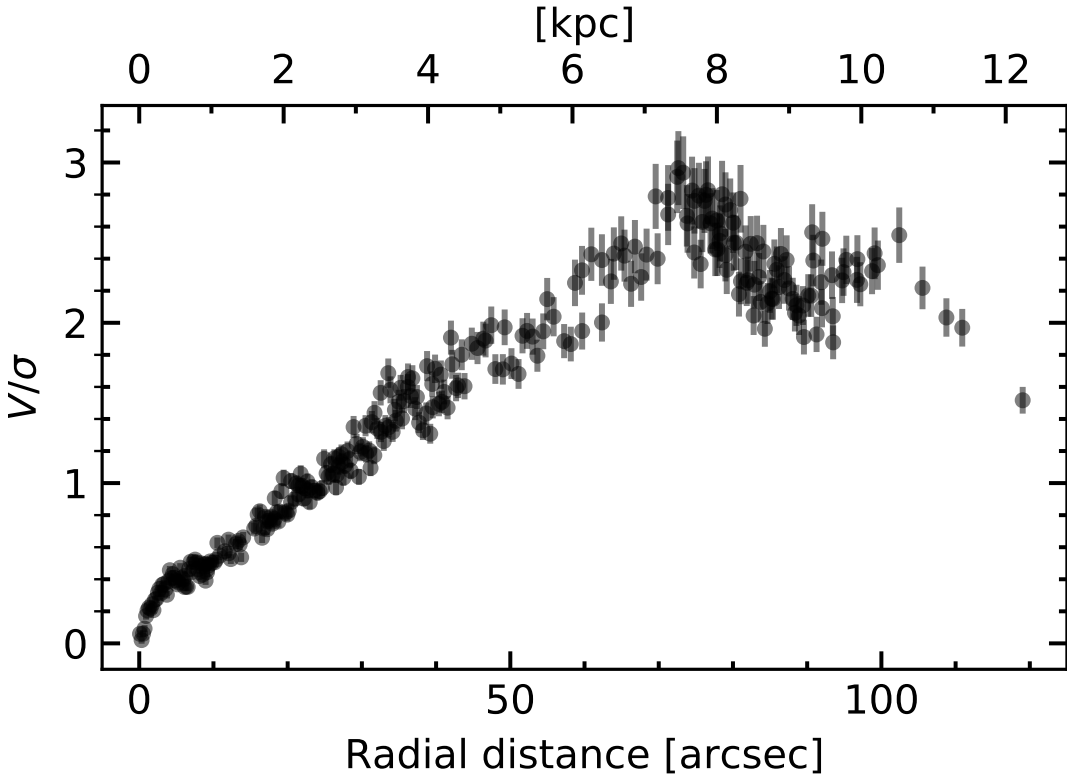

Figure 2.8: V/σ profile along the major axis of NGC1380. The central region within $\sim$ 20 arcsec is pressure supported while the outer region from $\sim$20 arcsec is rotation dominated. The decrease from $\sim$100 arcsec corresponds to pressure supported structure such as stellar halo.

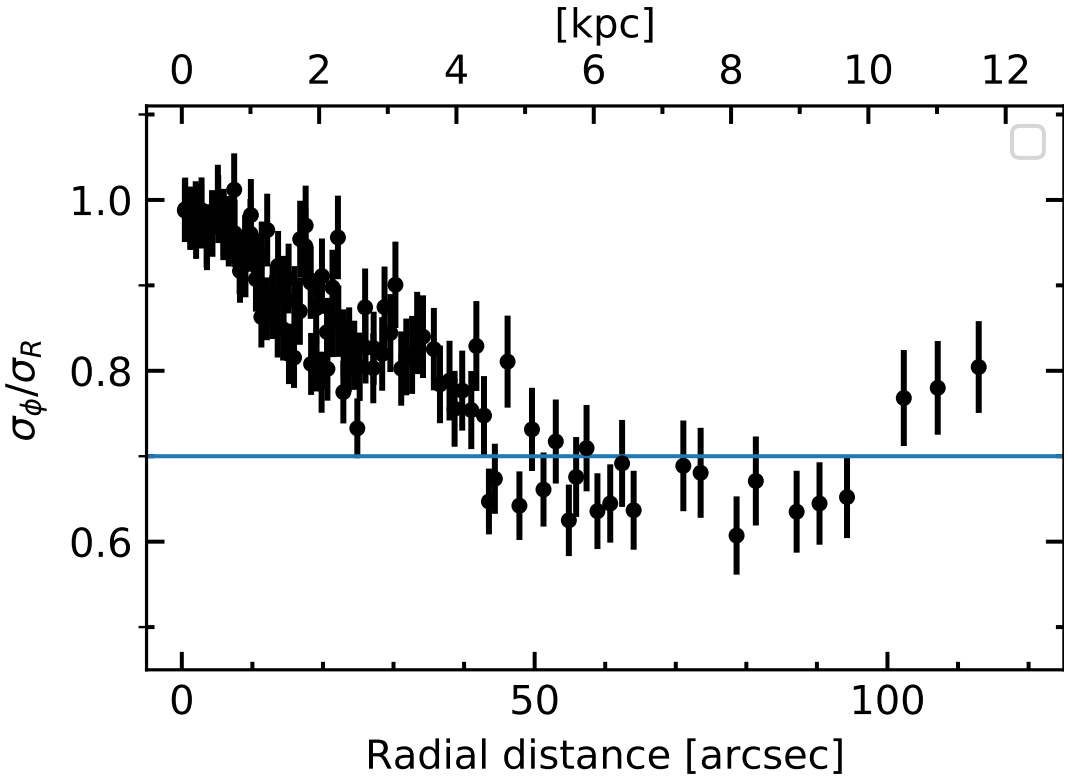

Figure 2.9: The axis ratio of the velocity ellipsoide σ_ϕ/σ_R of NGC 1380, where σ_ϕ and σ_R is the azimuthal and radial intrinsic velocity dispersion respectively. σ_ϕ/σ_R is derived approximately by the equation 2.3. The holizontal blue line shows the expectation from epicycle approximation for flat rotating disk $\sigma_\phi/\sigma_R = 1/\sqrt{2} \sim 0.7$, manifesting the flat rotating disk from 40 arcsec out to 100 arcsec.

the position angle (P.A.) and center of all Gaussians to be the same under the assumption that the galaxy is axisymmetric. The measured effective point spread function is approximated with three Gaussians and taken into account for the fitting (Cappellari, 2002). The mask for the central dust extinction is iteratively modified and improved until the mask sufficiently encloses the dust extinction (see Figure 2.10). The final MGE model of the galaxy has 14 Gaussians, the parameters of which are shown in Table 2. The model reproduces the observed isophote (see Figure 2.10) well. The relative error of the most location is below 10 %, except the region where the substructure is reported in Sarzi et al. 2018 at a radius of $\sim$ 75 arcsec. The non-parametric decomposition of bulge and disk does not work well near the galactic center because the difference in axial ratios between the two components is not obvious. Therefore, two Gaussians with flat axial ratios (with dispersions of 0.07 and 0.32 arcsec) in the bulge-dominated region (<20 arcsec) are classified as bulge components.

Figure 2.11 shows the surface brightness profile of the HST I band image with the bulge and disk components non-parametrically decomposed by MGE. It can be seen that the round component analogous to a bulge and/or stellar halo is dominant in the central 20 arcsec and the outer region from 100 arcsec, while the flat component analogous to a disk is dominant from 20 arcsec out to 100 arcsec, which is concordant with the bulge, disk, and stellar halo structures inferred from the stellar kinematics discussed in subsection 2.3.1. Figure 2.12 shows the circular velocities of the bulge and halo component and bulge components of the best fit MGE model in which both M/L ratios were assumed to be 1. The peak of the disk circular velocity is found to be at a radius of 79.1 arcsec. By analogy with the exponential disk, whose peak of the circular velocity is at 2.2 $R_{\rm d}$ ($R_{\rm d}$ is disk scale length), the scale length of the disk non-parametrically identified is roughly estimated to be 36 arcsec. This value is consistent with the disk

scale length of $36.3^{+1.0}_{-0.4}$ arcsec estimated by the parametric disk-bulge decomposition in NGC 1380 by Bedregal et al. (2006). From the resulted MGE parametrization, the *I* band (F814W filter) effective radius along the semimajor axis is 36.6 arcsec, estimated using MGE_HALF_LIGHT_RADIUS code in JAM package (Cappellari, 2008).

$\log_{10} I_{\text{I band}}$ ($L_\odot$ pc^{-2}) (1)	σ' (arcsec) (2)	q' (3)
Bulge components		
5.169	0.07	0.38
4.218	0.30	0.74
4.203	0.32	0.38
4.084	0.59	0.74
3.768	0.76	0.74
4.058	1.53	0.74
3.559	3.43	0.74
2.711	3.99	0.74
3.005	14.1	0.74
3.382	6.22	0.74
2.066	59.8	0.74
Disk components		
2.611	4.36	0.38
2.527	18.4	0.38
2.473	45.7	0.38

Table 2.2: MGE parametrization and non parametric bulge/disk decomposition of NGC 1380 I-band surface brigtness distribution. Column (1) lists the central surface brightness, assuming *I* band (HST ACS F814W) ST magnitude of 5.36 mag for the Sun (Willmer, 2018). Column (2) lists the standard deviation along the major axis of each Gaussian. Column (3) lists the axis ratio of each Gaussian.

2.3.3 Distinct Galactic Structures with Gas Kinematics

In Figure 2.13, we show the position velocity diagram (PVD) of observed CO (2-1) emission, extracted from the observed cube with an aperture along the major axis with a

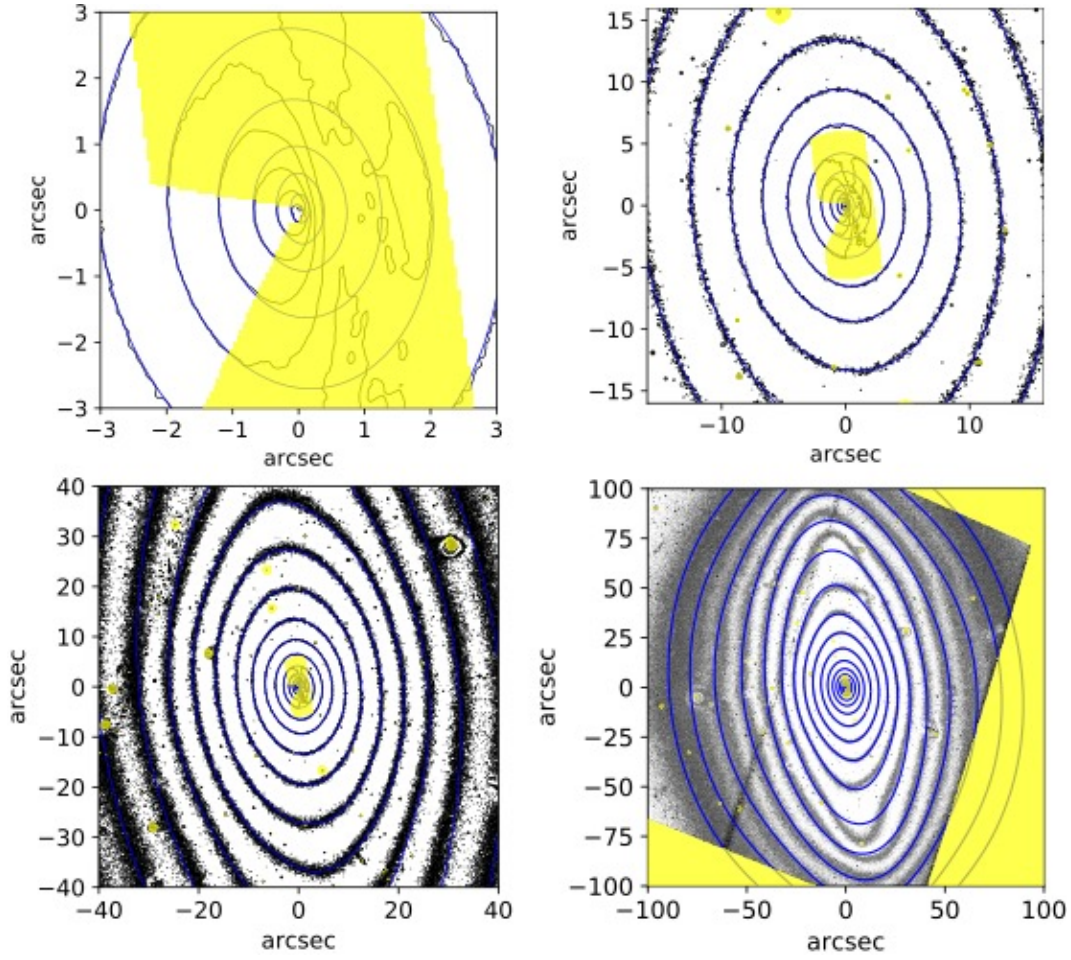

Figure 2.10: HST *I* band (ACS F814W) image of NGC 1380 (black contours), overlaid with our MGE model (blue contours). The yellow shade indicates the masked out region for the MGE fitting to construct the MGE model due to the central dust extinction and fore/background stars and galaxies.

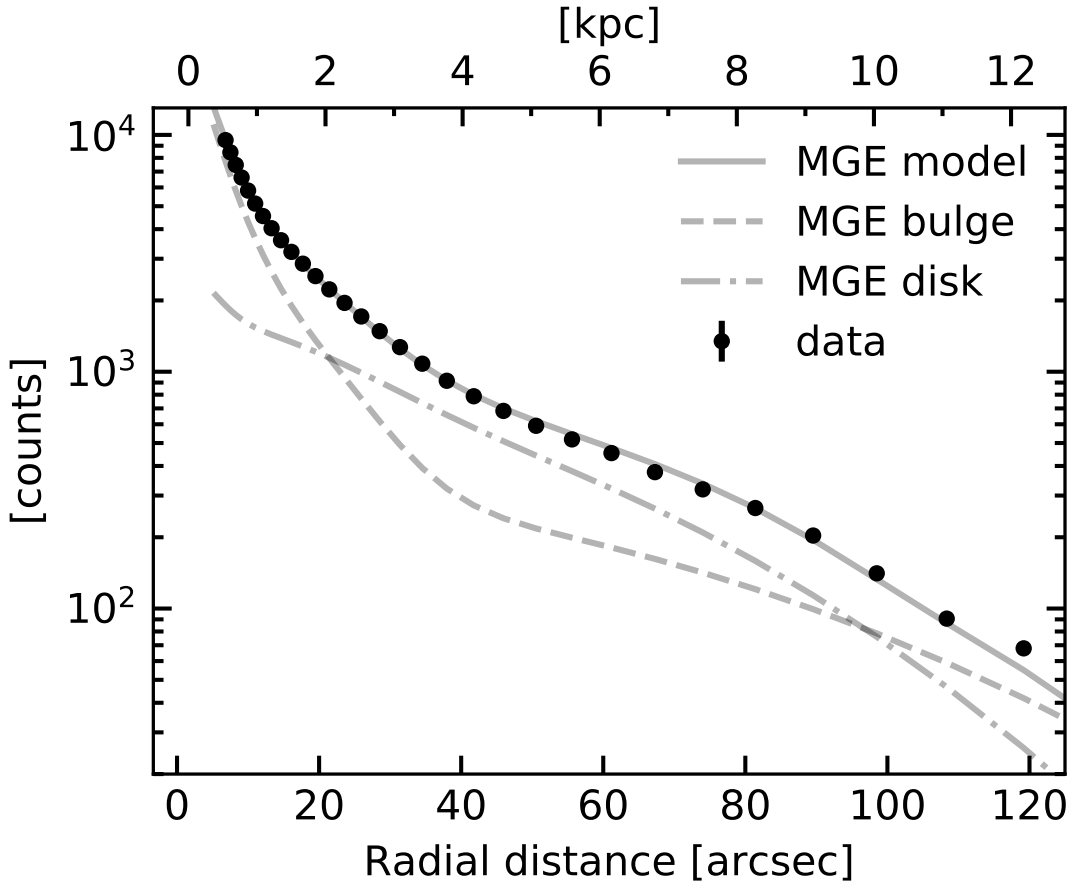

Figure 2.11: Surface brightness profile of the HST I band imaging (black dots), best fit MGE model (thin black solid line), spherical component corresponding to a bulge and stellar halo (axial ratio $q_{\rm bulge}$ of ~ 0.74), and flat component corresponding to a disk (axial ratio $q_{\rm disk}$ of ~ 0.38). The decomposition into spherical and flat components was performed by fitting HST I band image with Gaussians having either of the two unique axial ratios $q_{\rm bulge}$, $q_{\rm disk}$ ($q_{\rm bulge} < q_{\rm disk}$; $q_{\rm bulge}$ and $q_{\rm disk}$ were left free while fitting).

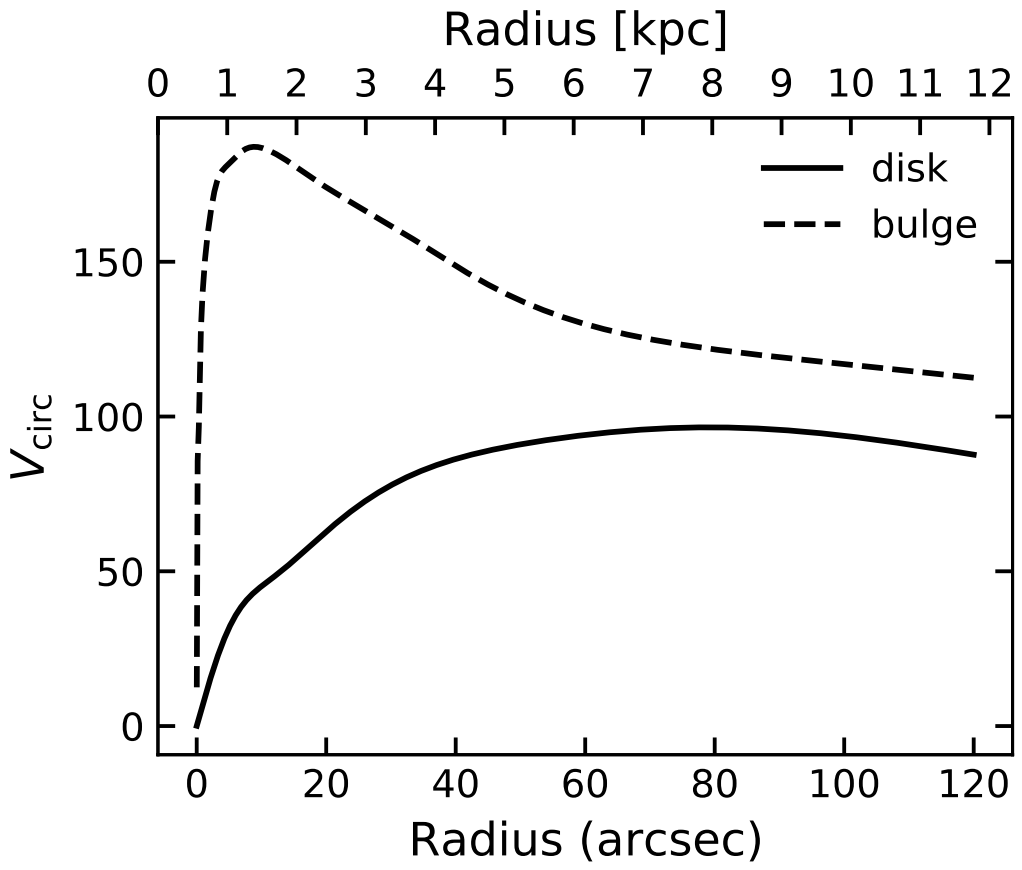

Figure 2.12: Circular velocities of bulge (including halo) and disk components of the best fit MGE model. M/L ratio was assumed to be 1. The peak of the disk circular velocity is found to be at 79.1 arcsec.

width of one beam width. In the center, we can see the quasi-Keplarian upturn in which rotation velocity of CO (2-1) rises sharply in the center (rotation velocity$V_{rot} \propto 1/\sqrt{R}$, where R is the radius from the center), indicating the central black hole dominates the gravitational potential. At the outer region from about 300 pc, the rotation velocity $V_{\rm rot}$ becomes flat ($V_{\rm rot} \propto$ constant), suggesting that the stellar distribution of bulge dominates in the gravitational potential of this region. The constant rotation velocity suggests a density distribution such that the density ρ decreases as $\rho \propto r^{-2}$, which is typical to the central region of galaxies (Cappellari et al., 2013). The velocity width of the CO(2-1) emission in PVD reflects the velocity dispersion that originates from the random motion of the gas clouds. The increase of velocity dispersion in the center is due to the beam smearing effect (Burkert et al., 2016). Since the spatial resolution of the beam is not enough to capture the intrinsic velocity gradient in the center, the velocity is averaged over the beam width resulting in the decrease and increase of velocity gradient and the observed velocity dispersion, respectively. In the outer region, where the beam smearing is less severe, it can be seen that the intrinsic velocity dispersion is $\sim$ 5km/s (see bottom panel of Figure 2.6) much smaller than the rotation velocity, indicating the CO(2-1) line emission arise from the dynamically cold thin disk and its rotation velocity trace the gravitational potential. We will estimate the velocity dispersion of the disk by the detailed modeling of the disk dynamics taking the beam smearing effect into account.

2.4 Result II: Measuring Galactic Mass Distribution

So far, we have seen that HST imaging and VLT/MUSE stellar kinematics consistently reveal the galactic structures, including stellar bulge, disk, and stellar halo. The profile of the root mean square velocity of stars is flat up to a large radius, suggesting the need

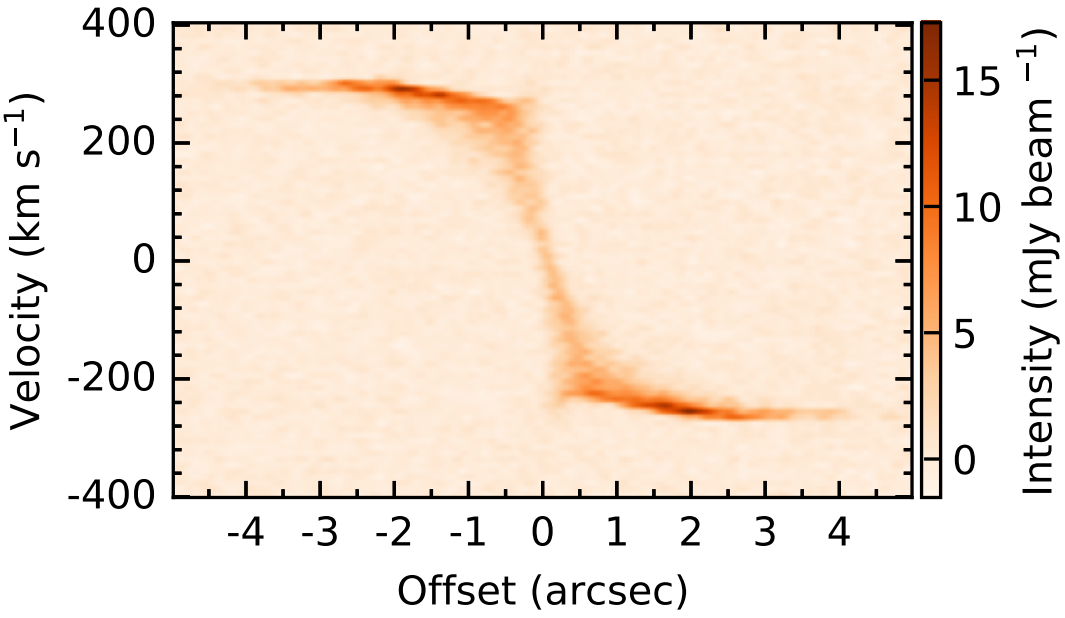

Figure 2.13: PVD of the observed CO(2-1) line emission of NGC 1380. The PVD is produced by extracted from the observed cube along the kinematic major axis with a width of roughly the one beam width (3 pixels, 0.18").

for dark matter in the outer part of the galaxy. Also, ALMA CO (2-1) molecular gas kinematics is dynamically cold and shows the quasi-Keplarian increase, a signature of the central black hole. In this section, we derive the stellar mass (stellar mass to light ratio, given the stellar distribution by HST) and black hole mass accurately by modeling the molecular gas dynamics. Then, with the help of the derived stellar mass and black hole mass in the central region, we aim to estimate the dark matter profile in early-type galaxy NGC 1380 using VLT/MUSE stellar kinematics data, with a large field of view.

2.4.1 Measurement of BH mass and Stellar Mass Distribution Using Gas Kinematics

We used the publicly available KinMS code (Davis, Bureau, et al. 2013) for CO(2-1) gas dynamical modeling. KinMS takes gas intensity distribution and kinematics as an input and generates a model cube, taking observational effects such as beam smearing into account. We produced model cubes with identical synthesized beam, pixel size, velocity resolution to the observed data cube and derived best-fit parameters by directly comparing the model cube and observed data cube (Onishi et al. 2017). We detail gas distribution and kinematics used in KinMS as follows.

Gas Distribution

As in the case of most early-type galaxies (Davis et al., 2013b), the observed CO(2-1) surface brightness distribution of NGC 1380 can be described well by an exponential profile. However, we chose to non-parametrically model the observed gas distribution for accurate gas dynamical modeling. Using SKYSAMPLER (Smith et al., 2019), We generate a set of gas particles on the 2d sky based on the clean model produced by CLEAN algorithm

(equivalent to the psf-deconvolved image). This exactly reproduces the observed CO(2-1) distribution (Intensity map of Figure 2.6) after being convolved by the psf without any model parameters. Then we transform the gas distribution in the 2-dimensional sky to the 3-dimensional physical space (R.A., Dec., distance along the line of sight) with three free parameters (Position angle, Γ, Inclination i), with the assumption that the CO(2-1) disk is thin. The disk center in position and velocity is specified by additional three parameters (R.A. center Δx, Dec. center Δy, velocity center ΔV)

Gas Kinematics

The gravitational potential of a galaxy $\Phi_{\rm gal}$ can be constructed as the sum of potentials of individual mass components, such as a central black hole, bulge and disk, gas disk, dark etc. In the cylindrical coordinate (R,z) at equatorial plane z= 0 under the assumption that the galaxy is axisymmetric, circular velocity $V_{\rm circ} = \sqrt{R\left(\partial\Phi_{\rm gal}/\partial R\right)}$ of the gas particle can be expressed as

$$V^2_{\rm circ}(R) = V^2_{\rm BH}(R) + V^2_{\rm star}(R) + V^2_{\rm DM\ halo}(R) \tag{2.4}$$

,where R is the radius from the galaxy center, and $V_{\rm BH}$ (R), $V_{\rm star}(R)$ and $V_{\rm DM\ halo}$ (R) are the circular velcoity of a test particle at a radius R due to the gravitational potential of the central black hole, star and dark matter. The CO (2-1) is detected at most up to about 0.5 kpc. The contribution of the dark matter halo is generally negligible in central sub-kpc scale for early type galaxies (Cappellari et al., 2013), so we removed $V_{\rm DM\ halo}(R)^2$ in the central CO(2-1) dynamical modeling. $V_{\rm BH}(R)$ is Keplerian $\sqrt{GM_{\rm BH}/R}$, where $M_{\rm BH}$ is the mass of black hole and G is the gravitational constant. $V_{\rm star}(R)$ are calculated from the intrinsic I band luminosity profiles derived from the MGE models (Table 2.2),

where the velocity is scaled with the stellar mass to I band luminosity ratio M/L. After some experimentation, we found that spatially constant mass to light ratio M/L cannot reproduce well the circular velocity of CO(2-1) at radius from 3 arcsec in NGC 1380. Therefore, following North et al. (2019), we adopted spatially varying M/L described by linear function with two free parameters, M/L at center, M/L_0 and at 5 arcsec, $M/L_{5\ \mathrm{arcsec}}$, expressed as

$$M/L(r) = M/L_0 + (M/L_{5\ \mathrm{arcsec}} - M/L_0)(r/5\ \mathrm{arcsec}) \tag{2.5}$$

In the case of spatially constant M/L, the circular velocity can be computed efficiently by mge_vcirc code (Cappellari, 2008) and can be simply scaled by a single M/L. Under spatially varying $M/L(r)$ (equation 2.5), we approximately derived the circular velocity as follows: we first computed spherically averaged luminosity density $\nu(r)$ (mge_radial_density code: Cappellari 2008) and spherically averaged mass density $\rho(r) = \nu(r)M/L(r)$. We then derived circular velocity V_{star} by integrating $\rho(r)$ as $V_{\mathrm{star}}(R) = \sqrt{\frac{G\int_0^R 4\pi r'^2\rho(r')dr'}{R}}$. Although this approximation becomes exact for spherically symmetric system, it provide an accurate circular velocity for our purpose with only 2% error at maximum within 0.6 kpc. The contribution of the molecular gas mass to the circular velocity is not included, because the total estimated gas mass is $\sim 8.4 \times 10^7 M_\odot$ (Boizelle et al., 2017) which is negligible compared to the enclosed mass of $\gtrsim 10^{10} M_\odot$ within CO(2-1) emitting region ($R \sim 500$pc). For the turbulent velocity dispersion of the molecular gas, we adopted spatially constant velocity dispersion σ_{gas} over the disk.

Model Fitting

In summary, model cubes are produced by KinMS code with 8 or 9 free parameters: the inclination i and position angle Γ of the molecular gas disk, the position of the disk center $\Delta x,\ \Delta y,\ \Delta V$, the mass of the central black hole $M_{\rm BH}$ constant stellar mass to I band luminosity ratio M/L or spatially varying $M/L(r)$ with M/L_0 and $M/L_{\rm 5arcsec}$, and velocity dispersion $\sigma_{\rm gas}$. The best-fit parameters and their associated confidence intervals are derived in the Bayesian framework using the emcee code (Foreman-Mackey et al., 2013), which is an implementation of affine invariant MCMC ensemble sampler (Goodman & Weare, 2010). Following recent studies (Onishi et al., 2017), we directly compare the observed cube with the model cube. The posterior distribution of a set of these free parameters θ given data can be written as

$$P(\theta|\mathrm{data}) \propto P(\theta) \times P(\mathrm{data}|\theta), \tag{2.6}$$

where $P(\theta)$ is the prior distribution of the free parameters, and $P(\mathrm{data}|\theta)$ is the likelihood that is the probability of obtaining the data on the given parameters θ. Uniform prior distributions are adopted for all parameters, setting the range much larger than expected from the data. All parameters are sampled in linear space except for the black hole mass $M_{\rm BH}$ which is sampled in log space to cover the multiple orders of magnitude. The likelihood can be written as

$$\begin{aligned} P(\mathrm{data}|\theta) &\propto \exp(-\chi^2(\theta)/2) \\ \chi^2(\theta) &= \Sigma_{i=0}^{N} \left[\left(\frac{I_{\rm data,i} - I_{\rm model,i}}{\sigma_{\rm rms}} \right)^2 \right], \end{aligned} \tag{2.7}$$

where $I_{\rm data,\,i}$ and $I_{\rm model,\,i}(\theta)$ are the intensity of the pixel i in the observed cube and model cube respectively. $\sigma_{\rm rms}$ is the root mean square noise of 0.54 mJy beam^{-1}.

	$\log_{10} M_{\rm BH}$ ($M_\odot$)	M/L_0 ($M_\odot/L_{\odot,I\ \rm band}$)	$M/L_{5\rm arcsec}$ ($M_\odot/L_{\odot,I\ \rm band}$)	$\sigma_{\rm gas}$ (kms^{-1})	i (deg)	Γ (deg)	δx (arcsec)	δy (arcsec)	δV (kms^{-1})	$\chi^2_{\rm red}$
M/L constant	8.520	2.59	-	8.34	76.11	186.89	0.02	0.01	9.62	1.0588
	+0.039	+0.03	-	+1.17	+0.31	+0.26	+0.01	+0.02	+1.07	
	-0.039	-0.03	-	-1.04	-0.32	-0.26	-0.01	-0.01	-1.05	
M/L varying	8.402	2.93	1.75	7.55	76.02	186.81	0.02	0.01	9.82	1.0392
	+0.052	+0.11	+0.25	+1.04	+0.29	+0.25	+0.01	+0.01	+0.95	
	-0.064	-0.11	-0.25	-0.96	-0.30	-0.24	-0.01	-0.01	-0.96	

Table 2.3: The gas dynamical modeling result.

Fitting Result

In the fitting, two cases are considered: M/L is spatially uniform, or M/L is spatially variable with a linear function. The derived best-fit parameters and their confidence intervals are shown in Table 2.3 for both cases. The observed flat rotation velocity at radius about >2.5 arcsec (see Figure 2.14) can be reproduced with spatially variable M/L but not with spatially constant M/L. Also, the spatially variable case is preferred in terms of χ^2 statistics. So, we adopt the result of spatially variable M/L as best-fit model for later discussion. Its posterior distributions and covariance matrix is shown in Figure 2.15. Figure 2.16 shows the intensity and velocity images which are made from the best-fit model cube and the observed data cube, as well as the residual maps (data - model), demonstrating that the best-fit model is in good agreement with the observed data. Figure 2.14 shows the position velocity diagram extracted from the model cube overlaid on that extracted from the observed cube. The central rise of the velocity is well reproduced by the central BH with a mass of $2.52^{+0.32}_{-0.35} \times 10^8 M_\odot$. The estimated BH masses only lowered by 0.12 dex when using spatially varying M/L rather than constant M/L (Table 2.3).

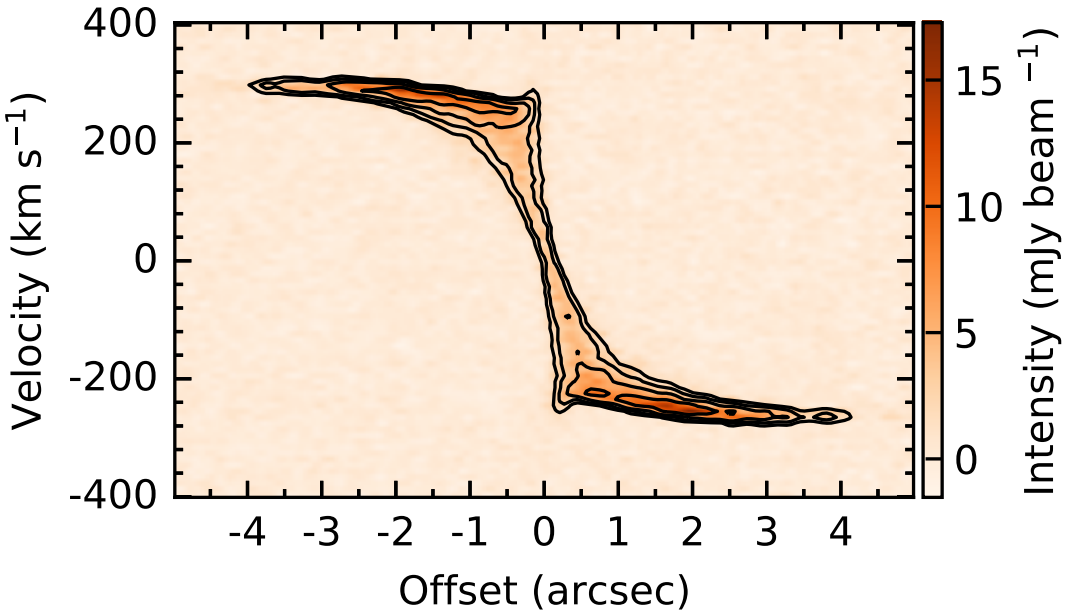

Figure 2.14: Observed PVD of CO(2-1) line emission of NGC 1380 (orange) and model PVD (black contours).

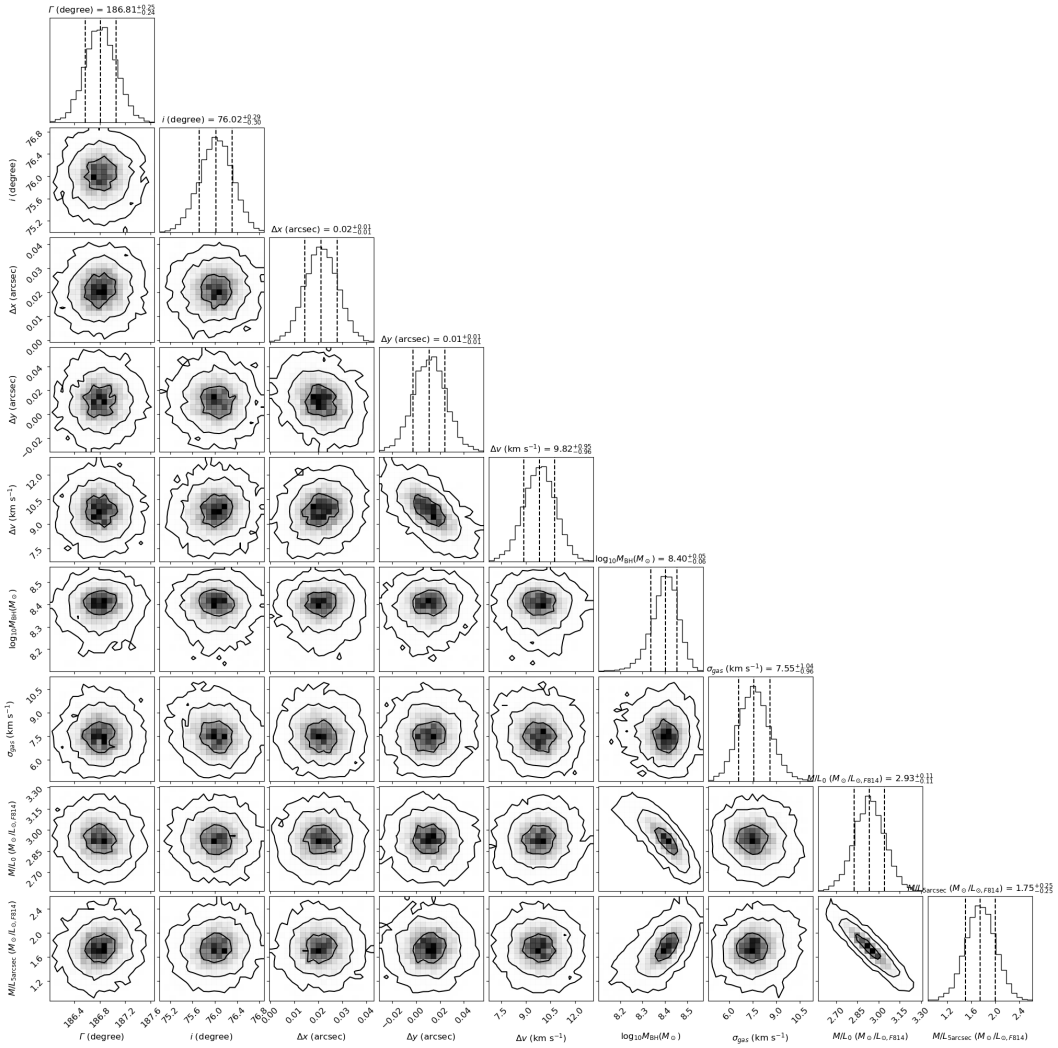

Figure 2.15: Posterior distributions of 9 model parameters by MCMC sampling of CO(2-1) dynamical model (spatially variable M/L). The histograms of marginalized posterior distributions are shown along the diagonal panels. The dashed vertical lines in histograms are the 16th, 50th, and 84th percentiles. The derived values of eight model parameters are indicated above the histogram, summarized in Table 2.3. The panels except for these histograms show the covariances between all model parameters (contour levels are equivalent to 68%, 95% and 99.7% confidence intervals for the 2D Gaussian distribution).

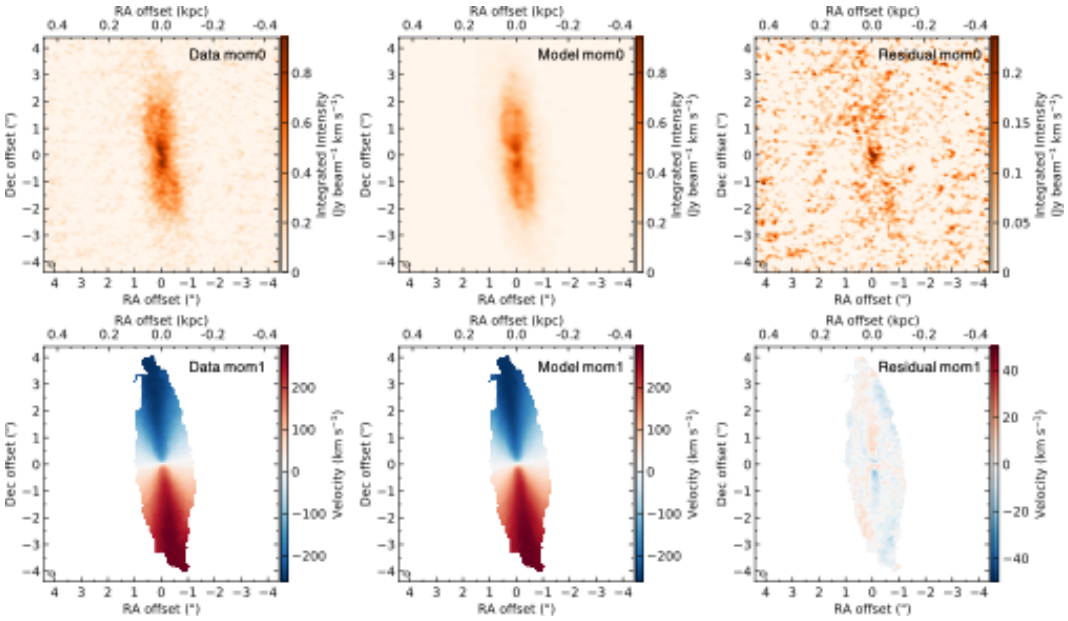

Figure 2.16: Intensity (moment 0) and velocity (moment 1) images of CO(2-1) emission, which were made from the observed data cube (left top and bottom) and the best-fit model cube (middle top and bottom), as well as the residual maps (data - model; right top and bottom)

2.4.2 Measurement of Stellar and Dark Matter Mass Distribution Using Stellar Kinematics

Gas dynamical modeling enables us to derive the BH mass and the stellar mass distribution within ~ 500pc. Using this central mass distribution and wide-field-of-view stellar kinematics data, we aim to quantitatively estimate the mass distribution, including dark matter halo, out to about 12 kpc. The galactic gravitational potential $\Phi_{\rm gal}$ can be expressed as

$$\Phi_{\rm gal} = \Phi_{\rm BH} + \Phi_{\rm stars} + \Phi_{\rm DM\ halo}, \tag{2.8}$$

where $\Phi_{\rm BH}$, $\Phi_{\rm stars}$, $\Phi_{\rm DM\ halo}$ are gravitational potential of BH, stars, and dark matter halo, respectively. In order to model the stellar kinematics under the gravitational potential and fit to the observed kinematics (e.g. line-of-sight root-mean-square velocity $V_{\rm rms} = \sqrt{V^2 + \sigma^2}$; Figure 2.3 bottom), we utilized Jeans Anisotropic Modeling (JAM; Cappellari 2008, 2020). JAM provides efficient axisymmetric solution of Jeans equations assuming that the stellar system reached equilibrium and is in steady state under the smooth gravitational potential. JAM is based on two assumptions for Jeans equation to be closed: the velocity ellipsoid is aligned to the cylindrical polar coordinates (R, z, ϕ) (Hereafter JAM$_{\rm cyl}$; Cappellari 2008) or spherical polar coordinates (r, θ, ϕ) (Hereafter JAM$_{\rm sph}$; Cappellari 2020); and the orbital anisotropy $\beta = 1 - (\sigma_z/\sigma_R)$ for JAM$_{\rm cyl}$ or $\beta = 1 - (\sigma_\theta/\sigma_r)$ for JAM$_{\rm sph}$.

For convenience, we briefly summarize the formula and solution of Jeans equations, JAM$_{\rm cyl}$ and JAM$_{\rm sph}$ in subsection 1.2.1. Required inputs for the solution of Jeans equations are luminosity density of kinematic tracer (stars in this study), anisotropy parameter β, and mass density (for calculating gravitational potential under which stars archive equilibrium). The luminosity density of stars is already parameterized by MGE (see Table 2.2). In the next subsections, we describe the details of the parametrization for the anisotropy parameter β and the unknown mass density structure of galaxies.

Velocity orbital anisotropy

Previous studies have adopted a spatially constant β when modeling early-type galaxies (Cappellari et al., 2013). However, both stellar photometric and kinematic data suggest the presence of distinct stellar structures: rotation-supported flat structure like a disk and spherical structure like a bulge and stellar halo (see for example Figure 2.9). Therefore, we allow the spatial variation of β in the galaxy by assigning different β to the spherical

MGE component (bulge and stellar halo, $\beta_{\rm bulge}$) and the flat MGE component (disk, $\beta_{\rm disk}$). The luminosity distribution of stars in the galaxy is described by the superposition of those of spherical structure $\nu_{\rm bulge}$ and the flat structure $\nu_{\rm disk}$. The orbital anisotropy beta at a given point in the galaxy $\beta(R,z)$ is described by the sum of the $\beta_{\rm bulge}$ and $\beta_{\rm bulge}$ weighted by their respective luminosity distribution $\nu_{\rm bulge}$ and $\nu_{\rm disk}$ as (Cappellari, 2008)

$$\begin{aligned}\beta(R,z) \equiv 1 - \frac{\sigma_z^2(R,z)}{\sigma_R^2(R,z)} &= 1 - \frac{\nu_{\rm bulge}(R,z)\sigma_{z\,\rm bulge}^2(R,z) + \nu_{\rm disk}(R,z)\sigma_{z\,\rm disk}^2(R,z)}{b_{\rm bulge}\nu_{\rm bulge}(R,z)\sigma_{z\,\rm bulge}^2(R,z) + b_{\rm disk}\nu_{\rm disk}(R,z)\sigma_{z\,\rm disk}^2(R,z)} \\ &\approx 1 - \frac{\nu_{\rm bulge}(R,z) + \nu_{\rm disk}(R,z)}{b_{\rm bulge}\nu_{\rm bulge}(R,z) + b_{\rm disk}\nu_{\rm disk}(R,z)},\end{aligned} \tag{2.9}$$

where $b_{\rm bulge} = 1/(1-\beta_{\rm bulge})$ and $b_{\rm disk} = 1/(1-\beta_{\rm disk})$. The last approximation is due to the fact that σ_z^2 depends on the total galactic potential and the spatial variation is much smaller than ν. In this way, we reproduce the continuous variation of anisotropy $\beta(R,z)$ in the galaxy with two free parameters, $\beta_{\rm bulge}$ and $\beta_{\rm disk}$. Cappellari et al. (2007) found that all fast rotating early type galaxies have anisotropy $\beta = 1 - (\sigma_z/\sigma_R)^2 > 0.05$ and a positive correlation between anisotropy β and the flatness of the galaxies. These results motivate us to set the boundaries $0.05 < \beta_{\rm disk} < 1$ for flat rotating structure like a disk, while $-1 < \beta_{\rm bulge} < 1$ for spherical structures like a bulge and halo to have tangentially biased orbits $\beta_{\rm bulge} < 1$, $\sigma_z > \sigma_R$.

Gravitational Potential of the Galaxy

We describe each mass component of the galaxy contributing to the galactic potential. For stellar components, we consider the M/L variation within 500 pc suggested by the gas dynamical modelling. In order to extrapolate and apply the M/L variation to larger

radius ~120 kpc, we modified eq 2.5 as

$$M/L\,(r) = \begin{cases} M/L_0 + (M/L_{5\text{arcsec}} - M/L_0)(r/5\text{arcsec}), & \text{if } r \leq r_{\text{break}} \\ M/L_0 + (M/L_{5\text{arcsec}} - M/L_0)(r_{break}/5\text{arcsec}), & \text{otherwise} \end{cases} \tag{2.10}$$

,where M/L decreases in proportion to the radius r inside the break radius r_{break}, and is constant beyond that radius. If we simply extrapolate the M/L variation estimated at the center to a larger radius, the M/L ratio would be zero at 9 to 17 arcsec. So, in order to make sure that the M/L is in the physically acceptable range, we limited r_{break} in a range of 5<r_{break}<16 arcsec for the fitting. Such a simple trend of stellar M/L variation is suggested from spectral data in early type galaxies, which show a sharp decrease at the center and an approximately constant value from the outer radius of about 0.4 effective radius (van Dokkum et al., 2017).

For dark matter halo potential, $\Phi_{\text{DM halo}}$ we have used NFW dark matter halo density profile (Navarro et al., 1997)

where ρ_s is density at break radius r_s. This profile has a double-power-law shape: $\rho(r) \propto r^{-1}$ inside of r_s ($r \ll r_s$), and $\rho(r) \propto r^{-3}$ outside ($r \gg r_s$). In stead of the two parameters r_s and ρ_s that uniquely characterize the density profile, we can use the virial radius of halo M_{200} and concentration of halo c, because of the two equation relates between (ρ_s, r_s) and (M_{200}, c),

$$\begin{aligned} \rho_s &= \frac{M_{200}}{16\pi r_s^3(\log(1+c)-c/(1+c))} \\ r_s &= (\frac{M_{200}G}{100H_0^2})^{\frac{1}{3}}/c. \end{aligned} \tag{2.11}$$

We reduce the number of free parameters to one parameter M_{200} using the virial

mass and concentration $M_{200} - c_{200}$ relation derived by Dutton & Macciò (2014).

Model Fitting

In summary, the second-order moment of stars are computed by JAM with 8 free parameters, inclination i, anisotropy parameter $\beta_{\rm bulge}$ and $\beta_{\rm disk}$, black hole mass $M_{\rm BH}$, three parameters to describe $M/L(r)$: M/L_0, $M/L_{\rm 5arcsec}$, and $r_{\rm break}$, and virial mass of NFW halo M_{200} The computed second-order moment of stars is fitted to observed root-mean-square velocity $V_{\rm rms} = \sqrt{V^2 + \sigma^2}$ in the Bayesian framework using the same procedure as gas dynamical modeling described in subsection 2.4.1. Four of the free parameters: inclination i, black hole mass $M_{\rm BH}$, M/L_0 and $M/L_{\rm 5arcsec}$ are already derived by the gas dynamical modelling, so we used Gaussian prior with their median values and confidence intervals. We use uninformative flat prior distribution for others. All parameters are sampled in linear space except for the black hole mass $M_{\rm BH}$ and $M_{\rm DM}$ which is sampled in log space in order to cover the multiple orders of magnitude. The likelihood can be written as

$$\begin{aligned} P(\mathrm{data}|\theta) &\propto \exp(-\chi^2(\theta)/2) \\ \chi^2(\theta) &= \Sigma_{i=0}^{\rm N} \left[\left(\frac{V_{\rm rms,i} - \langle v_{\rm los}^2 \rangle_{\rm i}^{1/2}(\theta)}{\epsilon_{V_{\rm rms,i}}} \right)^2 \right] \end{aligned} \tag{2.12}$$

where $\varepsilon_{V_{\rm rms},i}$ is the error of the observed root-mean-square velocity $V_{{\rm rms},i} = \sqrt{V_i^2 + \sigma_i^2}$, and $\langle v_{\rm los}^2 \rangle_i$ is second moment computed by JAM model at each spatial position i. The error of the observed root-mean-square velocity $\varepsilon_{V_{\rm rms},i}$ is computed considering the error propagation as

$$\varepsilon_{V_{\rm rms},i} = \frac{\sqrt{\left(V_i \varepsilon_{V,i}\right)^2 + \left(\sigma_i \varepsilon_{\sigma,i}\right)^2}}{V_{{\rm rms},i}}, \tag{2.13}$$

where $\varepsilon_{V,i}$ and $\varepsilon_{\sigma,i}$ is error on mean velocity V_i, and velocity dispersion σ_i, respectively. In order to avoid the parameters from being influenced too much by the high-S/N pixels in the center, following prescription by Mitzkus et al. (2017), we adopt a constant value of $\varepsilon_{V,i} = 5\mathrm{km\ s^{-1}}$ and constant fraction of $\varepsilon_{\sigma,i} = 0.07\sigma_i$. The fraction of 0.07 is chosen so that the error of the velocity dispersion is not smaller than that of the mean velocity. These are consistent with the median error of mean velocity 5km $\mathrm{s^{-1}}$ and velocity dispersion of 6km $\mathrm{s^{-1}}$ reported in Sarzi et al. (2018).

Fitting Result

Figures 2.17 and 2.18 show the best-fit Jeans equation-based models of stellar kinematics with two different velocity anisotropy assumptions, $\mathrm{JAM_{cyl}}$ and $\mathrm{JAM_{sph}}$ respectively, and their comparison with the observed data $V_{\mathrm{rms}} = \sqrt{V^2 + \sigma^2}$. Figures 2.19 and 2.20 show the posterior probability distributions of the 8 model parameters along with the prior distributions that are the result of ALMA gas modeling for $\mathrm{JAM_{cyl}}$ and $\mathrm{JAM_{sph}}$ respectively. These results are summarized in Table 2.4 and 2.5. The $\mathrm{JAM_{cyl}}$ result is inconsistent with the measured mass distribution obtained by ALMA (central 5 arcsec), with overall larger values of stellar-mass-to-light ratio and black hole mass. On the other hand, $\mathrm{JAM_{sph}}$ result converges closer to the central mass distribution derived by ALMA than $\mathrm{JAM_{cyl}}$. This may suggest that the model assumption of the spherically aligned velocity ellipsoid may be more appropriate in the central region than cylindrically aligned velocity ellipsoid. Under the nearly spherical gravitational potential of the bulge and the central black hole in the center or dark matter halo in the outer part of the galaxies, the orbit of the star is close to the planer orbit, and the velocity ellipsoid is expected to be spherically aligned (Cappellari, 2020). In $\mathrm{JAM_{cyl}}$, the anisotropy for the disk structure β_{disk} hits the boundary of 0.05 and favors lower values. $\mathrm{JAM_{sph}}$ results in

$\beta_{\rm disk}$ ~0.67, indicating that the velocity ellipsoid is anisotropic ($\sigma_R > \sigma_z$), which is consistent with the observation that the flatter structure have more anisotropic velocity ellipsoid (i.e., larger β; Cappellari et al. 2007). The JAM$_{\rm sph}$ archives total $\chi^2 = 30733.3$ and $\chi^2_\nu = 1.628$ with the degree of freedom of $N_{\rm dof} = 18878$, which is significantly preferable over the the results JAM$_{\rm cyl}$ with total $\chi^2 = 32125.7$ and $\chi^2_\nu = 1.702$. Therefore, we discuss the result of JAM$_{\rm sph}$ as the best fit model for NGC 1380.

We utilize prior constraints of the central mass distribution measured by modeling gas kinematics, which may help to mitigate the mass anisotropy degeneracy in the central region. In the covariance maps (Figure 2.20), bulge anisotropy $\beta_{\rm bulge}$ is well constrained without significant correlations with parameters which determine the central mass distribution such as $(M/L)_0$, $(M/L)_{\rm 5arcsec}$ and $M_{\rm BH}$. We can see the correlation between the disk velocity anisotropy $\beta_{\rm disk}$ and the mass of the dark matter halo because the disk-dominated region does not overlap with the ALMA data, but two parameters are well constrained. Although significant correlation between $M/L_{5arcsec}$ and $r_{\rm break}$ can be seen, the shape of overall M/L ratio variation is constrained as shown in Figure 2.21 for JAM$_{\rm sph}$. Interestingly, the M/L ratio has a large scatter in the outer regions of the galaxy but shows only little correlation with dark matter mass M_{200}, suggesting that the dark matter distribution does not significantly depend on the M/L and mostly constrained by the stellar kinematics data at large radii. Figure 2.22 shows the resulting cumulative mass distribution and dark matter fraction as a function of radius, with the dark matter fraction of $0.55^{+0.05}_{-0.05}$ at the peak radius of the disk circular velocity (Table 2.6).

The stellar M/L estimated from the stellar kinematics is up to ~25% (2.2σ) larger than the M/L constrained by ALMA data (~ 2 to 4 arcsec, see Figure 2.21).

This overestimation is consistent with the general trends suggested by Thater et al. (2020) that the black hole masses estimated by stellar kinematics seem to be

systematically larger than those estimated by gas kinematics. Even with the difference in spatial resolution between steller kinematics (0.9" in FWHM) and gas kinematics (0.25" $\times$ 0.18" in FWHM), the discrepancy between our mass distributions estimated by stellar and gas kinematics (~25%) is fairly small compared to the discrepancy reported up to a factor of four in black hole masses (e.g., Pinkney et al., 2020; Barth et al., 2016b; Walsh et al., 2013, 2012). This may suggest that it is effective to incorporate the constraints on the central mass distribution derived by the gas kinematics into the modeling of stellar kinematics as a prior distribution for reconciling the discrepancy between the estimated mass distributions by gas and stellar kinematics.

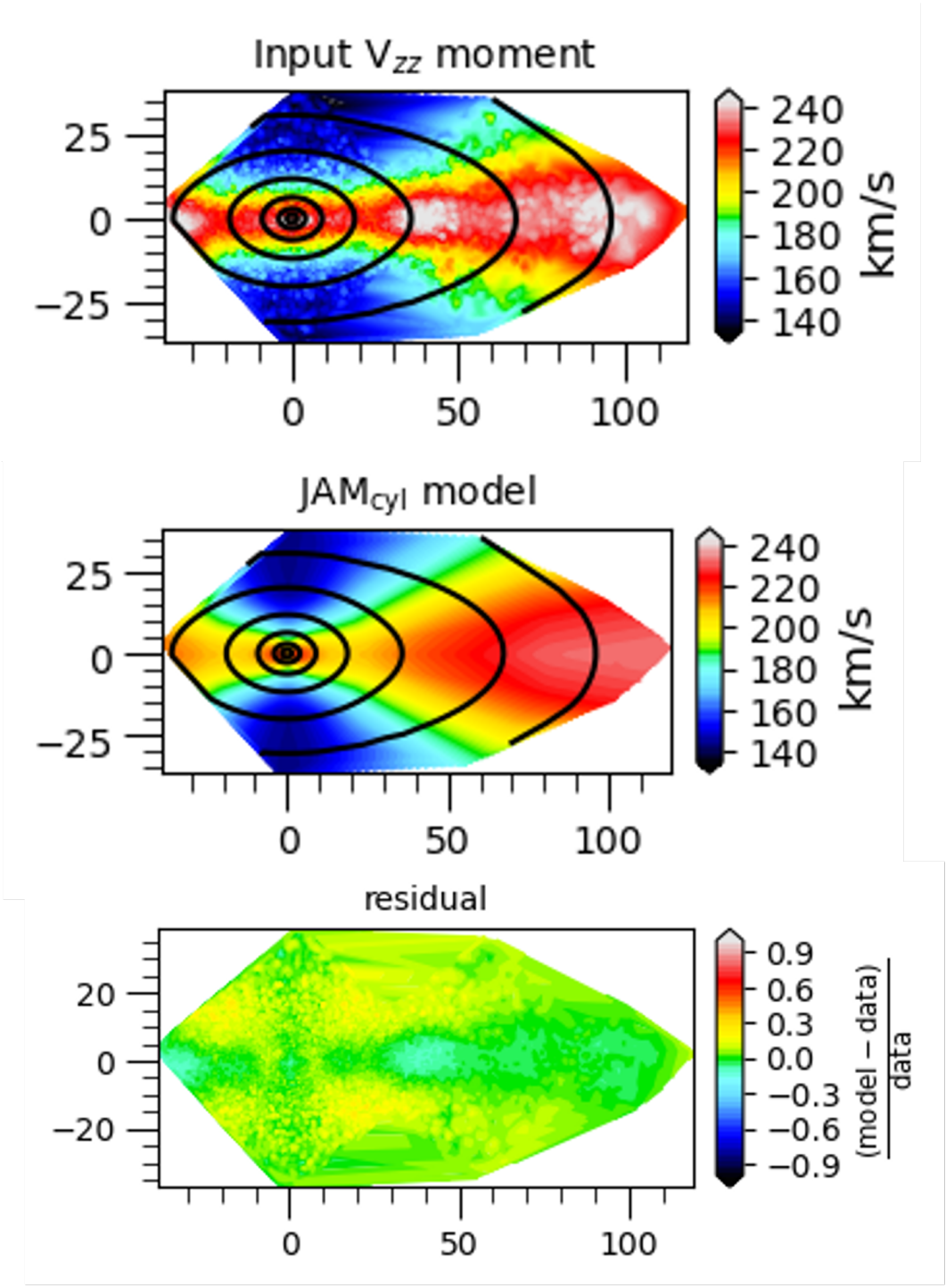

Figure 2.17: Comparisons between observed root-mean-velocity $V_{\mathrm{rms},i} = \sqrt{V_i^2 + \sigma_i^2}$ (top panel) and the best-fit $\mathrm{JAM_{cyl}}$ model (middle panel). Bottom panel shows the residual between the model and data.

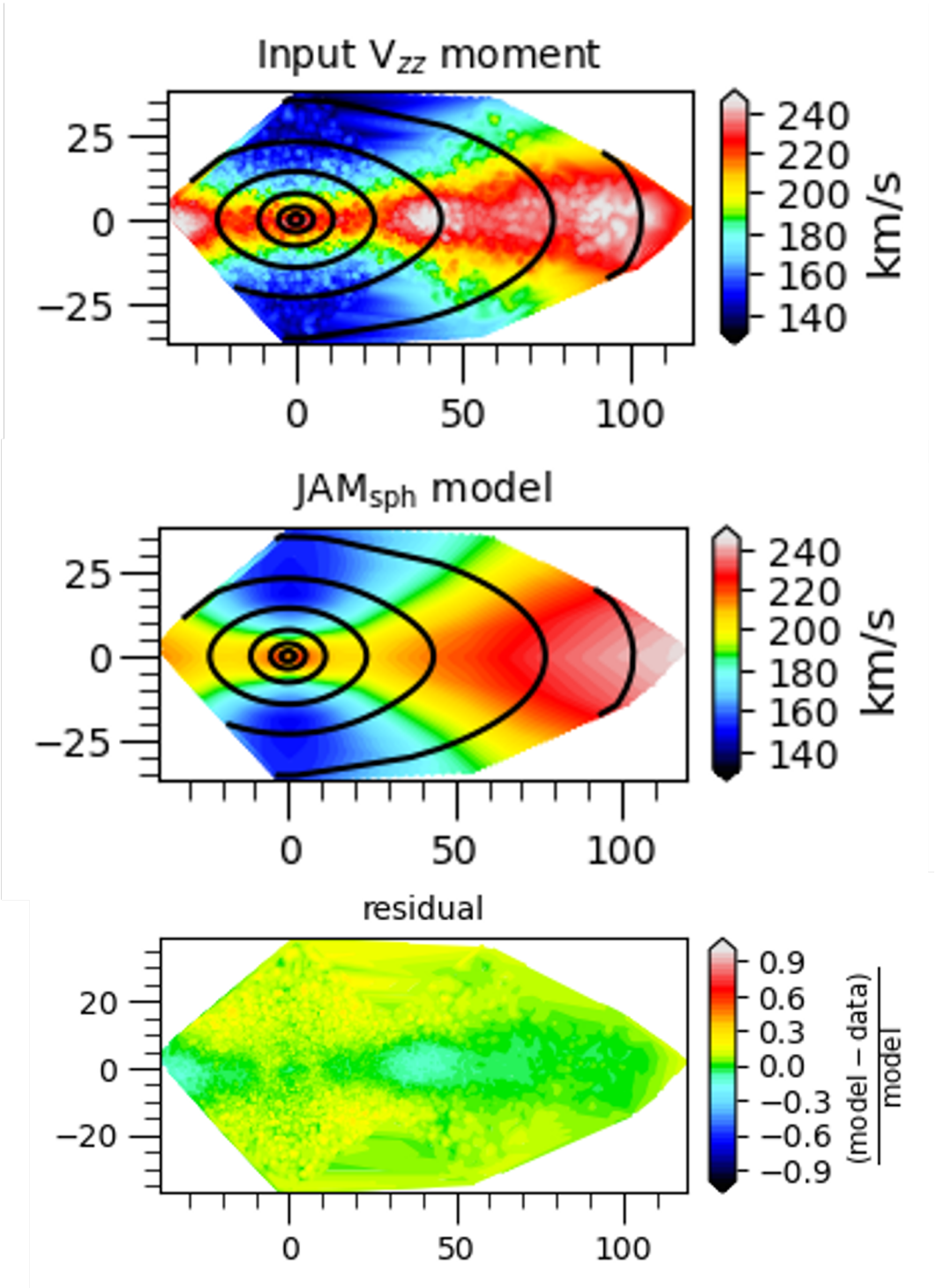

Figure 2.18: Comparisons between observed root-mean-velocity $V_{\mathrm{rms},i} = \sqrt{V_i^2 + \sigma_i^2}$ (top panel) and the best-fit JAM_{sph} model (middle panel). Bottom panel shows the residual between the model and data.

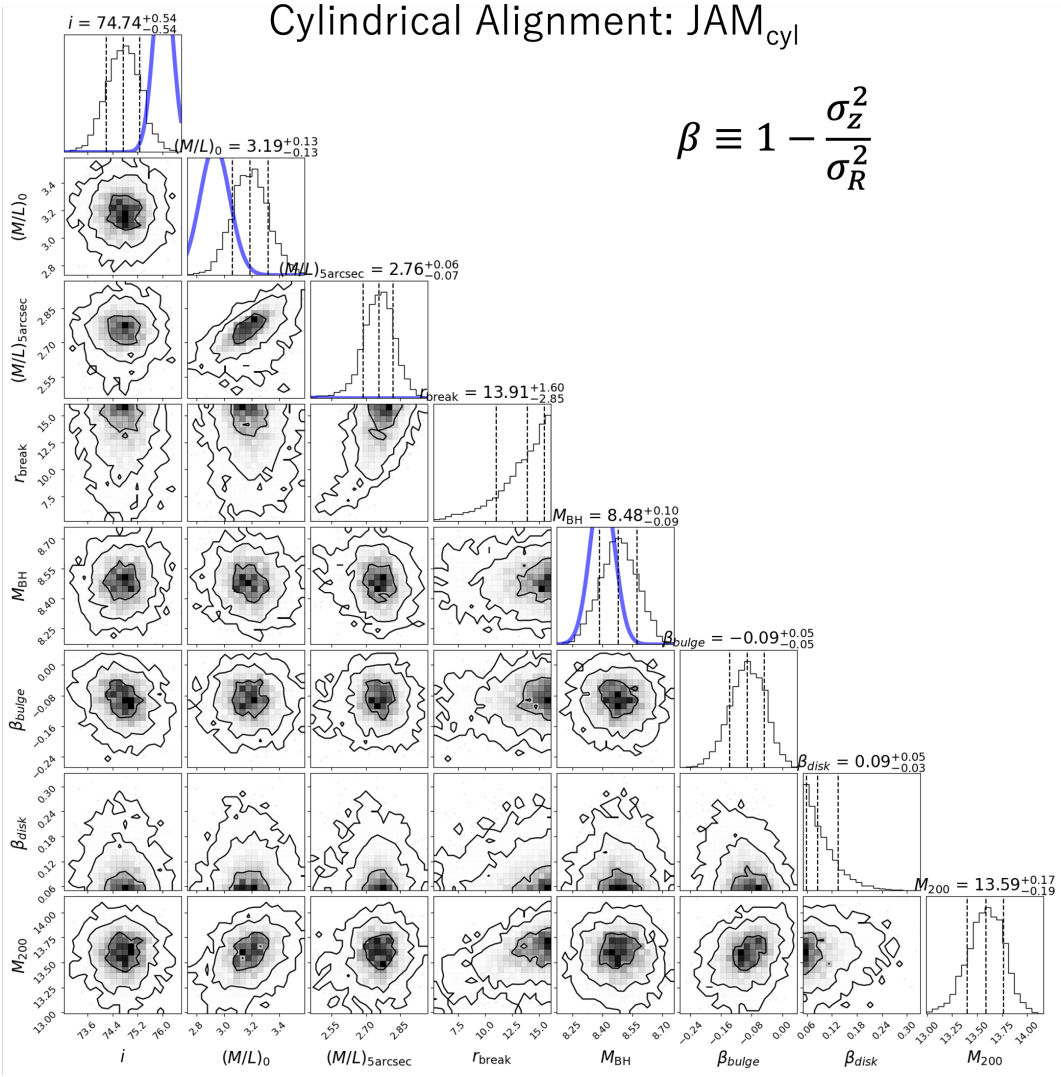

Figure 2.19: Posterior probability distributions of the 8 model parameters of our Jeans equation-based model JAM$_{cyl}$. Histograms of marginalized distributions for each parameter are shown along the diagonal panels with the Gaussian prior distribution from the ALMA gas dynamical modeling results (blue line). The dashed vertical lines in these histograms are the 16th, 50th, and 84th percentiles (68% confidence interval). The derived values of 8 model parameters are indicated above the histogram, summarized in table 2.4. The other panels show the covariances between all model parameters (contour levels are equivalent to 68%, 95% and 99.7% confidence intervals for the 2D Gaussian distribution).

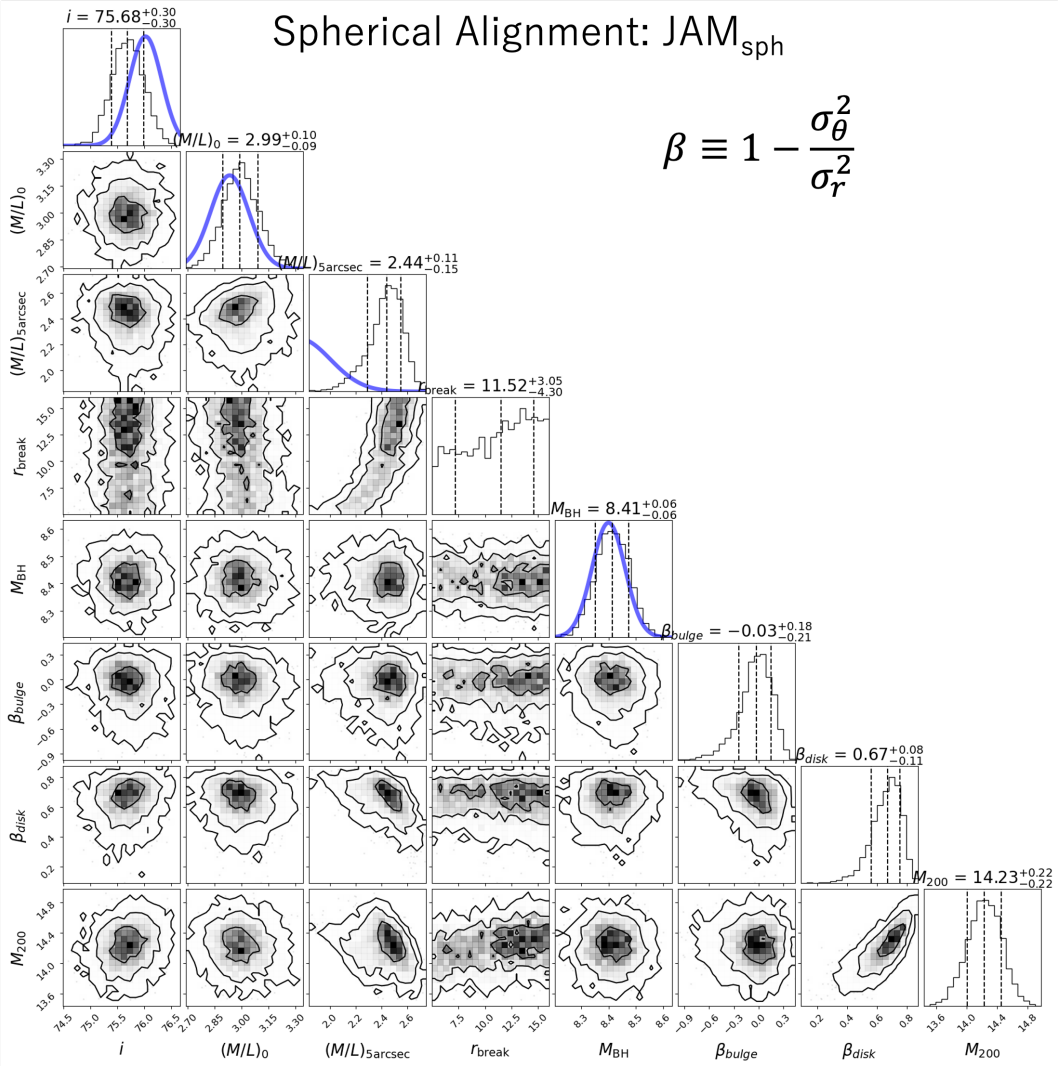

Figure 2.20: Posterior probability distributions of the 8 model parameters of our Jeans equation-based model JAM$_{sph}$. A histogram of marginalized distribution for each parameter is shown along the diagonal panels with the Gaussian prior distribution from the ALMA gas dynamical modeling results (blue line). The dashed vertical lines in these histograms are the 16th, 50th, and 84th percentiles (68% confidence interval). The derived values of 8 model parameters are indicated above the histogram, summarized in table 2.5. The other panels show the covariances between all model parameters (contour levels are equivalent to 68%, 95% and 99.7% confidence intervals for the 2D Gaussian distribution).

JAM_{cyl} NFW model	(unit)	median	best	upper	lower	prior
inclination	degree	74.74	74.94	0.54	0.54	(76.02+/-0.3)
M/L_0	$M_\odot/L_{I,\odot}$	3.19	3.14	0.13	0.13	(2.93+/-0.11)
$M/L_{5\ \mathrm{arcsec}}$	$M_\odot/L_{I,\odot}$	2.76	2.77	0.06	0.07	(1.75+/-0.25)
r_{break}	arcsec	13.91	15.83	1.60	2.84	[5.0,16.0]
BH mass	$M_\odot$(log)	8.48	8.50	0.10	0.09	(8.4+/-0.06)
β_{disk}	-	-0.09	-0.08	0.05	0.05	[-1.0,1.0]
β_{bulge}	-	0.09	0.05	0.05	0.03	[0.05,1.0]
M_{200}	$M_\odot$(log)	13.59	13.69	0.17	0.19	[11.0,15.0]

Table 2.4: The stellar dynamical modeling result using cylindrical JAM model.

JAM_{sph} NFW model	(unit)	median	best	upper	lower	prior
inclination	degree	75.68	75.63	0.30	0.30	(76.02+/-0.3)
M/L_0	$M_\odot/L_{I,\odot}$	2.99	2.96	0.10	0.09	(2.93+/-0.11)
$M/L_{5\ \mathrm{arcsec}}$	$M_\odot/L_{I,\odot}$	2.44	2.49	0.11	0.15	(1.75+/-0.25)
r_{break}	arcsec	11.52	15.51	3.05	4.30	[5.0,16.0]
BH mass	$M_\odot$(log)	8.41	8.39	0.06	0.06	(8.4+/-0.06)
β_{disk}	-	-0.03	0.02	0.18	0.21	[-1.0,1.0]
β_{bulge}	-	0.67	0.68	0.08	0.11	[0.05,1.0]
M_{200}	$M_\odot$(log)	14.23	14.39	0.22	0.22	[11.0,15.0]

Table 2.5: The stellar dynamical modeling result using spherical JAM model.

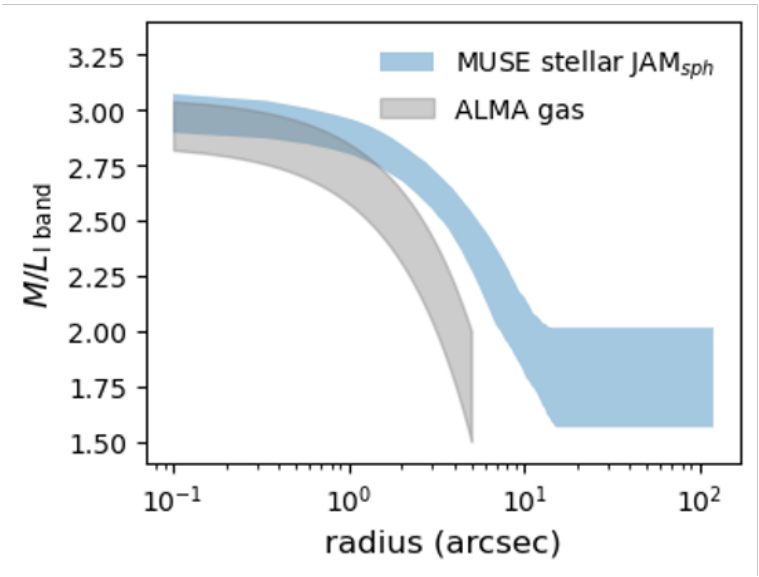

Figure 2.21: The M/L ratio variation in NGC 1380 estimated by ALMA molecular gas modeling (gray shade) and MUSE stellar kinematics modeling with JAM_{sph} (blue shade). Note that we used the M/L in the central region of the galaxy (gray shade), derived from ALMA gas kinematics, as a prior distribution to estimate the M/L for the entire galaxy (blue shade) using MUSE stellar kinematics. The shaded regions encompass the 68% confidence interval.

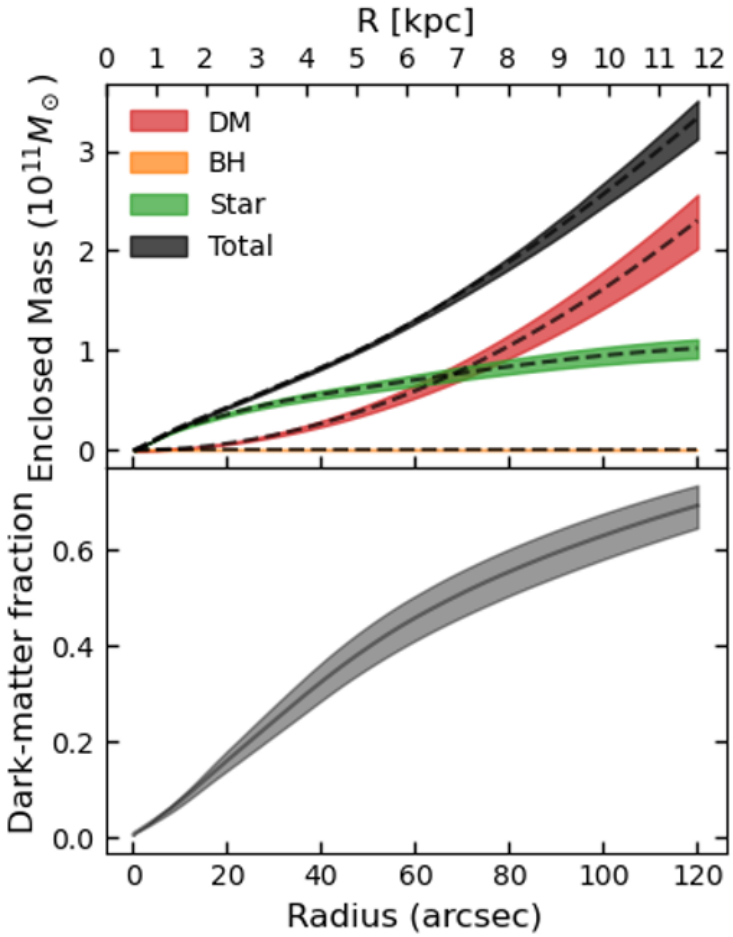

Figure 2.22: The enclosed mass distribution (top) and dark matter fraction (bottom) of NGC 1380 as a function of radius estimated by MUSE stellar kinematics modeling with $\mathrm{JAM}_{\mathrm{sph}}$. Shaded regions encompassing the median lines indicate the 68% confidence interval.

2.5 Discussion of This Chapter

2.5.1 Internal structures of NGC 1380

Table 2.6 summarizes the structural parameters of NGC 1380 derived by MGE nonparametric decomposition of bulge and disk (Section 2.3.2) and dynamical modeling (Section 2.3.2), compared with the results of traditional parametric bulge-disk decomposition (Sersic profile for bulge and exponential profile for disk; Bedregal et al. 2006). Our bulge-to-total ratio and bulge effective radius are $\sim$ 10% and 1.6 times larger than those derived by parametric decomposition. Since our decomposition is non-parametric and fully based on the axial ratio of the structures, our bulge component effectively includes the stellar halo component in the outer part of the galaxy. The scale length of the disk $R_{\rm d}$, defined for exponentially declining profile as the radius at which the brightness falls off by a factor of e from the center, is ill-defined and has an ambiguous physical meaning for our non-parametric disk model. Therefore, we have redefined and estimated the scale length for our disk in terms of the gravitational contribution of the disk to the dynamics of the galaxy. By analogy with the exponential disk, whose peak of the circular velocity is at $2.2R_{\rm d}$ ($R_{\rm d}$ is the disk scale length) and the fact that the peak of our disk circular velocity is found to be at the radius of 79.1 arcsec (see 2.12), scale-length $R_{\rm d}$ of our non-parametric disk is estimated to be 36.0 arcsec, which is consistent with that of the disk obtained by parametric decomposition.

Based on the tensor virial theorem, the ellipticity of an oblate spheroidal stellar structure is determined by the kinetic energy of the bulk rotational motion around the symmetry axis and those of random motions in the symmetric axis and radial (major) axis (Binney & Tremaine, 2008). The orbital anisotropy β quantifies the ratio of random kinetic energies in the symmetric and radial axes, which is expected to correlate with the

ellipticity of the structure and has been confirmed observationally (Cappellari et al., 2007). Figure 2.23 show the anisotropy $\beta \equiv 1 - (\sigma_z/\sigma_R)^2$ as a function of intrinsic ellipticity $\epsilon_{\rm intr}$ for early-type galaxies obtained by Cappellari et al. (2007) with our measurements, approximately equivalent quantity $\beta \equiv 1 - (\sigma_\theta/\sigma_r)^2$ and $\epsilon_{\rm intr}$ for disk and bulge structure of NGC 1380. Our measured β for the bulge and disk are consistent with the general trend that the flatter structures have larger anisotropy. Furthermore, our results may indicate even stronger correlations between β and $\epsilon_{\rm intr}$, deviating from the average trend obtained by Cappellari et al. (2007) galaxy sample. β and $\epsilon_{\rm intr}$ measured in Cappellari et al. (2007) is averaged quantities over the entire galaxy. On the other hand, in this study, bulge and disk structures were separated and β was measured for each structure, allowing us to measure the intrinsic β of the bulge and disk structures.

	Name	(unit)	derived value in this study	Bedregal et al. (2006)
(1)	$(B/T)_{\rm light}$	-	0.68	$0.58^{+0.01}_{-0.01}$
(2)	$(B/T)_{\rm mass}$	-	$0.70^{+0.01}_{-0.01}$	-
(3)	$\log M_{\rm bulge}$	$M_\odot$	$10.89^{+0.04}_{-0.03}$	-
(4)	R_e	arcsec	28.35	$17.6^{+0.4}_{-0.3}$
(5)	$\epsilon_{\rm bulge}$	-	0.28	-
(6)	$\log M_{\rm disk}$	$M_\odot$	$10.53^{+0.05}_{-0.06}$	-
(7)	$R_{\rm d}$	arcsec	36.0 arcsec	$36.3^{+1.0}_{-0.4}$
(8)	$\epsilon_{\rm disk}$	-	0.71	-
(9)	$f_{\rm DM}$	-	$0.55^{+0.05}_{-0.05}$	-

Table 2.6: Structural parameters of NGC 1380 computed from MGE model (Table 2.2) and stellar dynamical modeling results (Table 2.5) in this study and those derived by the traditional bulge-disk decomposition (Bedregal et al., 2006). Row (1): Bulge-to-total fraction in luminosity at I band in this study and K band in Bedregal et al. (2006); Row (2): Bulge-to-total fraction in mass; Row (3): Bulge mass; Row (4): Bulge half light radius ; Row (5): Intrinsic ellipticity of bulge component; Row (6): Disk mass; Row (7): Disk scale length $R_{\rm d}$; Row (8) Intrinsic ellipticity of disk component; (9) Dark matter fraction at the disk scale length $R_{\rm d}$. Values without confidence intervals are derived by the best-fit MGE model (which describe the intrinsic 3D luminosity distribution given inclination). Values with 68% confidence intervals are derived by our final posterior distribution obtained by $\rm JAM_{sph}$ modeling. See text for our definition and derivation of Disk scale length $R_{\rm d}$.

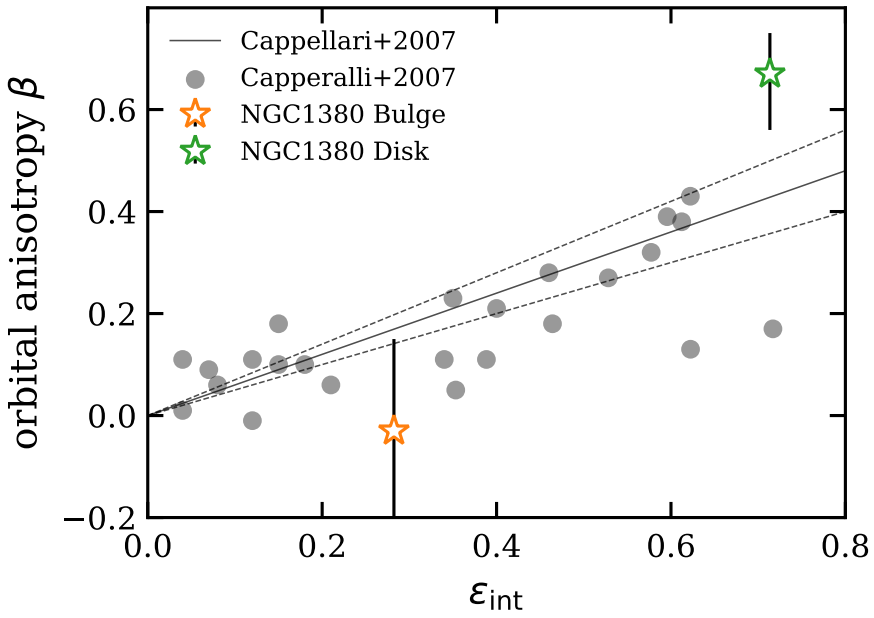

Figure 2.23: Orbital anisotropy β as a function of intrinsic ellipticity $\epsilon_{\rm intr}$ for the sample of early type galaxies measured by Cappellari et al. (2007) (Black circles) and for bulge and disk components measured in this study (shown with orange and green stars respectively). Black line shows the best fitting linear relation for early type galaxies obtained in Cappellari et al. (2007), $\beta = (0.6 \pm 0.1\epsilon_{\rm intr})$

2.5.2 Anisotropy variation in NGC 1380

Figure 2.24 shows the best fit shape of the velocity ellipsoid in the meridional plane of NGC 1380 in JAM$_{\rm sph}$. With the assumption of the velocity ellipsoid being spherically aligned and only two free anisotropy parameters, $\beta_{\rm bulge}$ and $\beta_{\rm disk}$, our model reproduces the realistic velocity ellipsoid in the meridional plane: (1) The velocity ellipse is spherically aligned and nearly isotropic anisotropy in the bulge dominated region (Cappellari, 2020); (2) The velocity ellipse is nearly cylindrically aligned and radially elongated near the equatorial plane, where the density of the disk is maximum (Cappellari, 2008); (3) The velocity ellipse is spherically aligned and radially elongated above the disk

plane (Hagen et al., 2019; Everall et al., 2019) and stellar halo region (Wegg et al., 2019).

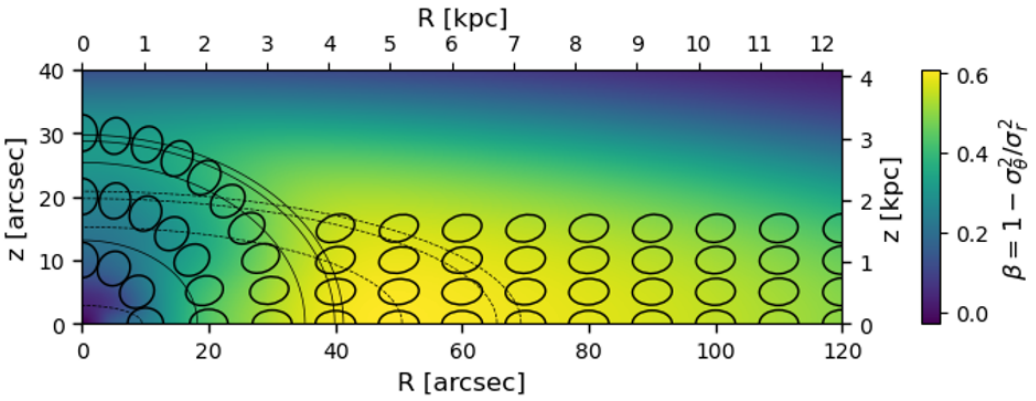

Figure 2.24: The shape of velocity ellipsoid in the meridional plane (R,z) of NGC 1380. The velocity ellipsoid is shown in black ellipse using the best fit parameters $\beta_{\rm bulge}$ and $\beta_{\rm disk}$ of JAM$_{\rm sph}$ results (see Equation 2.9). We show the contours of luminosity distribution of bulge and disk with black sold line and black dashed line, respectively. Note that the direction of the ellipsoids' major axis is towards the center by the assumption of spherical alignment. The color indicates the β value in each position of the galaxy.

2.5.3 Central black hole - galaxy correlation

The central black hole mass of NGC 1380 is, for the first time, directly measured to be $2.52^{+0.32}_{-0.35} \times 10^8 M_\odot$. The central black hole is suggested to correlate with a host galaxy properties (Kormendy & Ho, 2013), such as stellar velocity dispersion and bulge mass. We plot our measurements on the known scaling relations in Figure 2.26 (black hole mass - stellar velocity dispersion) and 2.24 (black hole mass - bulge mass) compiled by Saglia et al. (2016). We measure the effective velocity dispersion σ_e by computing intensity-weighted average of the root mean square velocity $\sqrt{V+\sigma}$ within one half of the half light radius $R_e/2$ as (Kormendy & Ho, 2013; Saglia et al., 2016),

$$\sigma_e = \sum_{R \le R_e/2} \left(w(R) \sqrt{V(R)^2 + \sigma(R)^2} \right) / \sum_{R \le R_e/2} w(R) \tag{2.14}$$

where the weight $w(R)$ is circularized intensity $I_c(R)$. For the half light radius, we adopted the r-band effective radius of $R_e = 56.4$ obtained by unprecedented deep imaging (Iodice et al., 2019). The measured effective velocity dispersion is 188.7 km s^{-1}. The uncertainty estimated following Saglia et al. (2016) (the standard deviation of $\sqrt{V+\sigma}$ divided by the square root of number of data points within $R_e/2$) is unphysically small, 0.0015 km s^{-1}. Therefore, we rather adopted the value 24.3 km s^{-1} derived as the simple standard deviation of $\sqrt{V+\sigma}$ within $R_e/2$, which fully encompass the values when assuming different fractions of R_e used by different authors in the literatures: $R_e/2$ (Kormendy & Ho, 2013) to $R_e/8$ (Ferrarese & Merritt, 2000). Our measurements agree well with the trend seen in other galaxies and the scaling relation derived by Saglia et al. (2016).

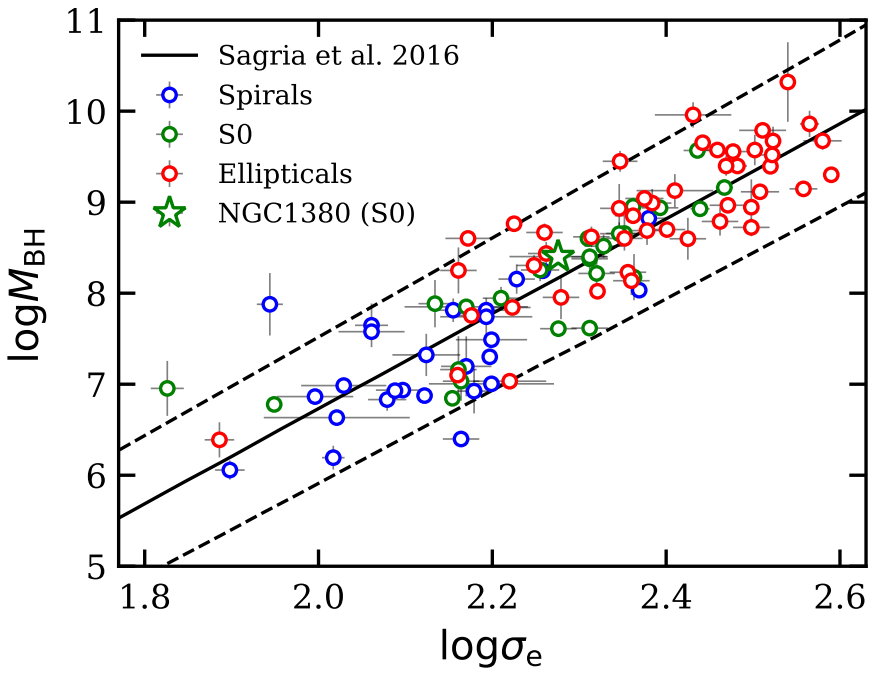

Figure 2.25: Central black hole mass and effective velocity dispersion relation compiled by Saglia et al. (2016). Morphological type of galaxies is indicated by colors: elliptical (red), lenticular (green), and spiral (blue). The scaling relation and its associated uncertainty obtained by Saglia et al. (2016) are plotted with black line and dashed black lines respectively. Our measurement for NGC 1380 is shown with a star.

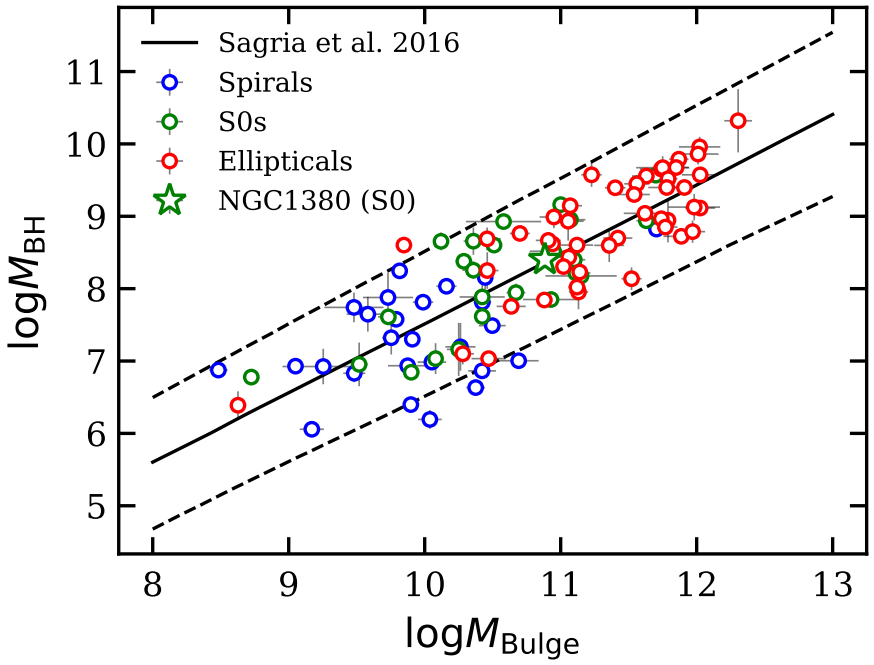

Figure 2.26: Central black hole mass and bulge mass relation compiled by Saglia et al. (2016). The symbols and colors are same as Figure 2.25.

2.5.4 Dark matter fraction in NGC 1380 and the stability of the disk

We consider the dynamical stability of NGC 1380 based on our measured mass distributions of structures: round bulge and halo structure, flat disk structure, and dark matter halo. Efstathiou et al. (1982) found the simple stability criteria of the stellar disk against the bar-like mode instability using N-body simulations

$$V_{\rm max}/(M_{\rm disk}G/R_{\rm d})^{1/2} > 1.1, \tag{2.15}$$

where $V_{\rm max}$ denotes the maximum rotation velocity and $M_{\rm d}$ is disk total mass. Galaxies with only exponential disk (self-gravitating exponential disk) are unstable with

$V_{max}/(M_{disk}G/R_d)^{1/2} = 0.62$. Stable disk structures require round pressure supported structures like bulge (including stellar halo) and dark matter halo. The stability criterion (equation 2.15) can be rewritten regarding the dark matter plus bulge fraction f(DM+Bulge) at $2.2R_d$ as

$$f(DM) = 1 - (V_{disk,max})/(V_{max})^2 > 0.67. \quad (2.16)$$

Figure 2.27 shows the comparison of our measured dark matter fraction f_{DM} and V_{circ} at $2.2R_d$ in NGC 1380 with those measured for spiral galaxies in literatures (Disk mass survey; Martinsson et al. 2013a,b SWELLS survey; Dutton et al. 2013; Barnabè et al. 2012). NGC 1380, like other spiral galaxies, appears to be located in a regime for stellar disk being unstable to bar-like instability mode. However, the prominent bulge structure in NGC 1380 may contribute to the disk stability in addition to the dark matter halo. Once the bulge contribution is taken into account and dark matter plus bulge fraction $f_{DM+bulge} = 0.85^{+0.02}_{-0.02}$ is used instead of f_{DM} as a stability measure in Figure 2.28, the disk of NGC 1380 locates in a stable region for stellar disk, which can explain the absence of significant spiral and bar structures in NGC 1380.

NGC 1380 seems to have a higher dark matter fraction at the given disk radius than other spiral galaxies and depart from the trend, f_{DM} decreases with a circular velocity of the galaxy suggested by Courteau & Dutton (2015) for spiral galaxies. Further studies with a larger sample are needed to clarify whether this indicates the intrinsic difference between the S0 galaxies (including NGC 1380) and late-type spiral galaxies, or the specific galaxy environment of NGC 1380, a central region of Fornax cluster, allows the dark matter accumulation proceed efficiently.

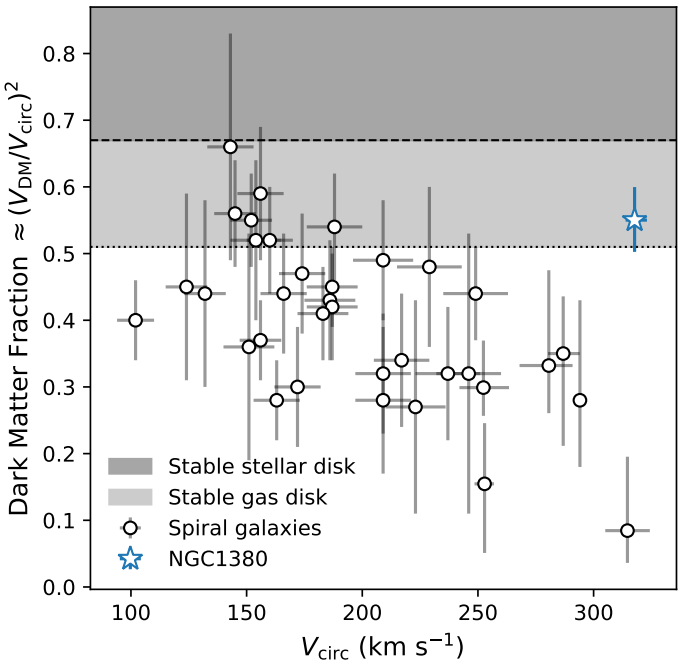

Figure 2.27: The dark matter fraction and total circular velocity $V_{\rm circ}$ for a sample of late-type galaxies (Martinsson et al., 2013a; Dutton et al., 2013; Barnabè et al., 2012) and NGC 1380. Our measurement is highlighted with a blue star. Gray region indicates the stability criteria for stellar disk (above $f_{DM} \approx 0.67$ Efstathiou et al. 1982) and gas disk (both light and dark glay; above $f_{DM} \approx 0.51$ Courteau & Dutton 2015).

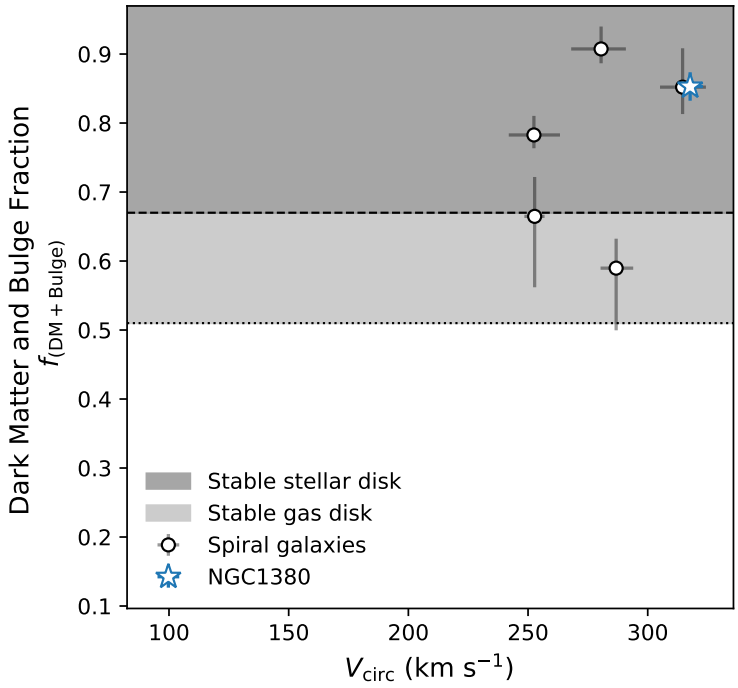

Figure 2.28: The dark matter plus bulge fraction at $2.2R_d$ and total circular velocity V_{circ} for 5 bulge-dominated late-type galaxies (Dutton et al., 2013) out of galaxies plotted in Figure 2.27 and NGC 1380. Our measurement is highlighted with a blue star. The symbols and colors are same as Figure 2.27.

2.6 Concluding Remarks of This Chapter

We analyzed various observational data for NGC 1380 (i.e., large-field-of-view stellar photometric image by HST, and stellar kinematics by VLT/MUSE and molecular gas CO(2-1) kinematics by ALMA) to infer the internal structures and their mass distributions of NGC 1380.

- We non-parametrically decomposed the I band HST photometric image into a round and flat structures using MGE. The result is concordant with the stellar kinematic data (the ratio of the rotation velocity to random velocity dispersion, the

variation of velocity anisotropy), suggesting (1) a dispersion dominated spherical structure like a bulge within ∼ 20 arcsec (2) a rotation dominated flat structure like a disk from ∼ 20 to ∼ 100 arcsec and (3) a spherical structure like a stellar halo from ∼ 100 arcsec.

- In addition to the visible structures, the velocity rises towards the center in the molecular gas kinematics, which suggests the presence of a central black hole. Root mean square velocity $\sqrt{V^2 + \sigma^2}$ of stellar kinematics remains constant up to the outer part of the galaxy, suggesting that the dark matter dominates in the outer part of the galaxy.

- The black hole mass of $2.52^{+0.35}_{-0.32} \times 10^8 M_\odot$ is estimated by dynamical modeling of ALMA CO(2-1) molecular gas, which is robust to the assumption of the spatially variable mass to light ratio. The modeling also allows us to measure the extended stellar mass distribution separately from the BH mass. The estimated $M_{\rm BH}$ is consistent with scaling relations such as $M_{\rm BH} - \sigma_{\rm e}$ and $M_{\rm BH} - M_{\rm bulge}$.

- We model the stellar kinematics using the mass distribution derived from ALMA CO(2-1) molecular gas as a prior and assigning different velocity anisotropies $\beta_{\rm bulge}$ and $\beta_{\rm disk}$ to spherical and flat stellar components. Spherically aligned velocity ellipsoid $\mathrm{JAM_{sph}}$ is preferred in terms of the resulted likelihood, consistency of the central mass distribution, and physically motivated anisotropy values.

- The derived velocity anisotropy of β and intrinsic ellipticity $\epsilon_{\rm intr}$ of bulge and disk is consistent with the observationally suggested correlation by Cappellari et al. (2007) that the flatter structure has larger anisotropy.

- The dark matter fraction at 2.2 disk scale radius $R_{\rm d}$ is estimated to be $0.55^{+0.05}_{-0.05}$,

making NGC 1380 in the regime where the stellar disk is unstable to the bar mode instability (Efstathiou et al., 1982). However, if considering that the bulge component also contributes to the stability of the disk, the fraction of bulge plus dark matter halo is $0.85^{+0.02}_{-0.02}$, explaining the absence of significant spiral and bar structures in the lenticular galaxy NGC 1380.

3

Galactic Structures in the Early Universe

3.1 Introduction of This Chapter and Target BRI 1335-0417

Most spiral galaxies have common distinct structures: a bulge; a flat, extended rotating disk; and prominent spiral arms that stretch from the center. As observationally established, the cosmic star formation in the universe has undergone a particular process

of evolution; the star formation rate rises steeply after the Big Bang, reaches a peak at redshift z between 1.5 and 3, and declines steadily since then (Madau & Dickinson, 2014). Optical observations provide evidence that the prominent bulge structure is already formed in some massive galaxies at z of 0.5 to 2.5 (Tacchella et al., 2015; Lang et al., 2014). Spiral structure has been reported in three galaxies at redshift of $z = 2.18$ [Q2343-BX442: (Law et al., 2012)], $z = 2.01$ [HDFX 28: (Dawson et al., 2003)] and $z = 2.54$ [A1689B11: (Yuan et al., 2017)]. The high-resolution observation by the Atacama Large Millimeter/submillimeter Array (ALMA) have begun to reveal the potential substructures, including spiral structure in two submillimeter galaxies at redshift of $z = 2.32$ (ALESS 112.1) and $z = 2.67$ (ALESS 15.1) (Hodge et al., 2019) and the existence of the dynamically cold disk in galaxies at redshift $z \sim 4$ (Rizzo et al., 2020; Neeleman et al., 2020; Tadaki et al., 2018; Lelli et al., 2021) and a compact structure like a bulge at redshift z of 4 to 5 (Rizzo et al., 2020; Lelli et al., 2021). It is currently unclear whether the later appearance of spiral structure is due to different formation times or observational limitations.

BRI 1335-0417 is a quasar host galaxy at redshift $z = 4.4074 \pm 0.0015$ (Guilloteau et al., 1997), 1.4 Gyr from the Big Bang, and is classified as a Hyper Luminous InfraRed galaxy (HyLIRG) with a luminosity of $3.1 \times 10^{13} L_\odot$ ($L_\odot$ is the luminosity of the Sun) at far-infrared wavelengths (Carilli et al., 2002) and is one of the most intensely star-forming galaxies known at $z > 4$ with a star formation rate of $5 \pm 1 \times 10^3 M_\odot \mathrm{yr}^{-1}$ ($M_\odot$ is the mass of the Sun) estimated from the modeling of spectral energy distribution (Wagg et al., 2014). Physical properties of BRI 1335-0417 derived so far are summarized in Table 3.1. [CII] line emission from this galaxy was detected in previous observations at lower spatial resolution, which was insufficient to determine the gas distribution and kinematics (Wagg et al., 2010).

#	Properties	Values
(1)	R.A.[$^{\rm h}$ $^{\rm m}$ $^{\rm s}$]	13 38 03.4145
(2)	Dec.[$^\circ$ $'$ $''$]	-04 32 34.9769
(3)	$L'_{\rm CO(2\rightarrow1)}$($10^{11}$ K km s^{-1}pc^{-2})	1.09 ± 0.08
(4)	$L_{\rm [CII]}$(10^9 $L_\odot$)	16.4 ± 2.6
(5)	$M_{\rm H_2\,(\alpha=0.8)}$($10^{10}M_\odot$)	1.03 ± 0.07
(6)	$M_{\rm H_2\,(Z'=1)}$($10^{10}M_\odot$)	5.1 ± 0.4
(7)	$M_{\rm H_2\,(Z'=0.02)}$($10^{11}M_\odot$)	6.5 ± 0.5
(8)	SFR(10^3 $M_\odot$ yr^{-1})	5± 1
(9)	log$M_{\rm BH}$	9.77

Table 3.1: Properties of BRI1335-0417: (1) and (2) Right ascension and declination (J2000) from Gaia data release 2 catalogue (Gaia Collaboration, 2018), (3) CO(J=2→1) luminosity $L'_{\rm CO(2\rightarrow1)}$ (Jones et al., 2016) (4) [CII] luminosity $L_{\rm [CII]}$ (Wagg et al., 2010) (5), (6) and (7) Respective molecular gas masses $M_{\rm H_2}$ estimated using three different conversion factors from $L'_{\rm CO(2\rightarrow1)}$ to M_{H_2} (Jones et al., 2016), that are $\alpha_{\rm CO} = M_{\rm H_2}/L'_{\rm CO(1\rightarrow0)}$ = 0.8 M$_\odot$ K^{-1} km^{-1} s pc^{-1}, a standard value for low z star-bursting galaxies (SMGs; Bolatto et al. 2013), and the valuses $\alpha_{\rm CO}$ in the case of solar metallicity $Z = Z_\odot$ and unphysically low metallicity $Z = 0.02$ $Z_\odot$ considering the dependency of metal abundances (Narayanan et al., 2012). For all cases, Jones et al. (2016) used $L'_{\rm CO(2\rightarrow1)}/L'_{\rm CO(1\rightarrow0)}$ = 0.85 which is a standard value for SMGs. (8) Star formation rate (SFR) estimated by modeling spectral energy distribution (Wagg et al., 2014) (9) BH mass estimated using broad CIV line width (Shields et al., 2006).

3.2 ALMA Observation Data

3.2.1 Band 7 Spectroscopic Images - [CII] Gas and Dust Continuum

BRI 1335-0417 was observed in [CII] line emission (rest-frame frequency of 1900.5369 GHz) using ALMA with the Band 7 receiver for the rest-frame frequency being redshifted to around 351 GHz in the observed frame. At the redshift for BRI 1335-0417 of z = 4.4074 (Guilloteau et al., 1997), the [CII] line of 1900.5369 GHz is shifted to 351.470 GHz and can be observed with ALMA Band 7 (275 – 373 GHz) that has two single sideband (2SB) receiver systems (Iguchi, 2005), providing upper sideband (USB) and lower sideband (LSB) simultaneously with the intermediate frequency (IF) bandwidth of 4-8 GHz. We retrieved archival ALMA observations obtained on 2018 January 21 in the observing frequency range of 337.434 GHz -341.433 GHz (LSB) and 349.705 GHz -353.271 GHz (USB), so the USB contains the redshifted [CII] line emission. The LSB consists of two spectral windows, each of which has 128 frequency channels with a width of 15.625 MHz, while USB consists of two spectral windows, each of which has 1920 frequency channels with a width of 977 kHz. The total bandwidths of LSB and USB were 4 GHz and 3.75 GHz, respectively. The observation was executed in the C43-5 array configuration with baseline lengths of 15 m to 1398 m. The 5th percentile shortest baseline of the configuration was 70 m, providing the maximum recoverable scale of 2.47 arcsecond at 351.47 GHz [(Remijan et al., 2019) their equation 7.7]. Total observing time was 2.0 h, including an on-source time of 1.0 h and the other 1.0 h for calibration sources and overhead. QSO B1334-127 (VCS1 J1337-1257) was utilized as a flux and bandpass calibrator and NGC 5232 (VCS1 J1336-0829) as a phase calibrator.

We performed data reduction using version 5.1.1 of the Common Astronomy Software Applications (CASA; McMullin et al. 2007) pipeline. We first imaged the dust

continuum emission shown in Fig. 3.1 using the line-free channels (with a 4.75 GHz total bandwidth over both sidebands at a central frequency of 345 GHz in the observed frame corresponding to 1863 GHz in the rest frame) using the task tclean in CASA. We identified the line-free channels using the hif_findcont task in CASA and removed channels that show a dip feature around ~ 352.3 GHz due to atmospheric absorption. The visibility data were weighted by the Briggs scheme with a robust parameter of 0.0, which provides a trade-off between resolution and sensitivity, resulting in a synthesized beam with FWHM 0.17" × 0.14" (~ 1.16 kpc × 0.95 kpc in physical scale) at a position angle of 86 deg and a root mean square noise of 0.036 mJy beam^{-1}. Secondly, we imaged the [CII] line emission shown in Fig. 3.1 (A and B). We measured the flux density of the dust continuum emission by fitting a linear function to the line-free channels and subtracted its emission components from the visibility data using the task uvcontsub in CASA. After continuum subtraction, we imaged two spectral windows of the USB to produce a data cube with the three dimensions of right ascension, declination, and velocity using the task tclean in CASA. The velocity channel resolution was 20 km s^{-1} (=23.4 MHz) after binning by 24 frequency channels of 977 kHz to improve the signal-to-noise ratio. The visibility data were weighted by the Briggs scheme with a robust parameter of 0.5, resulting in a synthesized beam with FWHM 0.20" × 0.16" (1.33 kpc × 1.11 kpc in a physical scale) at a position angle of 80 deg. The root mean square noise of each velocity channel with a width of 20 km s^{-1} is about 0.35 mJy beam^{-1}. The clean threshold was set to 1.5 times the rms noise for the dust continuum image and 1.0 times rms noise for the [CII] line image to maximize the flux in the cleaned model. The clean mask was drawn closely around the areas of source emission. For both dust continuum and [CII] line images, the cellsize was chosen to be roughly one third of the minor synthesized beam width. Primary beam correction was performed, smaller

than 1 % at the edge of the images.

Figures 3.1 (A and B) show [CII] images of the integrated flux and line-of-sight velocity respectively. Figures 3.1 B were made by the masked moment method (Dame, 2011). The observed data cube was smoothed by convolving with a uniform filter spatially (1.5 times the beam size) and spectrally (4 times the channel width), then the mask area was determined by the intensity threshold (7.5 times the root mean square noise in the smoothed cube) and applied to the original observed cube. Finally, these velocity images (Moment 1) were created from the masked cube using plotting code in the KINMS package (Davis et al., 2013a). The filter size and threshold of the mask were selected, so the mask covered the [CII] line emission area.Figure 3.1D shows a composite image of the gas velocities, produced from [CII] velocity channel maps (Fig. 3.2) that show the [CII] line intensity images at each velocity.

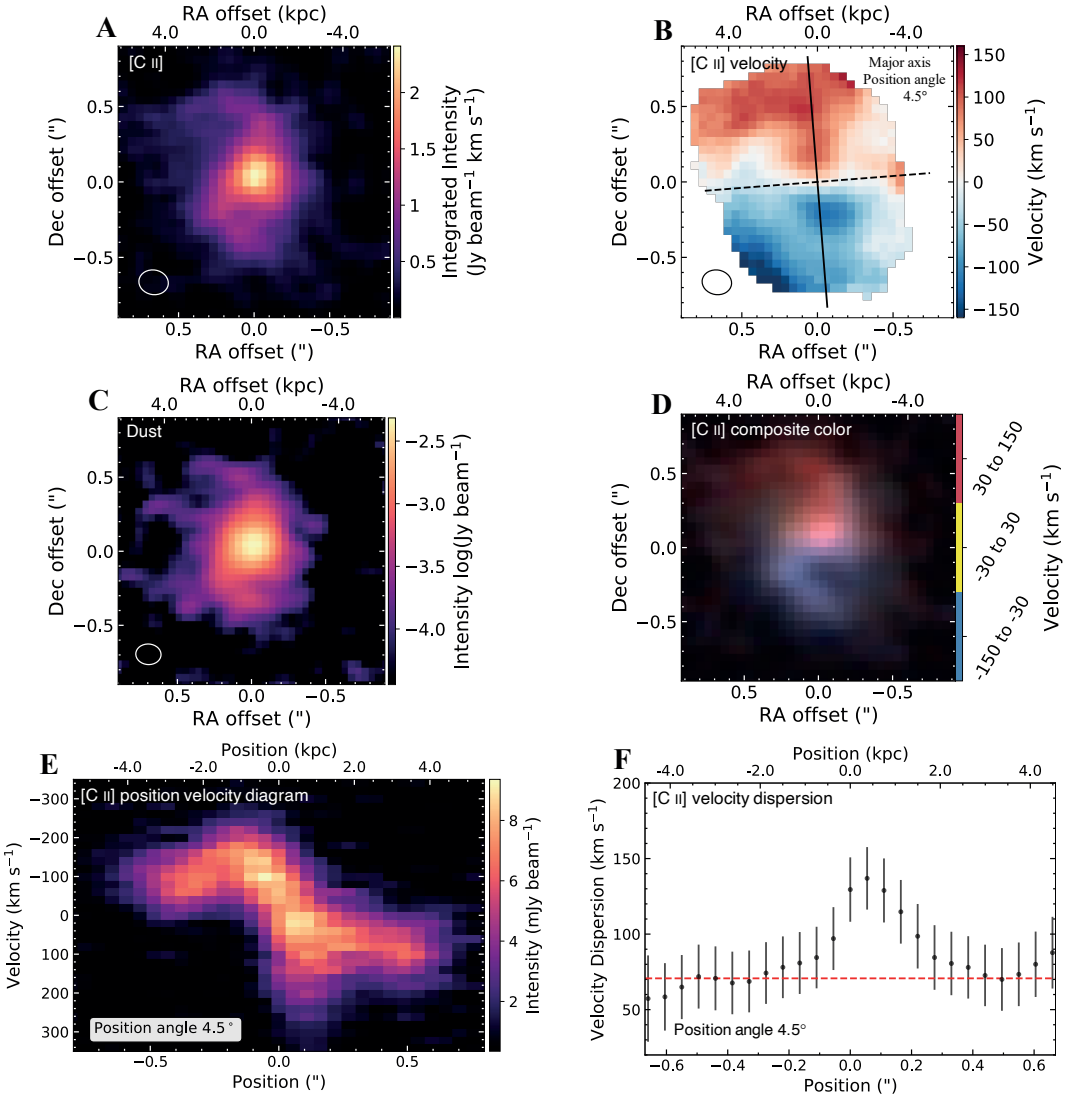

Figure 3.1: Morphology and kinematics of [CII] line and dust continuum emission in BRI 1335-0417. (A) and (B) the ALMA [CII] line maps of intensity (moment 0) and intensity-weighted velocity (moment 1). The kinematic major and minor axes are shown in panel B by black solid and dotted lines, respectively. (C) the ALMA dust continuum map at a rest-frame frequency of 1863 GHz. (D) a composite color image, showing in red the redshifted gas emission with velocity of 30 to 150 km s^{-1}, in yellow gas at the systemic velocity of -30 to 30 km s^{-1}, and in blue the blueshifted gas with velocity of -150 to -30 km s^{-1}. The FWHM of the synthesized beam is 0.20" × 0.16" in (A), (B) and (D), and 0.17" × 0.14" in (C), which are shown by an ellipse in the bottom left corners. In each figure panel, the right ascension (RA) and declination (Dec) offsets are given relative to the position (J2000) $13^{h}38^{m}03^{s}.416$, -4°32'35".02. (E) PVD of the observed [CII] line emission, extracted along the major kinematic axis shown in panel B, which has a position angle of 4.5° (Table S1). Data were averaged over one beam width (three pixels). (F) the velocity dispersion measured from the line profile at each position of PVD. The error bars correspond to the sum in quadrature of the profile fitting uncertainty (95% confidence level) and the velocity channel width. The red dashed line shows the estimated intrinsic velocity dispersion of 71^{+14}_{-11} km s^{-1}. Positive position in panels (E) and (F) is the direction toward the north along the kinematic major axis in (B).

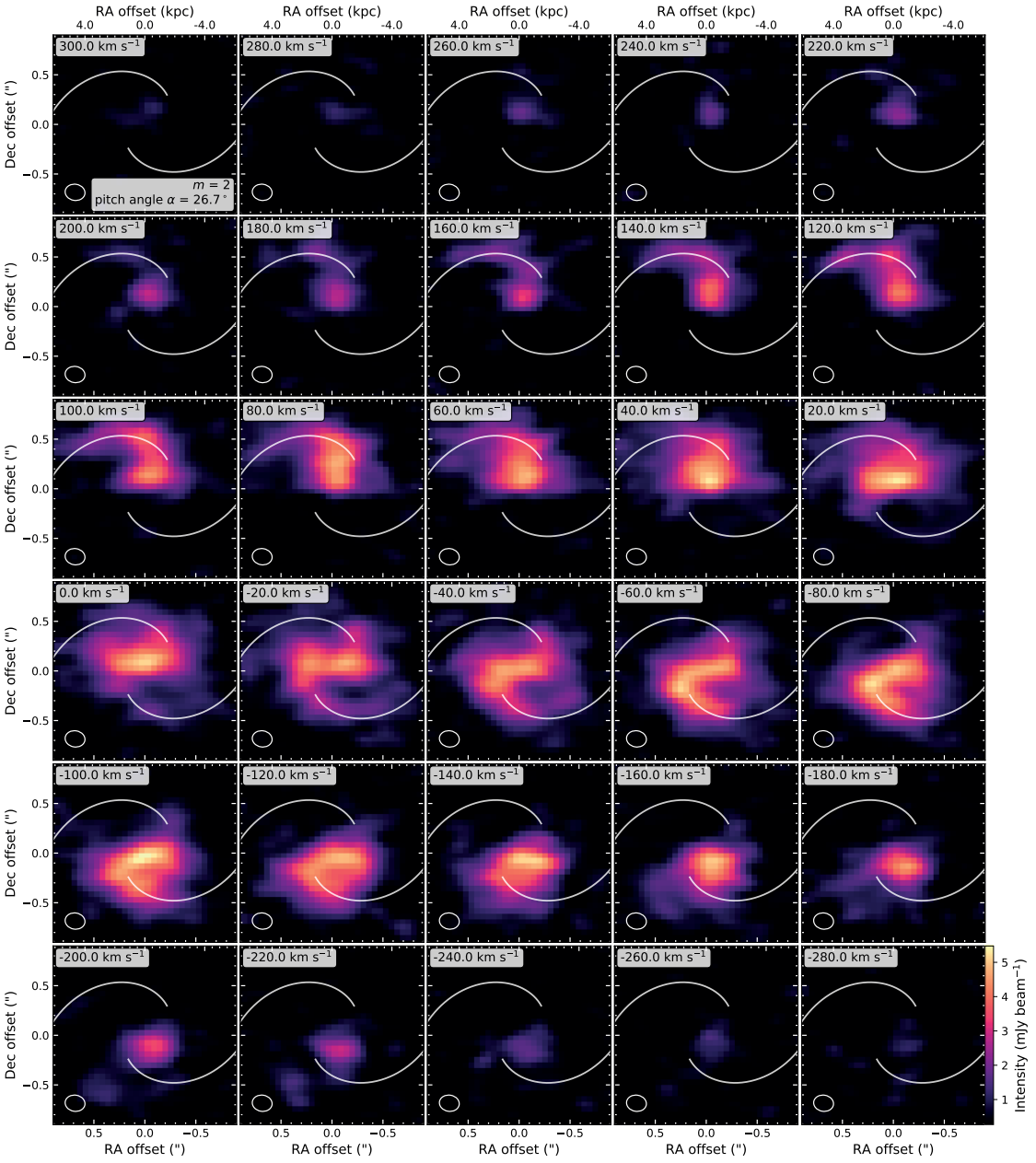

Figure 3.2: Velocity channel maps of the [CII] line emission, showing the spiral structure. Each panel shows an image at each velocity of the [CII] line emission, labeled in the top left. Overline with white lines is the best-fitting two-armed logarithmic spiral model, which has a pitch angle $\alpha = 26.7°$ (14). The images have been de-projected to be viewed as face-on using a position angle of 4.5° and inclination of 37.8° (Table S1). The white ellipse shows the FWHM of the synthesized beam in the left bottom of each panel.

3.3 Results: Identifying Galactic Structures

3.3.1 Identifying Disk and Bulge

Morphology and Kinematics of [CII] Gas and Dust Continuum Distribution

Images of the [CII] line and Dust continuum emissions show a central compact structure and an extended structure like a disk. The composite color image shows a spiral morphology with clear northern and southern arms extended from the radius of 2 to 5 kpc. In addition to the composite color image, two spiral arms are much more clearly seen on the [CII] velocity channel images (Fig.3.2). The CO(2→1) line images were obtained by the Karl G. Jansky Very Large Array (JVLA), which showed different spatial distributions of CO(2→1) depending on the antenna configuration used for the observations. The images obtained with BnA and B configuration showed a structure with a bright central component and a weaker northern component (Jones et al., 2016), while with B and C antenna configuration showed a complex structure with multiple components (Riechers et al., 2008). However, these multiple CO(2→1) components correspond to the northern spiral arm, southern spiral arm, and central disk of [CII] images in position and velocity, indicating that CO(2→1) line has similar dynamics with [CII] line. This can be explained by the difference of the emitting region: [CII] line emission arises from multiple phases of the interstellar medium, including ionized gas, atomic gas, and molecular gas, while CO (2-1) line emission traces dense molecular gas (Pineda et al., 2013), and also by the difference of the observations: ALMA [CII] data enable us to make images of compact and diffuse extended structures with high fidelity thanks to broad uv coverage, maintaining a sensitivity with reasonable spatial and spectral resolutions.

We can see a central, steep rise of [CII] line velocity reaching about 240-260 km s^{-1}, which is a signature of the centrally concentrated mass distribution, and a constant velocity of 70-110 km s^{-1} in the outer parts, in the Position-Velocity Diagram (hereafter PVD; Fig. 3.1E) along the kinematic major axis. A slowly rising or constant velocity curve has been detected in other high redshift galaxies (Rizzo et al., 2020; Neeleman et al., 2020; Tadaki et al., 2018). Such a velocity curve has been observed in nearby spiral galaxies where the galaxy's gravitational potential is determined by a combination of some galactic structures (Sofue et al., 2003). This PVD of observed [CII] line emission also indicates the presence of a central compact structure like a bulge and an extended disk. Looking at the more detailed features of PVD, the central rise of the velocity in the northern side appears steeper than the southern side. At larger radii, the subsequent decrease of the velocity appears steep in the southern side while shallow in the northern side. These may be due to streaming motion along spiral arms, warping of the disk, recent gas accretion (Lelli et al., 2021) and/or the central lopsided gas distribution. These slightly disturbed features are rather common in nearby galaxies and also have been revealed in high-redshift galaxies at $z \sim 4$ with recent high-resolution observations (Neeleman et al., 2020; Lelli et al., 2021). Figure 3.1F shows the velocity dispersions extracted at each position of PVD in Fig. 3.1E. The velocity dispersions of $\sim$ 70 km s^{-1} seem to be constant in the outer parts, but the velocity dispersion increases up to $\sim$ 140 km s^{-1} in the center. This increase in the center is known to be due to the beam smearing effect (Burkert et al., 2016). Since the spatial resolution of the beam is not enough to capture the intrinsic velocity gradient, the velocity gradient decreases as the velocity is averaged over the beam width, and the observed velocity dispersion increases. Thus, the intrinsic velocity dispersion σ of 71 km s^{-1} (see red dashed line in Fig. 3.1F) is estimated by a method proposed by Green et al. (2010) that extracts the velocity

dispersion at the outer region of the disk where the beam smearing is less severe and corrects the beam smearing effect.

Quantifying the [CII] Gas and Dust Continuum Distribution

Both the Dust continuum and [CII] line intensity distributions of BRI 1335-0417 include complex structures which may indicate a disk and spiral arms; accordingly, the position angle of the disk was estimated by using PAFIT Package (Krajnović et al., 2006) from the [CII] line velocity image (Figure 3.1 B), which shows the regular rotation and kinematic position angle. The central 0.5" region in [CII] line velocity image was utilized for measuring position angle, as this region features a sufficient signal-to-noise ratio. The estimated position angle is 4.5 ± 3.7 (95 % confidence interval). We also derived the position angle of the disk from the gas dynamical modeling (see below), finding $7.6^{+7.3}_{-7.1}$ ° at 95 % confidence level. To estimate the axis ratio of the disk with the estimated position angle, we fitted 2-dimensional (2D) Sérsic functions to the dust continuum image (see Fig 3.8C) and the [CII] line intensity image (Fig. 3.1A), using GALFIT code (Peng et al., 2010). While fitting these images, the synthesized beam was taken into account. From the estimated axis ratio (q) of the dust continuum image, the inclination of the disk $i = 37.8^{+2.4}_{-3.3}$ ° was calculated with equation $q = \cos(i)$ and the confidence interval was estimated from the uncertainty of the measured position angle. This estimated inclination was used as a prior in our MCMC sampling (see below), where the gas dynamical modeling finds $37.3^{+3.0}_{-3.1}$ ° at 95 % confidence level. As GALFIT outputs, the measured Sérsic index is $n = 0.87 \pm 0.02$ (close to exponential n=1) from the [CII] line intensity distribution, while it is $n = 2.48 \pm 0.05$ from the distribution of the dust continuum emission. These indicate that the [CII] line distribution has a shallow and near exponential profile like a typical disk (Driver et al., 2006), while the dust

continuum distribution has a centrally concentrated profile with a high Sérsic index ($n > 2$) compatible with that of a typical galaxy with a bulge (Driver et al., 2006). We therefore fitted a 2D exponential function to the [CII] line intensity image, resulting in a disk-scale radius $R_d = 1.83 \pm 0.04$ kpc. The physical parameters derived in this section using PAFIT Package and GALFIT are listed in Table 4. Figure 3.3 shows the azimuthally-averaged intensity profile of the [CII] line image and continuum image with the best fit exponential profile and Sérsic profile, respectively.

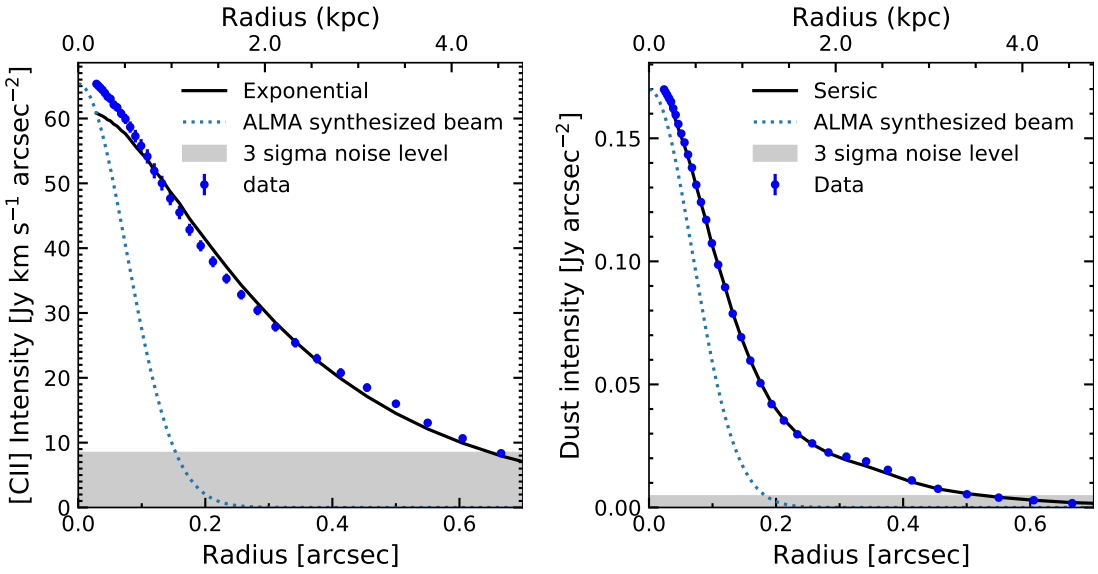

Figure 3.3: Left figure shows the observed [CII] line intensity profile (blue point) and the best fit exponential intensity profile (black line). Right figure shows the intensity profile of the observed dust continuum (blue point) and the best fit Sérsic profile ($n = 2.48$, black line). The blue dotted line shows Gaussian function which approximates the synthesized beam of ALMA, where its FWHM is a geometric mean of major- and minor-axis of that of the synthesized beam. These intensity profiles are derived by using Photutils code (Bradley et al., 2019) as follows. We first derive the ellipses by fitting them to the isophotes of intensity images (Figure 3.1A for [CII] line and Figure 3.1C for dust continuum), where four parameters of each ellipse (2-dimensional centre position, a position angle and an ellipticity) are left free. All of these azimuthally-averaged intensity profiles are derived by averaging along each ellipse.

Disk position angle Γ(°)	4.5±3.7
Disk inclination i(°)	$47.8^{+2.4}_{-3.3}$
Disk scale radius $R_{\rm d}$(kpc)	1.83± 0.04
Dust continuum effective radius $R_{\rm e,dust}$(kpc)	1.40± 0.02

Table 3.2: Physical parameter derived by PAFIT Package and GALFIT. The position angle of the disk was estimated from the [CII] line kinematics using the PAFIT package. The inclination of the disk, i was estimated from the axis ratio measured by fitting the Sérsic profile to the dust continuum image using the GALFIT code. The reduced chi-square χ^2_ν of the fitting is 1.592, where the degree of freedom is 4090. Disk scale radius Rd was estimated by fitting exponential profile to the [CII] line image using the GALFIT code. The reduced chi-square χ^2_ν is 0.956, where the degree of freedom is 4091.

Quantifying the Rotation Kinematics of [CII] Gas

We estimate the inclination-corrected rotational velocity v_{rot} is 179^{+25}_{-18} km s^{-1} at radius of 0.3", calculated using the flat part of the PVD (Fig. 3.1E). The ratio of v_{rot} to the intrinsic velocity dispersion σ quantifies the rotational support of the disk (Burkert et al., 2016). Our estimated ratio v_{rot}/σ of $2.5^{+0.6}_{-0.4}$ indicates that the [CII] gas disk of this galaxy is rotation-dominated. Similar values have been found for other galaxies observed at $z \sim 4$ (Neeleman et al., 2020; Tadaki et al., 2018). Higher ratios have also been reported at redshift of 4 to 5 (Rizzo et al., 2020; Lelli et al., 2021). Additional evidence of rotating disk is symmetric velocity field across the kinematic minor axis, seen in this object (Fig. 3.1B).

Gas Dynamical Modeling

We used the KINMS code (Davis et al., 2013a) to produce a gas dynamical model cube which has the same beam size and velocity resolution as those in the observed cube (i.e., beam smearing effect was taken into account for the model cube). It requires a set of gas particles which approximates the distribution of gas intensity in physical

space (right ascension, declination, and distance along the line of sight), and then the line-of-sight velocity of each particle is calculated by taking a circular velocity of the galaxy as an input. The SKYSAMPLER code (Smith et al., 2019) was used to generate gas particles that reproduce the [CII] line intensity profile of BRI 1335-0417 by using the de-convolved CLEAN components that were provided by a task of tclean in CASA. Then, it transformed the distribution of gas particles from the sky plane into the physical space using the inclination and position angle of the galactic disk.

Structures of the Galaxy

In general, the structure of disk galaxies consists of a central black hole, a centrally concentrated bulge, an extended disk and a dark matter halo (Kent, 1986; Sofue et al., 2009; Genzel et al., 2017). The circular velocity $v_{\rm circ}(r)$ of the galaxy can be expressed by

$$v^2_{\rm circ}(r) = v^2_{\rm BH}(r) + v^2_{\rm bulge}(r) + v^2_{\rm disk}(r) + v^2_{\rm DM}(r), \tag{3.1}$$

where r denotes the radial distance from the galaxy center, and $v_{\rm BH}(r)$, $v_{\rm bulge}(r)$, $v_{\rm disk}(r)$ and $v_{\rm DM}(r)$ are the circular velocity of a test particle at r due to the gravitational potential of the central black hole, bulge, disk, and dark matter, respectively. The sphere of influence of the black hole $R_{\rm SOI} = GM_{BH}/^2_*$= 0.02" where the G is the gravitational constant, MBH is the mass of the black hole and σ_* is the stellar velocity dispersion, was calculated for a mass of $6 \times 10^9 M_\odot$, which was estimated using the virial theorem in a previous study (Shields et al., 2006), assuming the local relationship between black hole mass and stellar velocity dispersion (Kormendy & Ho, 2013). Because estimated RSOI is much smaller than our spatial resolution, we cannot measure the circular velocity of black hole $v_{\rm BH}(r)$ and bulge $v_{\rm bulge}(r)$ separately. We thus included the black hole mass

in the bulge. In this case, $v_{\rm bulge}(r)$ is equal to $v_{\rm BH}(r)$ in the limit that the size of the bulge goes to 0, allowing a possibility of a black hole without a bulge. The mass contribution of dark matter is typically smaller than that of the baryonic structure such as the bulge and disk within the radius of < 10 kpc, which are suggested by the recent observation for high redshift galaxy (Genzel et al., 2017; Förster Schreiber et al., 2009; Wuyts et al., 2016). In this object, the [CII] line emission is detected only up to 5 kpc, which is not sufficient to measure the mass distribution of the dark matter using the kinematics. We therefore excluded the dark matter mass distribution from our dynamical model. A circular velocity $v_{\rm circ}(r)$ of the galaxy is then approximated by

$$v^2_{\rm circ}(r) = v^2_{\rm bulge}(r) + v^2_{\rm disk}(r). \tag{3.2}$$

Bulge Model

In the PVD shown in Fig. 3.1E, there is a steep rise of [CII] line velocity reaching about 240 to 260 km s^{-1} in the galactic center, indicating a centrally concentrated mass distribution such as a bulge. Observations of nearby galaxies (Gadotti, 2009; Lange et al., 2016) and distant galaxies ($2 < z < 3$) (Lang et al., 2014; Bruce et al., 2014) indicate that the observed surface brightness distributions of a bulge can be approximated by de Vaucouleurs profile (de Vaucouleurs, 1948). Assuming the bulge has the same mass profile as its brightness profile, we can express the surface mass density distribution using the de Vaucouleurs profile:

$$\Sigma_{\rm bulge}(R) = \Sigma_e \exp\left\{-\kappa[(R/R_e)^{1/4} - 1]\right\} \tag{3.3}$$

where $\kappa \sim 7.6695$ (Graham & Driver, 2005), R is the projected radius on the plane of the sky and Σ_e is the surface mass density at the effective radius R_e in which the enclosed mass becomes half of the total mass of the bulge M_{bulge}. The total mass of the bulge is then given by $M_{bulge} \sim 22.665 R_e^2 \Sigma_e$ (Sofue et al., 2009). In the case of a spherical bulge, the circular velocity of the bulge $v_{\rm bulge}(r)$ at r can be determined by two parameters: the total mass of the bulge M_{bulge} and the effective radius R_e. It follows that (Binney & Tremaine, 2008; Noordermeer, 2008)

$$v^2_{\rm bulge}(r) = -\frac{4G}{r}\int_{l=0}^{r}\left[\int_{R=l}^{\infty}\frac{d\Sigma_{\rm bulge}(R)}{dR}\frac{dR}{\sqrt{R^2-l^2}}l^2\right]dl. \tag{3.4}$$

The circular velocity of the spherical structure differs from that of the non-spherical one. In the case of a non-spherical structure with an axial ratio greater than 0.6, however, the difference between them is less than 8 percent, allowing us to use the spherical assumption for simplicity.

Disk Model

The exponential disk has not only been predicted by the theory of galactic disk formation (Katz & Gunn, 1991) but also revealed by several photometric observations of nearby galaxies (Gadotti, 2009; Driver et al., 2006) and distant galaxies ($z \sim 2-3$) (Wuyts et al., 2016; Lang et al., 2014; Bruce et al., 2014; Genzel et al., 2014). In addition, the exponential profile has been widely used for disk mass distribution in modeling the galactic dynamics, including the Milky Way (Sofue et al., 2009; Genzel et al., 2017; Burkert et al., 2010). A surface mass density distribution of an exponential disk is given by

$$\Sigma_{\rm disk}(R) = \Sigma_0 \exp(-R/R_d), \tag{3.5}$$

where R_d is a disk-scale radius and Σ_0 is the central surface mass density. The circular velocity of the disk can be fully determined by just two parameters: the disk-scale radius Rd and the total mass of the disk $M_{disk} = 2\pi\Sigma_0 R_d^2$. It follows that (Freeman, 1970)

$$v_{\rm disk}^2(r) = 4G\Sigma_0 R_d y^2 [I_0(y)K_0(y) - I_1(y)K_1(y)] \tag{3.6}$$

where $y = r/(2R_d)$. I_0, K_0, I_1 and K_1 are modified Bessel functions. Several studies suggest that the [CII] line is a good tracer of the total gas mass (Zanella et al., 2018; Gullberg et al., 2018). Also, [CII] intensity distribution of this object is well fitted by the exponential profile. In this paper, we therefore used $R_d = 1.83$ kpc measured by the GALFIT code (Table 4).

Rotation Velocity of Pressurized Galactic Disk

The PVD in Fig.3.1E shows that BRI 1335-0417 has velocity dispersions of ~ 70 km s^{-1} in the outer parts. The intrinsic velocity dispersion averaged for galaxies at $z \sim 2.3$ is 50 ~ 70 km s^{-1} but there are a wide range of values up to ~ 80 km s^{-1}, and for galaxies at $z \sim 0.9$ is 25 km s^{-1} (Wisnioski et al., 2015). The pressure in the gas disk is proportional to the square of the velocity dispersions of the gas, which is not negligible for the gas dynamical modeling (61). The pressure gradient causes a radial force that balances part of the gravitational force, resulting in the reduction of the rotational velocity of the gas. Under hydrostatic equilibrium, the rotational velocity $v_{\rm rot}(r)$ for the exponential gas distribution is given by Burkert et al. (2010, 2016)

$$\begin{aligned} v_{\rm rot}^2 &= v_{\rm circ}^2(r) + 2\sigma_v^2 \times \frac{{\rm dln}\Sigma_{\rm gas}}{{\rm dlnr}}(r) \\ &= v_{\rm circ}^2(r) - 2\sigma_v^2 \times \left(\frac{r}{R_d}\right), \end{aligned} \tag{3.7}$$

where v is the intrinsic velocity dispersion of the gas, and $\Sigma_{\rm gas}(r)$ is the surface density distribution of the gas disk, which was assumed to be exponential with the disk-scale radius R_d (Table 4). Because the velocity dispersion is constant over this galaxy except in the central region [Fig. 3.1 (E and F)], we adopted an isotropic and spatially uniform velocity dispersion. This is consistent with previous works (Burkert et al., 2010; Genzel et al., 2017; Lang et al., 2017). Given the high velocity dispersion, we considered the disk thickness of $h \sim (v/v_{\rm rot}(R_d)) \times 1.68R_d$ (Genzel et al., 2017), correcting equation 3.3.1.

MCMC Fitting

For modeling, the best fits and their associated confidence intervals are derived by a Markov Chain Monte Carlo (MCMC) sampling using the emcee code (Foreman-Mackey et al., 2013), which is an implementation of affine invariant MCMC ensemble sampler. We directly compare the observed cube with the model cube, then derive the following eight physical parameters: the position angle and inclination of disk (Γ, i), the masses of the central compact structure like a bulge and the disk ($M_{\rm bulge}, M_{\rm disk}$), the effective radius of the compact structure (R_e) and the offsets between the observed and model cubes in right ascension, declination, and velocity ($\Delta x, \Delta y, \Delta V$). Following the Bayesian framework, the posterior distribution of a set of these physical parameters θ on the data is

$$P(\theta|\text{data}) = P(\theta) \times P(\text{data}|\theta), \tag{3.8}$$

where $P(\theta)$ is the prior distribution of the physical parameters, and $P(\text{data}|\theta)$ is the likelihood that is the probability of obtaining the data on the given parameters θ. Since the inclination of the disk i is estimated with GALFIT code (Table 4) as mentioned above, the prior distribution is Gaussian. We used log uniform prior distribution for

the mass of the bulge $M_{\rm bulge}$ and disk $M_{\rm disk}$ in order to cover the multiple orders of magnitude, while uniform prior distribution for the other 5 parameters. The range is set to values much larger than expected from the data. The likelihood can be written as

$$\begin{aligned} P(\text{data}|\theta) &\propto \exp(-\chi^2(\theta)/2) \\ \chi^2(\theta) &= \Sigma_{i=0}^{N} \left[(\frac{I_{\rm data,i} - I_{\rm model,i}}{\sigma_{\rm rms}})^2 \right], \end{aligned} \tag{3.9}$$

where $I_{\rm data,i}$ and $I_{\rm model,i}(\theta)$ are the intensity of the pixel i in the observed cube and model cube respectively. $\sigma_{\rm rms}$ is the root mean square noise of 0.35 mJy beam^{-1} that was measured using the pixels of only line-free channels in the observed cube under the assumption that it is constant over the cube. In fitting, the velocity range of these cubes is from -390 km s^{-1} to +370 km s^{-1} with the velocity center 0 km s^{-1} matched to the frequency of 351.470 GHz in barycentric frame. In the standard χ^2 statistic, the 68% confidence interval corresponds to $\Delta\chi^2 = \chi^2 - \chi^2_{\rm min} = 1$. A variance of this distribution is 2(N - P) where N is the number of constrains and P is the number of inferred parameters. In our data ($N \sim 4 \times 10^4$ and $P = 8$), it becomes 2N and yields an unrealistically small confidence interval due to the large number of constraints in fitting the observed cube. The method to scale the standard $\Delta\chi^2$ by a factor of $\sqrt{2N}$ was proposed by Van Den Bosch & Van De Ven (2009). The scaled loglikelihood by $1/\sqrt{2N}$, or equivalently the scaled root mean square noise $\sigma_{\rm rms}$ by $(2N)^{1/4}$, was used in the previous works with the Bayesian framework, giving the same effect by scaling $\Delta\chi^2$. The modified likelihood can be written as

$$\begin{aligned} P(\text{data}|\theta) &\propto \exp(-\chi^2(\theta)/2) \\ \chi^2(\theta) &= \Sigma_{i=0}^{N} \left[(\frac{I_{\rm data,i} - I_{\rm model,i}}{\sigma_{\rm rms}})^2 / \sqrt{2N} \right]. \end{aligned} \tag{3.10}$$

For our data, it is confirmed that MCMC sampling of the posterior distribution converges by using this procedure. Also, the correction by the inverse covariance matrix for the pixel to pixel correlations (Davis et al., 2017) in the observed cube is not taken into account in this paper because it is negligible compared to the effect by scaling the loglikelihood.

Results of the Gas Dynamical Modeling

We run the MCMC fitting with 180 walkers and 4000 steps. Since the first 600 steps are not converged to the posterior distribution (a burn-in phase) by MCMC sampling, these first steps are excluded. The outcomes of MCMC sampling are shown in Fig. 3.4, including the one-dimensional histogram of each physical parameter and the covariance maps of the pairs of physical parameters. The best fits (median of the marginalized distribution) and their associated 95 % confidence intervals are summarized in Table S2. Our gas dynamical modeling provides a good agreement between the observed cube and the model cube (see a comparison between the observed and model images in Fig. 3.5, A to F, and the model PVD superimposed on the observed PVD of BRI 1335-0417 in Fig. 3.5 G, where these PVDs are extracted along the kinematic major axis indicated by a solid line in Fig. 3.5, D to F). Figure. 3.5 shows the comparison between the observed velocity dispersion (black points) and model velocity dispersion (gray shade), measured at each position of PVD. The central increase of the observed velocity dispersion is well reproduced by the dynamical model under the assumption of the spatially uniform intrinsic velocity dispersion. In Figure 3.1A and Figure 3.5A, we can see a spiral morphology in the [CII] line intensity image, but in this paper, we simply assume that the mass distribution of a disk is axisymmetric. This does not affect our mass measurement of the central compact structure. The amplitude of the spiral component is relatively

weak and only about 15% of the peak emission at maximum. In addition, the two-armed spiral morphology is extended from the radius of 2kpc to 5kpc, far from the center. Therefore, the contributions of these two arms to the gravitational potential are small in the center of the galaxy. Also, roughly speaking, the two arms are located symmetrically with respect to the galaxy center, making these contributions cancel each other out.

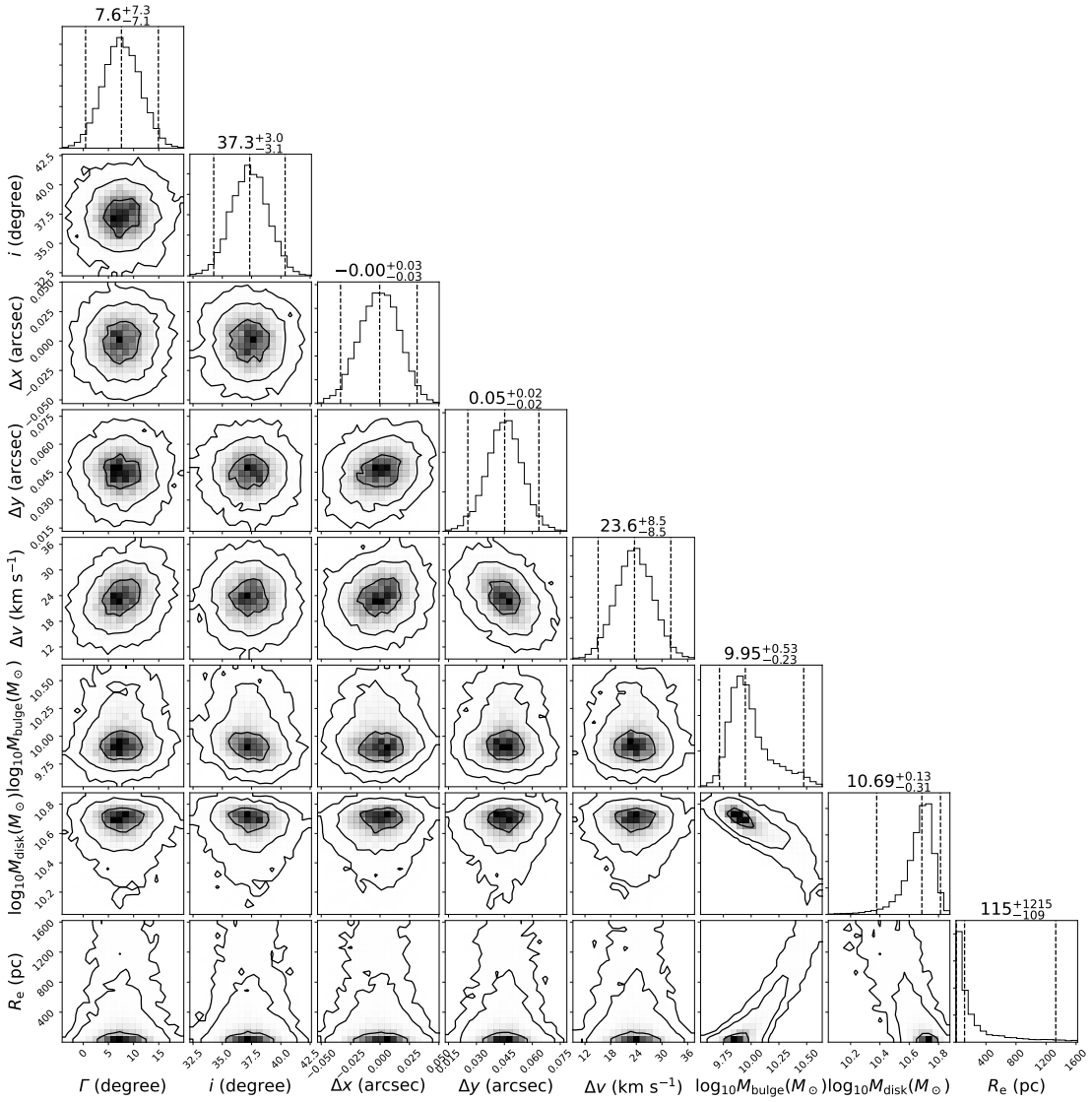

Figure 3.4: Posterior probability distributions of the eight model parameters using MCMC sampling of our gas dynamical model. The posterior probability distributions for the respective parameters were marginalized, and then the results are shown as the respective histograms along the diagonal panels. The dashed vertical lines in these histograms are the 2.5th, 50th, and 97.5th percentiles (95% confidence interval). The derived values of eight model parameters are indicated above the histogram, summarized in Table 3.3. The other panels show the covariances between all model parameters (contour levels are equivalent to 68%, 95% and 99.7% confidence intervals for the 2D Gaussian distribution).

Parameters (unit)	Symbols	Priors	Medians	95% confidence interval
Galactic mass model:				
Central compact mass ($10^9 M_\odot$)	$M_{\rm bulge}$	$[10^{-9}, 10^4]$	8.9	-3.7, +20.9
Disk mass ($10^{10} M_\odot$)	$M_{\rm disk}$	$[10^{-10}, 10^3]$	4.9	-2.5, +1.7
Central compact mass effective radius (kiloparsec)	R_e	[0.001, 1.625]	-	(<1.33)
Orientation of [CII] gas disk:				
Position angle (degree)	Γ	[-20, 20]	7.6	-7.1,+7.3
Inclination angle (degree)	i	(37.8 ± 1.6)	37.3	-3.1,+3.0
Nuisance parameters:				
[CII] center velocity offset (km s^{-1})	Δv	$[-60, 60]$	23.6	±8.5
[CII] center RA offset (arcsecond)	Δx	$[-0.15, 0.15]$	-0.00	±0.03
[CII] center Dec offset (arcsecond)	Δy	$[-0.15, 0.15]$	0.05	±0.02

Table 3.3: Best fit summary of our gas dynamical model. Column 1 shows the parameters and their units in our dynamical model. Column 2 shows the symbol used for each parameter. Column 3 shows the prior distributions used in our MCMC sampling, in which the values in brackets indicate the upper and the lower boundary of the uniform prior distribution, while the values in parentheses indicate the mean and standard deviation of the Gaussian prior. Columns 4 and 5 show the medians of posterior distribution, their associated 95% confidence intervals respectively. The upper limit on the effective radius Re of the central compact mass, is reported in parentheses. The reduced chi square χ^2 in our MCMC fitting is 1.69 under the degree of freedom of 42400.

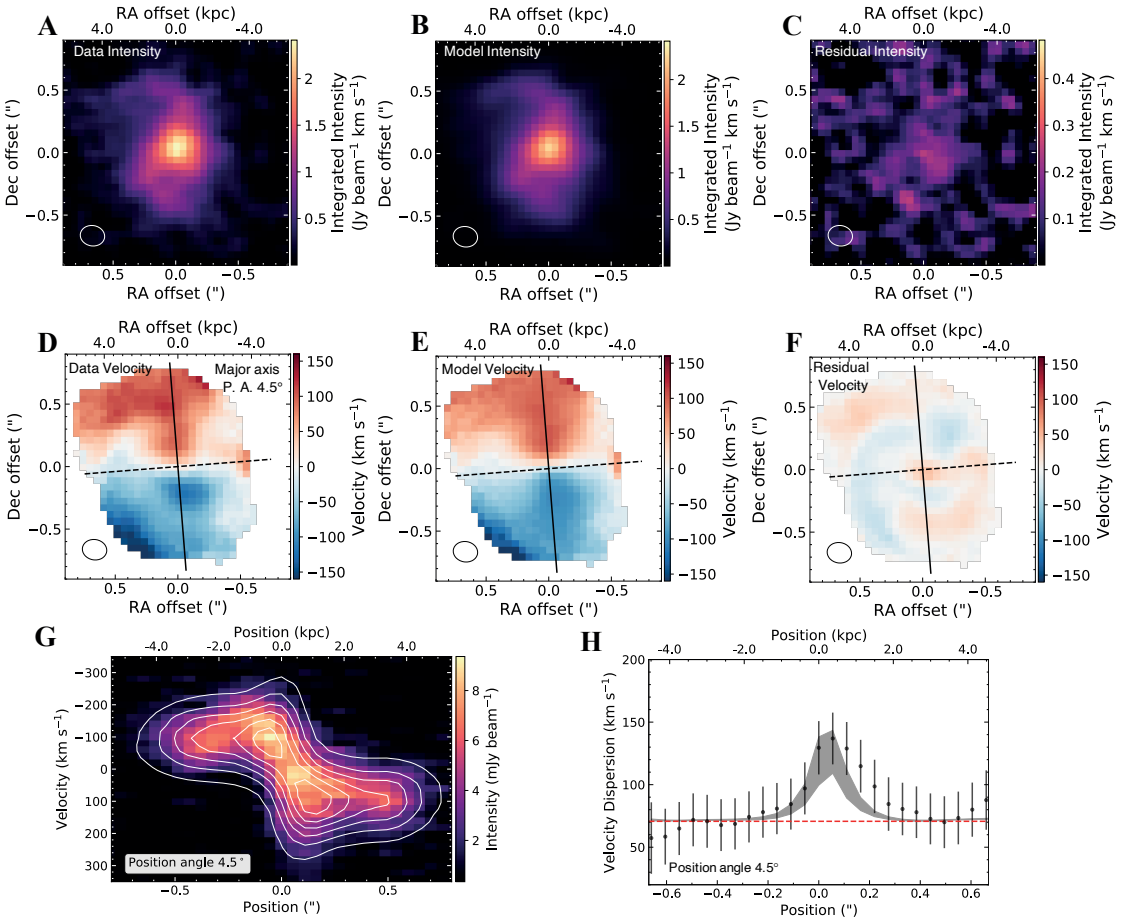

Figure 3.5: Morphology and kinematics of [CII] line in BRI 1335-0417 and their comparisons with gas dynamical models. (A) and (D) are the respective ALMA [CII] line maps of intensity (moment 0), intensity-weighted velocity (moment 1), same as Figs. 3.1 A and B respectively. (B) and (E) are the dynamical model maps with the central compact mass and disk taken into consideration, which correspond to (A) and (D). (C) and (F) are the residual maps between the observed [CII] line maps of (A) and (D) and the dynamical model maps of (B) and (E), respectively. The masked moment method (39) was used to produce the map (D). The same mask was applied to (E) for a fair comparison. Plotting symbols in (A-F) are the same as Figs. 3.1A and B. (G) shows the observed PVD of [CII] line emission (color, same as Fig. 3.1E) and model PVD (white contours: every $4\sigma_{\rm rms}$ from $3\sigma_{\rm rms}$ to 23 $\sigma_{\rm rms}$, where $\sigma_{\rm rms}$ is the root mean square noise of 0.35 mJy $beam^{-1}$). The model PVD was extracted along the kinematic major axis [see black solid line in (E)]. (H) shows velocity dispersion, which was measured by fitting a Gaussian with third and fourth-order Gauss-Hermite parameters h3 and h4 (76) to the line profile at each position of PVD (black points and error bars, same as Fig. 3.1F). This fitting used the pixels where [CII] line emission has a signal to noise ratio SNR > 4 in at least 4 velocity channels. (H) also shows velocity dispersion extracted from the model PVD in the same way (gray shade, showing 95% confidence intervals). The red dashed line is the same as Fig. 3.1F.

Here, we also consider the possibility that the radiation from active galactic nuclei (AGN) could influence the [CII] intensity distribution, which could bias our estimation of the disk scale radius and our dynamical modeling result. Since the [CII] profile is well described by the exponential profile which is typical to the disk, the influence of the AGN is considered to be small. If AGN radiation influenced the [CII] emission, the [CII] emission would become more concentrated, our size estimate of the disk would become smaller, and the true disk scale radius would be larger than our estimate. Furthermore, we investigated dependence of the best-fit $M_{\rm bulge}$ and $M_{\rm disk}$ on the disk scale radius R_d using several different values of R_d. In order to compare with them, we also derived the best-fit $M_{\rm bulge}$ and M_{disk} by adding the disk scale radius as a free parameter in our MCMC fitting. We confirmed that the derived masses of M_{bulge} are not sensitive to the disk scale radius (see Fig. 3.6).

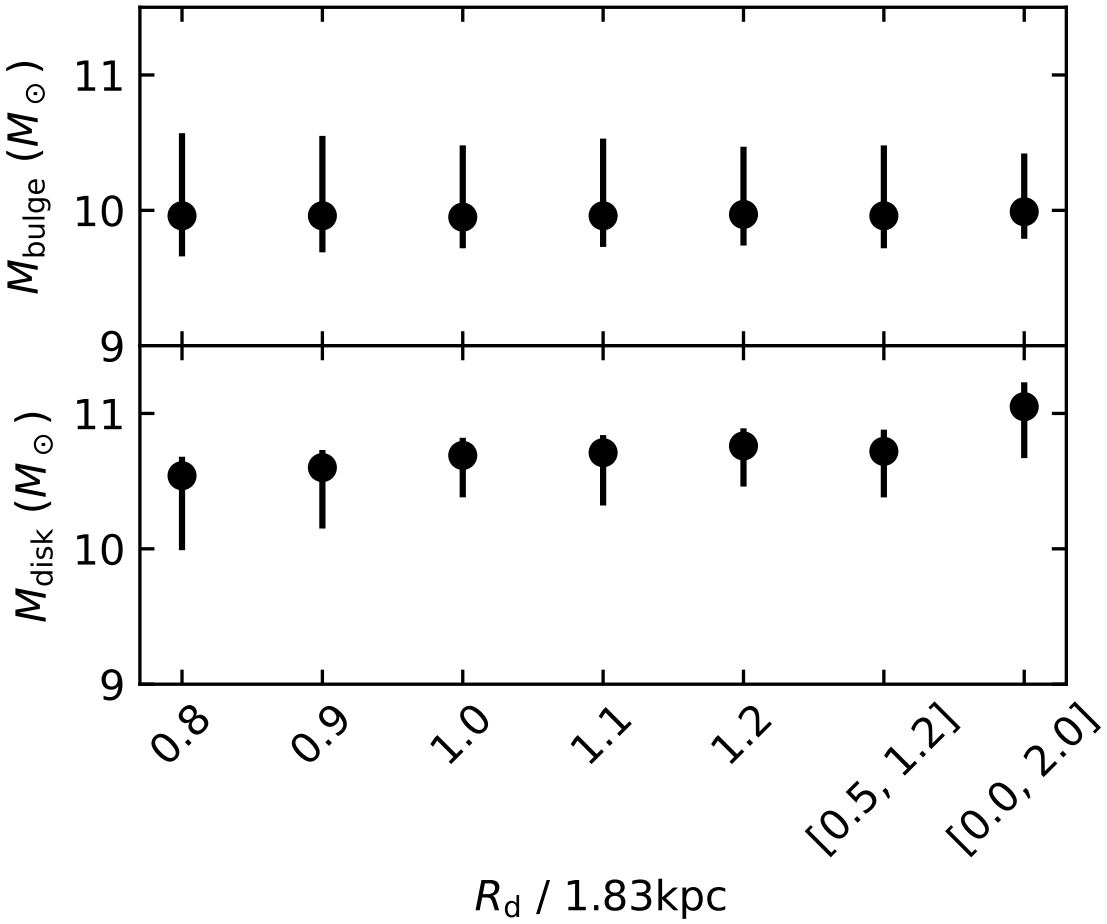

Figure 3.6: The dependency of derived physical parameters on the disk radius. Best fitting values of $M_{\rm bulge}$ and $M_{\rm disk}$ were derived using several values of the disk scale radius, shown normalized by our estimated value of R_d = 1.83 kpc (see Table S1). The disk scale radius was added as a free parameter in the MCMC fitting with the uniform prior range shown in brackets. The derived $M_{\rm bulge}$ is not sensitive to the disk scale radius.

The best-fitting effective radius of the compact structure R_e is less than 1.3 kpc (at 95 % confidence interval) and its mass is 5.2×10^9 to $3.0 \times 10^{10} M_\odot$ depending on the value of Re. These results are compatible with the typical effective radius and mass of stellar bulges in nearby galaxies (Gadotti, 2009). The modeled mass of the disk $4.9^{+1.7}_{-2.5} \times 10^{10} M_\odot$ is consistent with the molecular gas mass of $5.1 \times 10^{10} M_\odot$ (Jones et al., 2016) estimated from the CO (J=2→1) luminosity (assuming that BRI 1335-0417

has metal abundance of the sun).

Studies of nearby galaxies have revealed that a bulge and a supermassive black hole coexist in massive galaxies and that there is a strong correlation between them (Kormendy & Ho, 2013). The central black hole mass of $M_{\rm BH} = 6 \times 10^9 M_\odot$ was estimated in a previous study from the virial theorem with the broad line width , although there are a number of systematic effects (e.g., the variable luminosity, blending with other broad emission feature, and unknown gas kinematics and distribution) that could bias the black hole mass estimation (Mejía-Restrepo et al., 2018). The virial black hole mass is in the range of our derived compact structure mass 5.2×10^9 to $3.0 \times 10^{10} M_\odot$, indicating that a bulge and a central black hole coexist in the central compact structure or leaving room for a possibility of a black hole without a bulge. The ratio of virial black hole mass to the compact structure mass is 1 to 0.2, which is higher than the black hole to bulge mass ratio of 0.001 to 0.002 observed in nearby galaxies (Kormendy & Ho, 2013). Several studies have reported evidence that the black hole-bulge mass ratio in high redshift galaxies is higher than at low redshift, but it is still inconclusive in the current studies (Schulze & Wisotzki, 2014). In order to separately measure the black hole mass and bulge mass and assess the possibility of a black hole without bulge, we need to obtain the brightness distribution of stars (Davis, 2014) in this object.

3.3.2 Identifying Spiral Structure

To quantitatively measure the degree of the spiral structure, we decomposed the [CII] line intensity distribution of BRI 1335-0417 into m-armed logarithmic spirals, $\rho = \rho_0 \exp(-m/p(\phi + \phi_0))$ in polar coordinates (ρ, ϕ). p is a variable related to the pitch angle ϕ by $p = -m/\tan(\phi)$, and ρ_0 and ϕ_0 are an arbitrary constant. We first

deprojected the [CII] line intensity image to be viewed as face-on using the position angle 4.5° and inclination 37.8° that are measured by GALFIT and PaFit Package (Table 4). The image rotation and stretching for the deprojection are performed using the scikit-image package, in which mapping the original pixels onto a new pixel grid is done by Bi-linear spline interpolation. From the deprojected image, we then calculated the Fourier amplitude (Law et al., 2012; Kalnajs, 1975; Puerari & Dottori, 1992), which indicates the magnitude of the m-armed logarithmic spirals. It follows that

$$A(p,m) = \frac{1}{D}\Sigma_{j=1}^{N} f_j \exp(-i(pu_j + m\phi_j)) \tag{3.11}$$

where $D = \Sigma_{j=0}^{N} f_j$ is the sum of the flux f_j of the pixel j in the image, u_j is the logarithmic radius from the center of the image and ϕ_j is the polar angle. We excluded the central region of 1.6 kpc and the region outside of 7.2 kpc for the calculation of $A(p,m)$ in order to avoid the effects of unresolved components and noise. The center of the polar coordinate is defined as the pixel which has a peak intensity in the [CII] line image. Figure 3A shows the Fourier amplitude $A(p,m)$ as a function of p for $m = 1, 2, 3, 4$. Its underlying noise level was estimated by applying equation 3.11 on 300 noise maps extracted from the emission line region of the data cube and computing their 84th percentile. The strongest and narrow peak is seen in $m = 2$ at $p = -4.0^{+0.6}_{-0.3}$, corresponding to spiral arms with a pitch angle of $\alpha = 26.7^{+4.1}_{-1.6}$ ° at the 95% confidence level. The confidence interval is estimated by Monte Carlo simulation propagating the error ranges of the position angle and inclination of the disk used for the image de-projection. Figure 3.7B shows this model overlain on the [CII] line intensity image after correction for the inclination angle of 37.8° (i.e., de-projected to be viewed as face-on). The amplitude of the $m = 2$ signal is 6.0 times the noise, while the other modes

$m = 1, 3, 4$ have signal-to-noise ratios of 4.0, 2.5 and 2.4 respectively (Fig. 3.7A). The $m = 1$ mode corresponds to a one-arm spiral or lopsided morphology. The signal in $m = 1$ mode (Fig. 3.2A) is due to the difference in length of two arms (Fig. 3.2B). The $m = 3$ and 4 modes correspond to a triangular and boxy shape, respectively, which could be produced by a stellar bar structure.

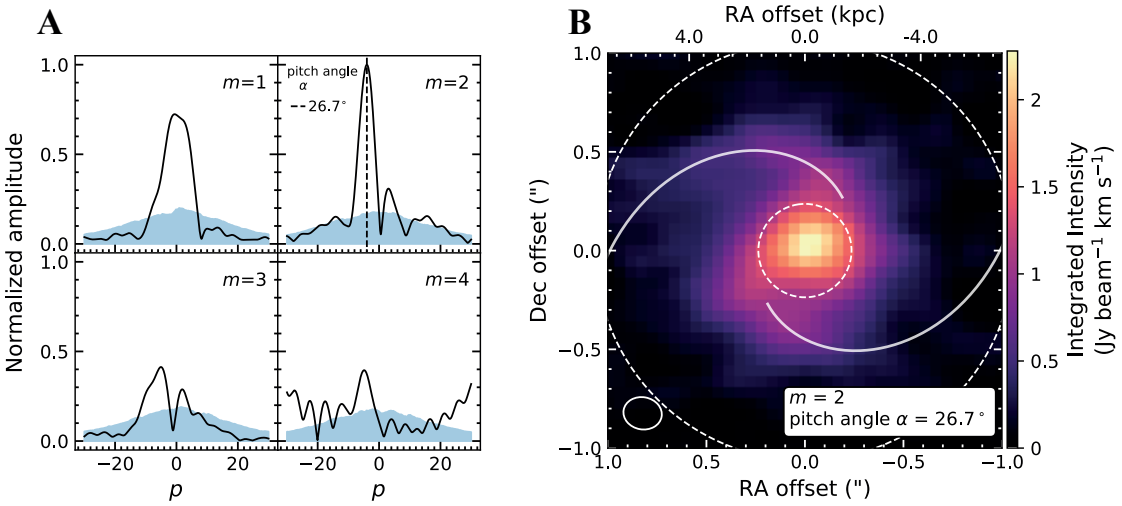

Figure 3.7: Fourier analysis of the [CII] line emission. (A) Fourier spectra of model logarithmic spirals with m arms and pitch angles α. The black solid lines show normalized amplitude as a function of the dimensionless parameter $p = -m/\tan(\alpha)$. The blue shaded region indicates the estimated noise level (14). The $m = 2$ mode has the strongest peak at a pitch angle of $26.7^{+4.1}_{-1.6}$ ° (dashed vertical line). (B) the [CII] line intensity image (de-projected version of Fig. 3.1A) overlaid with the best-fitting two-armed logarithmic spiral (white line, same as in Fig. 3.2). An ellipse shows the FWHM of the synthesized beam in the left bottom corner. The inner and outer dotted lines indicate the boundaries of the region used in the Fourier analysis.

Dynamical Stability of the Disk

The dynamical stability of the disk against perturbations is quantified using the Toomre Q parameter. For a gas disk, the parameter is given by (Toomre, 1964; Goldreich &

Lynden-Bell, 1965)

$$Q = \frac{\sigma_v \kappa}{\pi G \Sigma_{\rm gas}} \tag{3.12}$$

where κ is the epicyclic frequency, $\Sigma_{\rm gas}$ is the surface density of the gas, and σ_v is intrinsic velocity dispersion of the gas. κ is given by

$$\sqrt{2\left(\frac{v_{\rm rot}^2}{r^2} + \frac{v_{\rm rot}}{r}\frac{{\rm d}v_{\rm rot}}{{\rm d}r}\right)} \tag{3.13}$$

When $Q < 1$, the disk is unstable against the perturbations because the self-gravity of the gas overwhelms the local pressure forces due to the turbulent motion and the differential rotation (Toomre, 1964; Goldreich & Lynden-Bell, 1965). Because the total gas mass is traced by the [CII] line (Zanella et al., 2018; Gullberg et al., 2018), we estimated the surface density of the gas $\Sigma_{\rm gas}$ by using the total molecular gas mass $M_{\rm gas} = 5 \times 10^{10} M_\odot$ (Jones et al., 2016) and the [CII] line distribution we observed. The rotation velocity was derived from our gas dynamical modeling. Using these parameters, we derived Toomre Q parameter for each spatial pixel (Fig. 3.8, A and B). The error bars in Fig. S3.8B reflect the uncertainty of the model rotation velocity at 95 % confidence interval. We find Q is less than 1 throughout the outer part of the disk (Fig. 3.8), indicating the gas disk is susceptible to gravitational collapse, star formation (Rizzo et al., 2020; Neeleman et al., 2020; Tadaki et al., 2018) and spontaneous formation of spiral structure (Law et al., 2012; Dobbs & Baba, 2014).

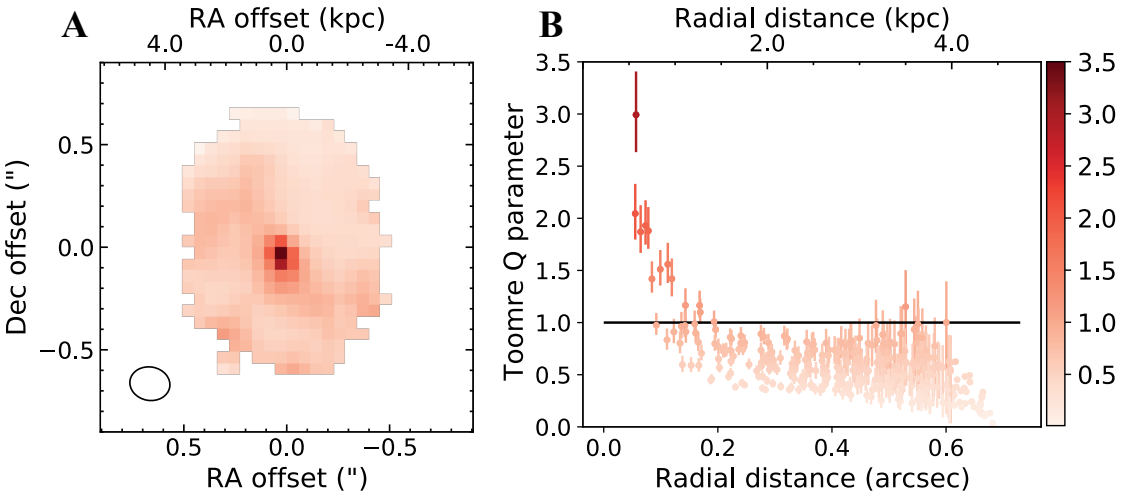

Figure 3.8: The Toomre parameter Q for the gas disk of BRI 1335-417. The spatial distribution of Toomre parameter Q for the gas disk is shown in (A). The Q was derived using rotation velocity, intrinsic velocity dispersion, and the surface density of the gas. The radial distribution of Q is shown in (B), where each pixel in (A) is plotted in radial distance deprojected to a disk plane. Over the outer part of the disk (at the radius of $R >$ 0.2"), Q is < 1, implying that the gas disk is unstable against the perturbations. The error bars reflect the uncertainty of the 95% confidence interval of the dynamical model. This measurement only used pixels where the [CII] line emission is detected at SNR > 4 in at least 4 velocity channels.

3.3.3 Major merger vs. Rotating Disk

Although dusty starburst galaxies like BRI 1335-0417 are thought to be formed mainly through major mergers, a sample of starburst galaxies in a certain field suggests a high duty cycle (Mitsuhashi et al., 2021), indicating a complex mechanism for starbursts that is not yet well understood (McAlpine et al., 2019) (continuous merger, gas accretion, violent disk instability). In order to reveal the star-forming mechanism of the galaxy population, it is important to classify galaxies into either major mergers or ordered rotating disks and study their demographics of mergers and disks within the population as a function of the cosmic epoch. Conducting quantitative classification was complicated

by the limited angular resolution and sensitivity for the high redshift galaxy sample. For BRI 1335-0417, there are several pieces of evidence in [CII] and dust kinematics that the galaxy is not in the process of a major merger. (1) Intensity distribution of [CII] and dust show a single peak with a given spatial resolution of $\sim$ 1.33kpc $\times$ 1.11 kpc, which clearly rejects an early-stage major merger with a separation larger than 1.3 kpc. (2) The [CII] velocity map is spatially resolved by 70 resolution elements, showing well-ordered rotating disk signature, with the iso velocity lines radiating outward from the center, like a "spider" diagram (van der Kruit & Allen, 1978). (3) The central rise of [CII] gas rotation velocity seen in the PVD indicates the centrally concentrated mass distribution in the center. Furthermore, the continuum dust emission in this object coincides with the center of the rotation dominated disk (see Figs. 3.1 B and C) within the beam, indicating that the compact structure like a bulge and/or a central black hole resides in the center of the gravitational potential, which disfavors the remaining possibility that two galaxies orbit each other around the center of mass with almost zero separation. Since this object has a rotating disk and a compact structure formed in its center, sufficient time for their formation likely has passed after the significant merger event. The orbital period at the effective radius of the disk $1.678R_d$, where the rotation velocity is well constrained, is about 120 Myr. If the disk may need about five orbital periods to be relaxed, major merger events must have happened at a redshift of z>7. This dynamical time scale is much longer than the gas depletion time of 10 Myr estimated based on the SFR of 5000 $M_{\odot}$yr^{-1}(SED modeling; Wagg et al. 2014) and molecular gas mass (CO(2-1) luminosity assuming solar abundances; Jones et al. 2016). This may suggest that additional mechanisms other than major merger events (i.e., continuous gas and satellites accretion from a large gas reservoir, violent disk instabilities) are required to drive and sustain the estimated high SFR.

We also quantify the symmetry of the velocity map and velocity dispersion map of BRI 1335-0417 to conclude whether the system is a disk or merger quantitatively. For this purpose, we made the mean velocity map and velocity dispersion map by fitting Gaussian Hermite function (Cappellari, 2017) to the spectrum of each spatial pixel in the [CII] 3d cube (2d position and velocity) rather than moment maps to maximally benefit from the high quality [CII] data with high signal to noise ratio. We only used pixels in which [CII] emission is detected with 3 sigma in at least 3 velocity channels. We then measured the asymmetry following Shapiro et al. (2008) using KINEMETRY code (Krajnović et al., 2006). First, we measured the azimuthal profiles of the velocity and velocity dispersion maps along concentric ellipses having an increasing semimajor axis. Then, we expand the azimuthal profiles of the velocity map and velocity dispersion map along the concentric ellipse with Fourier series as (Krajnović et al., 2006)

$$\begin{aligned} K(\psi) =& A_0 + A_1 \sin(\psi) + B_1 \cos(\psi) \\ &+ A_2 \sin(2\psi) + B_2 \cos(2\psi) + \cdots \end{aligned} \tag{3.14}$$

or more compact form,

$$K(a, \psi) = A_0(a) + \sum_{n=1}^{N} k_n(a) \cos\{n\,[\psi - \phi_n(r)]\} \tag{3.15}$$

with amplitude and phase coefficients

$$k_n = \sqrt{A_n^2 + B_n^2} \text{ and } \phi_n = \arctan\left(\frac{A_n}{B_n}\right). \tag{3.16}$$

We quantified the symmetric measure for velocity and velocity dispersion maps with

$$v_{\rm asym} = \left\langle \frac{k_{{\rm avg},v}}{B_{1,v}} \right\rangle_r \tag{3.17}$$

and

$$\sigma_{\rm asym} = \left\langle \frac{k_{{\rm avg},\sigma}}{B_{1,v}} \right\rangle_r , \tag{3.18}$$

with

$$k_{{\rm avg},v} = \left(k_{2,v} + k_{3,v} + k_{4,v} + k_{5,v}\right)/4 \tag{3.19}$$

and

$$k_{{\rm avg},\sigma} = \left(k_{1,\sigma} + k_{2,\sigma} + k_{3,\sigma} + k_{4,\sigma} + k_{5,\sigma}\right)/5, \tag{3.20}$$

as defined by Shapiro et al. (2008), where subscripts number n, v and σ denote for the n-th Fourer coefficients for the velocity and velocity dispersion maps defined in equations ,3.15 and 3.16, and the bracket denotes the average of the measurements for all ellipses with different semi-major axis. Figure 3.9 shows our measurement of BRI 1335-0417 ($v_{\rm asym} = 0.086$, $\sigma_{\rm asym} = 0.074$) in $v_{\rm asym}$- $\sigma_{\rm asym}$ space with the empirical boundary of disk and merger $K_{\rm asym} = \left(v^2_{\rm asym} + \sigma^2_{\rm asym}\right)^{1/2} = 0.5$ defined by Shapiro et al. (2008) using the artificially redshifted observed data or simulated galaxies of known merger and disk (shown with background color points with blue and red respectively). BRI 1335-0417 clearly locate well within the region $K_{\rm asym} = \left(v^2_{\rm asym} + \sigma^2_{\rm asym}\right)^{1/2} < 0.5$ occupied by the disk galaxies.

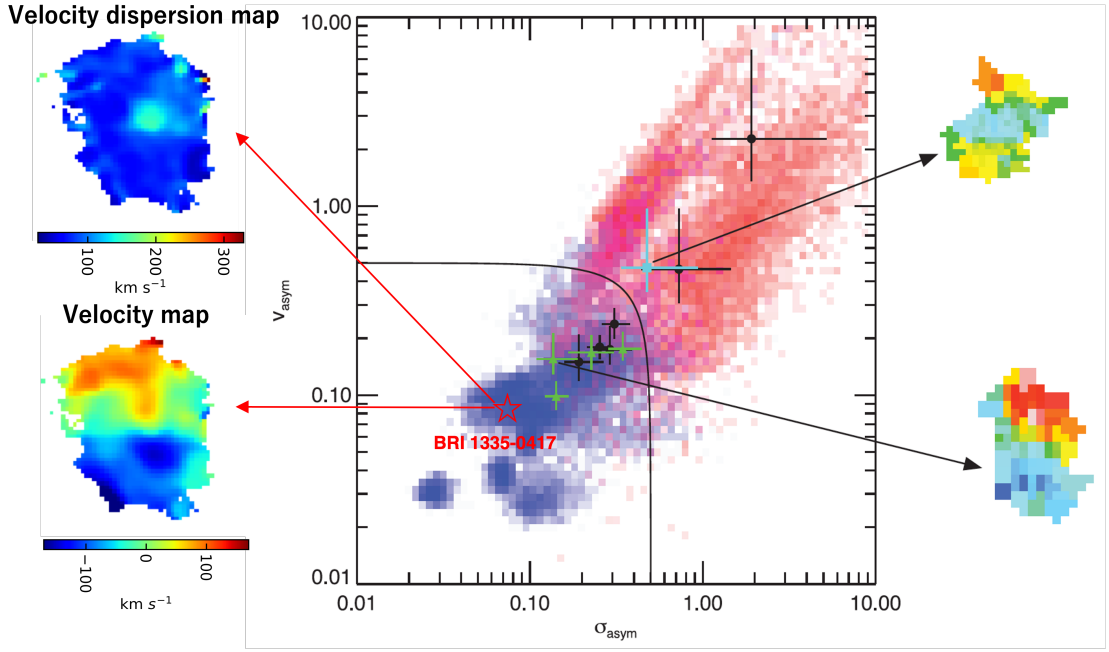

Figure 3.9: Asymmetric measures of velocity and velocity dispersion maps, v_{asym}, σ_{asym} for the SINS (the Spectroscopic Imaging survey in the Near-infrared with SINFONI) galaxy samples (black dots) and probable disk-like galaxies and a merger-like galaxy reported in the literature (Shapiro et al., 2008). We added the measurement of BRI 1335-0417 highlighted with a red star. Background colors are the probability distribution function of the measurements for artificially redshifted observed data or simulated galaxies of known merger (red) and disk (blue). Example velocity maps of merger-like and disk-like galaxies from SINS galaxies are shown in the right, while the velocity and velocity dispersion map of BRI 1335-0417 are shown on the left. The figure is adapted from Shapiro et al. (2008).

3.4 Discussion of This Chapter

The dusty starburst galaxies like BRI 1335-0417 are considered to be the progenitors of present-day massive elliptical galaxies, which are dominated by the old stellar population (Zolotov et al., 2015; Toft et al., 2014). This transformation requires the contraction of the disk by the efficient angular momentum transport through gravitational torques of non-axisymmetric structures (Dekel & Burkert, 2014). The color composite image and

velocity channel images of [CII] line (see Fig. 3.1D and Fig. 3.2) show a two-armed spiral morphology. Although the spiral galaxies have been found up to redshift z of about 2.67 (Law et al., 2012; Yuan et al., 2017; Dawson et al., 2003) so far, in this paper, we first identify a spiral morphology in this high-redshift galaxy (z = 4.41) long before the peak of the cosmic star formation. We witness that the spiral structure plays a significant role in the evolution of this galaxy: the angular momentum of the galactic material is redistributed and transferred through the gravitational torque generated by non-axisymmetric structure, triggering the gas inflow into the center of the galaxy and driving nuclear starbursts (Dekel & Burkert, 2014). This object may have a gas-dominated disk being continuously fed by the smooth gas accretion and gas-rich merger (Dekel et al., 2009). Such disk with excessive gas undergoes violent disk instability (Dekel & Burkert, 2014), which produces compact massive clumps and extended transient structures, shown in the cosmological numerical simulation (Inoue et al., 2016). Two-armed spiral morphology observed in this object could be induced in the disk through tidal interactions (Law et al., 2012; Dobbs & Baba, 2014). By the cosmological simulation at redshift of 6 (Kohandel et al., 2019), a spiral structure on [CII] rotating disk is shown to appear when the disk is relaxed after the successive merger events. The two-armed spiral morphology is extended up to 5kpc (Fig. 3.1A), connected to the galaxy center (Fig. 3.1D) and well associated with the rotating disk spatially and in velocity (Fig. 3.5 and Fig. 3.1E), while tidal-tail features in a galaxy merger are expected to be seen in much larger scale (>10kpc) (Hodge et al., 2019; Ren et al., 2020). Thus, the observed spiral morphology is inconsistent with large-scale tidal features. We therefore disfavor, but cannot completely rule out, a tidal-tail origin for the observed spiral morphology. Besides the above possible formation scenario of two-armed spiral morphology, the formation and amplification mechanism of the

spiral structure by stellar bar may work in this object (Dobbs & Baba, 2014; Baba, 2015). The images of [CII] line intensity and dust continuum (Fig. 3.1, A and C) show the non-axisymmetric structure like a bar, and the spiral arms appear to begin from the edge of this bar structure, which is similar to those seen in nearby disk galaxies and also consistent with the grand-design spiral arms in barred galaxies as proved by numerical simulation (Baba, 2015). In order to reveal whether the spiral arms are the stable, transient, or dynamic structure which is repeatedly generated and destroyed, it is important to compare the distribution and kinematics of the stars and gas with the numerical simulation (Dobbs & Baba, 2014) resembling the typical properties of high redshift galaxies such as high gas fraction and accretion rates.

3.5 Concluding Remarks of This Chapter

Spiral galaxies show distinct structures such as bulge, disk, and spiral arms. When and how these structures were formed in cosmic history is a perennial question being intensively explored in galaxy formation. Aiming to identify the galactic structures and formation at the early universe, we analyze observations of BRI 1335-0417, an intensely star-forming galaxy in the distant universe, at redshift 4.41. The [CII] gas show rotation kinematics with a steep rise of velocity in the center, two-armed spiral, and bar morphology. We interpret these features as a central compact structure, such as a bulge, a rotating gas disk, and spiral arms. These features had been formed within 1.4 billion years after the Big Bang, long before the peak of cosmic star formation.

BRI 1335-0417 is a typical example of extremely star-forming galaxies at $z > 4$ with an estimated star formation rate of about $5000 M_{\odot}$ yr^{-1}. Such a high star formation rate is commonly explained by a major merger scenario, which may show heavily

distorted galactic kinematics. Surprisingly, the high angular resolution observation of [CII] kinematics using ALMA shows that BRI 1335-0417 has slightly disturbed, rotation-dominated kinematics, which can be well described by the rotating disk model. This suggests that the extremely high star formation rate needs to be maintained for the period of time required for the disk to be formed after the major merger event. BRI 1335-0417 is likely to be subject to the violent disk instability driven by continuous gas accretion along the large-scale filaments of the cosmic web (Dekel et al., 2009; Dekel & Burkert, 2014), and/or minor mergers with the accreting satellites along with the gas accretion (Kohandel et al., 2019). In addition to the rotating disk, BRI 1335-0417 has a two-armed spiral morphology and a central steep rise of the velocity, which is a signature of the presence of a central compact structure. Recent high angular resolution observation of ALMA have shown detailed galactic structures and new picture of galaxy evolutions: early disk formation (Rizzo et al., 2020; Neeleman et al., 2020; Tadaki et al., 2018; Lelli et al., 2021), early bulge formation (Rizzo et al., 2020; Lelli et al., 2021) and possible disk substructure (Lelli et al., 2021) in dusty star-forming galaxies at redshift $z > 4$. These galactic structures could not be recognized by low angular resolution observations. There may be a diversity in the dynamics, structure, and physical conditions of these dusty star-forming galaxies, which suggests their different evolutionary stages or scenarios. We demonstrated that high angular resolution observation of [CII] kinematics towards a number of dusty star-forming galaxies might reveal their structures in distribution and kinematics, and their comparison for a large number of galaxies will shed light on the detailed driving mechanism of the most intense star formation in the universe.

4

Conclusion and Future Prospects

Conclusion

The main focus of this paper is to explore the formation and evolutionary processes of galaxies through studying the dynamics and mass distribution of galactic internal structures, each of which is suggested to drive or regulate the evolution of the galaxy. We studied two contrasting galaxies, which allows us to investigate detailed gas and/or stellar kinematics with currently available data: the massive early-type galaxy NGC

1380 at redshift of 0.006 and the distant rapidly evolving galaxy with a significant star formation rate, BRI 1335-0417 at redshift of 4.4 to reveal the formation and evolution of galaxies. In NGC 1380, We identified the internal structures: a central black hole, a bulge, a disk, a stellar halo, and a dark matter halo. We show a consistent picture of the underlying stellar structure both by the non-parametric decomposition of luminosity into the round and flat structures and by analyzing the independent stellar kinematics data (i.e., V/σ profile and σ_ϕ/σ_R), which suggests pressure support and rotation support structures. We measured the respective mass distributions accounting for the distinct kinematical properties of stellar structures (round and flat structures) motivated from the observed data. We construct the stellar dynamical model with the prior information of the ALMA-derived mass model, which helps to constrain the bulge's orbital anisotropy and relax the mass and anisotropy degeneracy over the galaxy. We found that the disk of NGC 1380 is stabilized against the bar mode instability not only by the dark matter but also the central bulge component, which may explain its absence of significant disk substructures like bar and spirals.

In BRI 1335-0417, we identified the rotating disk structure and central bulge structure that had already been formed at this epoch. Our estimated dynamical mass is comparable to the molecular gas mass estimated assuming solar metalicity, indicating that the contribution of the dark matter is less significant at the [CII] disk region. On the other hand, BRI 1335-0417 shows a spiral and bar-like structure in the disk, which is dynamically unstable in terms of Toomre Q parameters. Our dynamical modeling with the simple assumption of disk and bulge structures results in the disk mass, which is consistent with the estimated molecular gas mass in a previous study (Jones et al., 2017) assuming solar metal abundance. A recent study using detailed gas dynamics in a lensed galaxy at a similar epoch (redshift of 4.24) reports the conflict between dynamical mass

and gas mass, suggesting the tracer luminosity to gas mass ratio may be 4 times smaller than Galactic values (Dye et al., 2021). This result supports similar conflicts reported in the literature (Mizukoshi et al., 2021; Calistro Rivera et al., 2018). If we assume the estimated gas mass is correct, the mass of the DM and stars contained in the disk is 30% at maximum, which may make the gas disk of BRI 1335-0417 unstable to the bar-mode instability. Also, the galaxy may be gas-dominated, containing 70% of mass in the disk, which is subject to the violent disk instability to form spiral arms and bar structure seen in this object (Dekel & Burkert, 2014; Inoue et al., 2016). The estimated gas depletion time scale is shorter than the dynamical time scale required to form a relaxed disk after a significant major merger event. This difference of the timescale may suggests the additional mechanism other than major merger (i.e., continuous gas and satellites accretion from a large gas reservoir, violent disk instabilities) is responsible for driving and sustaining the high SFR. To conclude, although we studied only two galaxies contrasting their physical properties, we show that the dynamical instability in terms of the fraction of spherical structures (bulge and dark matter halo) may explain the observed slow/rapid galaxy evolution (star formation) and absence/presence of a significant bar and spiral structures in both NGC 1380 and BRI 1335-0417.

Future prospects

There are prospects for the remaining works in this thesis as listed below.

For the study of the nearby early-type galaxy NGC 1380 presented in Chapter 2;

- Our estimation of the stellar M/L is purely dynamical. The uncertainty of stellar M/L is large at large radii, which requires us to assume the simple profile of M/L; linearly decreasing at the center and constant beyond some radius. This simple

assumption is motivated by the result of the spectrum modeling in early-type galaxies (van Dokkum et al., 2017). The mass profile of stars should not change significantly even with the large uncertainty in stellar M/L because the stellar surface brightness decreases rapidly from the center. However, if the degree of freedom in the stellar M/L parameters (i.e., M/L_0, $M/L_{5\mathrm{arcsec}}$, r_{break}) can be reduced by the knowledge of the stellar population and stellar spectrum, it may be possible to use a more general profile for dark matter than the NFW (i.e., generalized NFW profile (Zhao, 1996)) and constrain the inner slope of the dark matter profile, which require higher accuracy to do so than just to measure the enclosed mass profile.

- In our non-parametric decomposition between the round bulge-like structure and the flat disk, we have not estimated the statistical uncertainty of the decomposition. As the spatial resolution of the telescope increases in the future and the quality of observational data improves, we expect the data to reveal more complex structures that cannot be described by the parametric disk and bulge. In such a case, it is advantageous to use the non-parametric structure decomposition demonstrated in this thesis. There is room to improve the code so that it can efficiently estimate the statistical uncertainty of the non-parametric decomposition.

For the study of high-redshift galaxies presented in Chapter 3.

- The star formation rate of BRI 1335-0417 was estimated to be 5000 $M_\odot$ yr^{-1} by SED modeling, which is extraordinarily high compared to galaxies at similar epoch (e.g., z>6; quasar host galaxies Decarli et al. 2018; sub-millimeter galaxies Dudzevičiūtė et al. 2020). This estimated SFR also makes BRI 1335-0417 a significant outlier in the Kennicutt -Schmidt diagram (Figure 10 in Jones et al.

2016). Its star formation rate is estimated from the SED modeling by Wagg et al. (2014) in which they assumed that the QSO contribution is negligible. Thus, the estimated star formation rate can be overestimated and should be considered as an upper limit. In diagnostics probing physical condition of ISM (which does not require the model assumption about the AGN contribution) such as $L_{[\mathrm{CII}]}/L_{\mathrm{FIR}}$ - $L_{\mathrm{CO}(2-1)}/L_{\mathrm{FIR}}$, BRI 1335-0417 seems to be not an outlier (De Breuck et al., 2011). Also, in $L_{[\mathrm{CII}]}/L_{\mathrm{FIR}}$ - L_{FIR} diagram, BRI 1335-0417 resides in the region occupied by luminous quasar-host galaxies (Ferkinhoff et al., 2013; Izumi et al., 2019). Our data provides us with the dust continuum map, showing the compact structure and extended disk, but [CII] shows an exponential profile like a disk. If we obtain additional data in the future at other wavelengths with comparable resolution, we may be able to remove the QSO contamination and derive the accurate star formation rate by the spatially resolved SED modeling and [CII] luminosity distribution.

- BRI 1335-0417 is a quasar-host galaxy (Shields et al., 2006) showing a bar-like structure in the center. Bar structures are suggested to play an essential role in feeding the gas to the quasar (Hopkins & Quataert, 2010). We would like to perform a quantitative analysis of this bar structure and possible non-circular motions due to the structure in BRI 1335-0417 in order to understand the dynamical role of the bar structure in distant quasars.

- From the exponential nature and rotation kinematics of [CII] emissions, we concluded that the [CII] emission of BRI 1335-0417 is emitted from the rotating disk structure. The current data does not require an additional [CII] component to explain the observed [CII] intensity distribution. Recently, Fujimoto et al.

(2020) shows that some of the isolated star-forming galaxies (30% in their sample) have extended [CII] emission out to 10 kpc scales beyond the size of rest-frame UV and FIR continuum. Our measurement shows the size of [CII] (3.07 ± 0.07 kpc) is more extended than the dust continuum (1.40 ± 0.02 kpc; see Table), which is consistent with the trend, the [CII] emission may be more extended than FIR emission suggested by stacking analysis of galaxies at a redshift of 5 to 7 (Fujimoto et al., 2019). The current data was taken in relatively short integration time (1h) and higher resolution (∼ 1 kpc) relying on the extremely luminous emission from BRI 1335-0417, therefore the data is not sensitive to the faint and extended structures compared to Fujimoto et al. (2020). Future observation with a more compact array configuration or longer integration time may reveal the extended [CII] emission in this source and allow us to constrain the extended mass distribution from the possible rotation dynamics.

- The gas mass fraction of 70 percent may be consistent with the gas mass fraction of 50 to 80 percent in galaxies at redshift $z = 2$ with a stellar mass of $2 \times 10^{10} M_{\odot}$ (see figure 9 in Tacconi et al. 2020). There have been no observations that can map out the stellar distribution of this galaxy. We think high-resolution JWST observation can measure the mass distribution of stars and provide us a stellar-mass content and the remaining dark mass allowed in the galaxy.

A

Appendix

A.1 Correlated noise modeling

Recent developments in radio interferometry have made it possible to spatially resolve the brightness distribution of astronomical objects. The imaging is generally done by setting about 3-5 pixels for the FWHM of the main lobe of the synthesized beam (i.e., point spread function). In addition, the synthesized beam has a complex sidelobe structure that

is determined by the sampled spatial frequencies of observation[1]. Therefore, the noise and signal in neighboring pixels correlate each other. The sidelobe structure can be removed only for signal which have high signal to noise ratio (S/N) by the general imaging method of interferometer such as CLEAN). For this reason, the noise correlation property differ from observation to observation, and correlated noise makes it difficult to evaluate the statistical significance of detections and findings in radio astronomy data. As far as we know there are no papers that discussed the significance of detection (uncertainty of integrated flux or spectrum) or image analysis considering the detailed noise correlation properties (e.g., see also Refregier et al. 2012 for discussing the noise correlation of VLA data and its effect on weak lensing analysis.)

The noise in one channel (image at a certain velocity) can be estimated by measuring the variance of pixel values in the emission-free region. In a spatially resolved image, one should be careful to estimate the statistical error (due to fluctuations in pixel values and correlated noise) associated with the spectrum or flux integrated over a region of the celestial sphere. In the case of uncorrelated noise, the statistical error can be simply (rms noise)$\times\sqrt{N_{\rm pix}}$, where $\rm N_{pix}$ is the number of pixels of the integrating region (increasing propotion to $N_{\rm pix}$). If the signal is uniformly present in each pixel, the S/N increase as $\sqrt{N_{\rm pix}}$ with $N_{\rm pix}$ in the case that noise is not correlated. However, the S/N will not at all increase with $N_{\rm pix}$ for perfectly correlated noise. When adding up the flux distributed over many pixels in images, the correlation of noise in each pixel must be considered appropriately. Therefore, understanding the characteristics of correlated noise will become increasingly important in the future for interpreting the images of high-resolution radio interferometry and for the intensity mapping study of HI gases

[1], The sampled spatial frequencies depend on the antenna configuration, the sky position of the source, and the observation time.

distributed in large-scale structures, probed by SKA or single-dish telescopes. Monte Carlo simulation is often used to to evaluate the significance of analysis performed on images, repeatedly adding random noise to the original image and performing the analysis. Using uncorrelated noises instead of correlated noise also leads to incorrect estimation of the noise effect.

In this appendix, we show that the correlation property of the noise in the ALMA data is similar to that of the synthesized beam pattern of the interferometer, and that the noise can be regarded as the uncorrelated noise convolved by the synthesized beam of the interferometer. In addition, to evaluate the statistical significance of the results obtained by image analysis, we summarize the method to generate randomly correlated noise by modelling spatially correlated noise in ALMA data and general images taken by interferometer. As a remaining future work, we would introduce and test the method to derive the statistical uncertainty associated with the spectra or fluxes obtained by spatially integrating the region of sky in images obtained by the interferometer, taking into account the noise correlation.

The discussion in this appendix can be exactly applicable to and is equally important for the image obtained by the single dish telescope (i.e. on-the-fly mapping observation), because of the large telescope beam and its non-negligible sidelobe structures. In addition, the pointing of the telescope is wobbly due to the wind, which causes the effect of further smoothing the observed brightness distribution and leads to noise correlation.

A.1.1 Noise characterization

First, we consider the intensity $I(\mathbf{x})$ of a 2D image, where $\mathbf{x}$ denote the pixel positions. The intensity $I(\mathbf{x})$ can be divided into the intensity from the detected sources $S(\mathbf{x})$ and

the noise $N(\mathbf{x})$,

$$I(\mathbf{x}) = S(\mathbf{x}) + N(\mathbf{x}). \tag{A.1}$$

The noise $N(\mathbf{x})$ includes the Cosmic Microwave Background (CMB), the thermal noise associated with the instrument, and all emission from the undetected sources.

$N(\mathbf{x})$ is assumed to have mean and variance for each pixel;

$$\begin{aligned} \langle N(\mathbf{x}) \rangle &\equiv \mu \quad \text{and} \\ \langle N(\mathbf{x})^2 \rangle &\equiv \sigma_N^2. \end{aligned} \tag{A.2}$$

The brackets denote the expected value for each pixel, however, which is practically estimated by averaging over the line-free pixels, based on the assumption of the noise properties do not change over the pixel region. When the noise is Gaussian, the statistical and correlation properties of the noise is fully quantified by the noise auto correlation function (ACF),

$$\xi(\mathbf{x}_{i,j}) \equiv \langle (N(\mathbf{x}+\mathbf{x}_{i,j}) - \mu)(N(\mathbf{x}) - \mu) \rangle = \langle N(\mathbf{x}+\mathbf{x}_{i,j}) N(\mathbf{x}) \rangle - \mu^2, \tag{A.3}$$

where the expected value is estimated by averaging for the pixel pairs with the relative distance $\mathbf{x}_{i,j} = (i, j)$. For simplicity of later analysis, we assume $\mu = 0$ since the the mean of the noise is much smaller than the standard deviation $\mu \ll \sigma_N$. When $\mu = 0$, noise auto correlation at zero lag equal to the variance of the noise, $\xi(0) = \sigma_N^2$. In the case that the noise is not Gaussian, correlation functions about the higher order term may be required. The noise seems to be approximated well by the Gaussian with mean $\mu \sim 0$ as shown in Figure A.1.

Once the noise ACF is measured, the correlated Gaussian noise at i, j pixel positions

$\mathbf{x}_{i,j}$ in $M \times M$ images can be randomly generated by the joint probability distribution, the probability that $N(\{\mathbf{x}_{i,j}\})$ takes the value in the small intervals $(N_{i,j} + \mathrm{d}N_{i,j})$ given by.

$$\mathrm{d}p = \frac{\mathrm{d}N_{1,1} \cdots \mathrm{d}N_{i,j} \cdots \mathrm{d}N_{M,M}}{(2\pi)^{M^2/2}|\mathbf{C}|^{1/2}} \exp\left(-\frac{1}{2}\Sigma_{a,b,c,d=1}^{M} N_{a,b}\mathbf{C}^{-1}_{a-c,b-d}N_{c,d}\right), \tag{A.4}$$

where $\mathbf{C}^{-1}$ is the inverse of the matrix $\mathbf{C}$ defined by

$$C_{i,j} = \xi(\mathbf{x}_{i,j}) \tag{A.5}$$

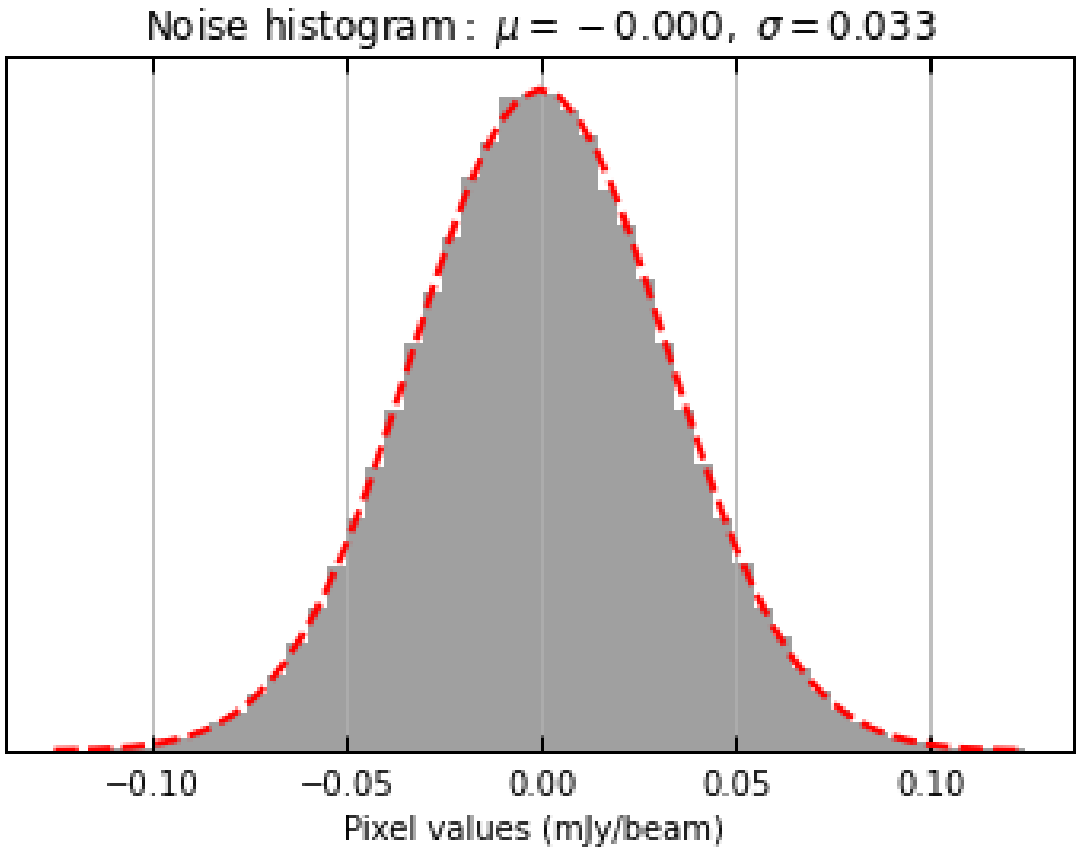

Figure A.1: The illustrative histogram of noise values over emission free regions (Band 7 image of FIR continuum for BRI1335-0417). An arbitrary scaling was set so that the area under the histogram sum to 1.

The noise ACF $\xi(\mathbf{x})$ was measured according to Refregier et al. (2012) by masking the signal from the source and $\xi(\mathbf{x})$ calculating the average of equation A.3 for pairs of pixels separated by vector $\mathbf{x}$. Figure A.2 show the example noise map from ALMA Band 7 image of FIR continuum for BRI 1335-0417 (see Figure A.1 for the histogram of this noise map). The noise map was made by (1) using image region where the primaly beam attenuation >70% and (2) excluding emission region, where the intensity exceeding 4σ and the surrounding pixels within 3 FWHM beam widths. Figure A.3 shows the noise ACF $\xi(\mathbf{x})$ computed from the noise map.

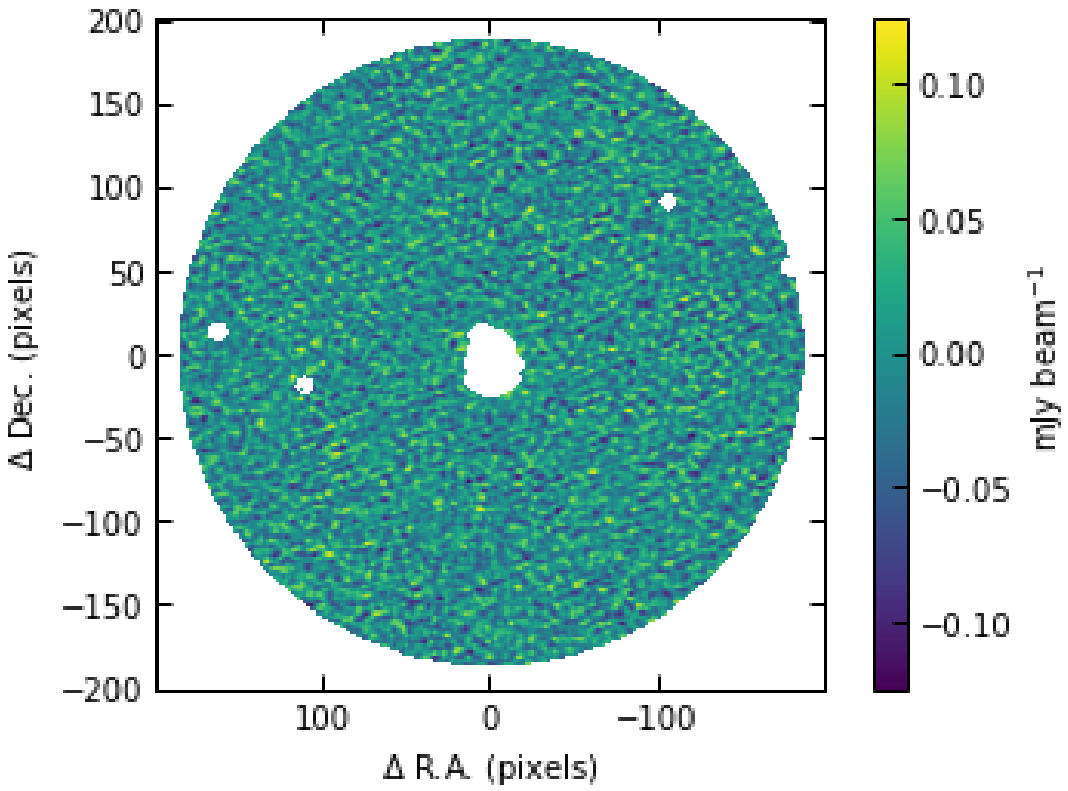

Figure A.2: The noise map from ALMA Band 7 image of FIR continuum for BRI 1335-0417. We excluded the region where the primary beam attenuation greater than 30%. Also to exclude the signal, we removed pixels whose intensity exceed 4σ and the surrounding pixels within 3 beam widths.

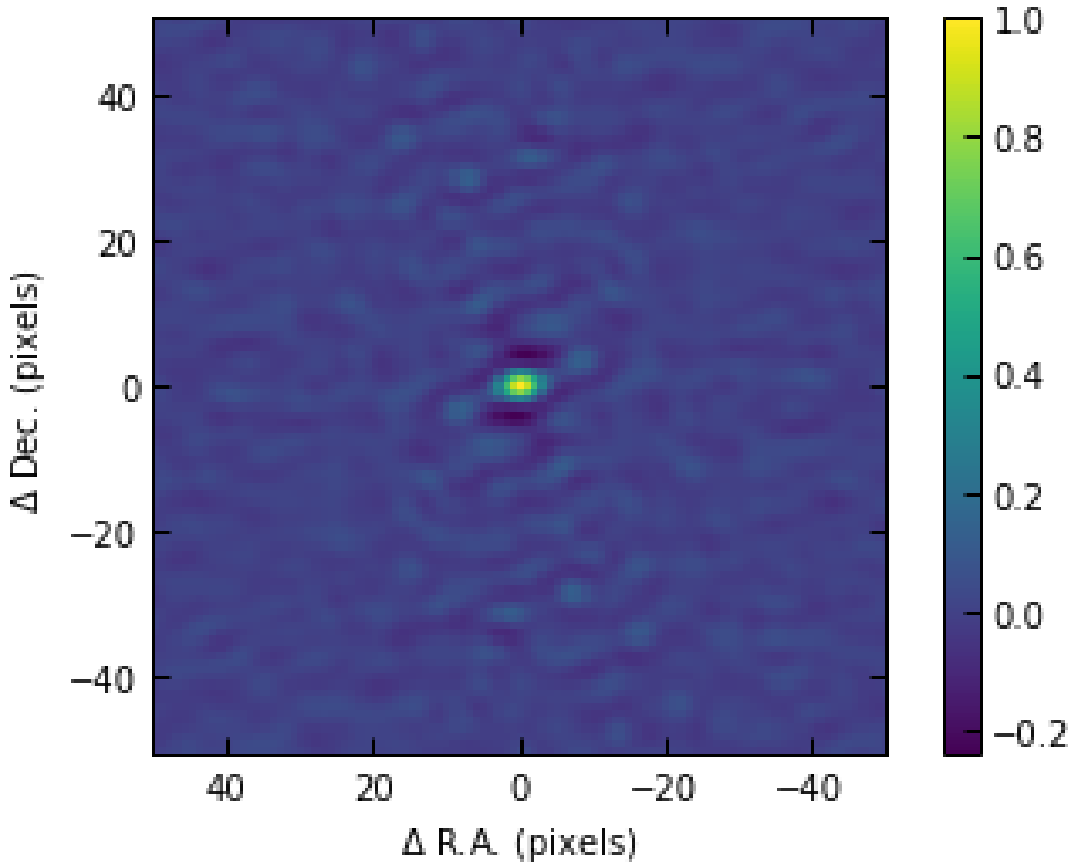

Figure A.3: The noise auto correlation function computed from the noise map in Figure A.2, which is normalized with $\xi(\mathbf{0}) = \sigma_N^2 = 1.07 \times 10^{-9}$ Jy beam^{-1}

A.1.2 Origin of Noise Correlation

A noise from the sky (CMB, background undetected sources, atmospheric emission) is convolved by the synthesized beam in the interferometric observation or by the beam pattern in the single dish observation (Condon, 1997). Noise in the image is sum of the correlated component and the uncorrelated component (the noise associated with the receiver). For simplicity, we ignore the uncorrelated component and considered the total noise in the image is the result of convolution as (Refregier et al., 2012)

$$N(\mathbf{x}) = B * \hat{N} = \sum_{i,j} B(\mathbf{x}_{i,j})\hat{N}(\mathbf{x} + \mathbf{x}_{i,j}) \tag{A.6}$$

where B is the synthesized beam pattern normalized as $\sum_{i,j} B(\mathrm{x}_{i,j}) = 1$ and $\hat{N}$ is intrinsic uncorrelated noise from the sky to be convolved by the synthesized beam.

Then the noise auto correlation is (Refregier et al., 2012),

$$\begin{aligned}
\xi(\mathbf{x}_{i,j}) &= \langle N(\mathbf{x} + \mathbf{x}_{i,j})N(\mathbf{x})\rangle \\
&= \langle \sum_{i',j'} B(\mathbf{x}_{i',j'})\hat{N}(\mathbf{x} + \mathbf{x}_{i,j} + \mathbf{x}_{i',j'}) \sum_{i'',j''} B(\mathbf{x}_{i'',j''}\hat{N}(\mathbf{x} + \mathbf{x}_{i'',j''})\rangle \\
&= \sum_{i',j'} \sum_{i'',j''} B(\mathbf{x}_{i',j'})B(\mathbf{x}_{i'',j''})\langle \hat{N}(\mathbf{x} + \mathbf{x}_{i,j} + \mathbf{x}_{i',j'})\hat{N}(\mathbf{x} + \mathbf{x}_{i'',j''})\rangle \\
&= \sigma_N^2 \alpha(\mathbf{x}),
\end{aligned} \tag{A.7}$$

, with beam auto correlation $\alpha(\mathbf{x}_{i,j})$

$$\alpha(\mathbf{x}_{i,j}) = \sum_{i',j'} B(\mathbf{x}_{i',j'})B(\mathbf{x}_{i,j} + \mathbf{x}_{i',j'}) \tag{A.8}$$

where, for the fourth equality in equation A.7, we used noise ACF property of an uncorrelated noise $\hat{N}$,

$$\xi(\mathbf{x}_{i,j}) = \langle \hat{N}(\mathbf{x} + \mathbf{x}_{i,j})\hat{N}(\mathbf{x})\rangle = \begin{cases} \sigma_N^2 & (\mathbf{x}_{i,j} = 0) \\ 0 & (\mathbf{x}_{i,j} \neq 0) \end{cases} \tag{A.9}$$

ACF of correlated noise is related to that of the beam ACF. As mentioned in Refregier et al. (2012), the noise correlation pattern seen in ACF is similar to the synthesized beam (i.e., point spread function) shown in A.4, suggesting that the noise in the ALMA image is dominated by the correlated component due to the convolution of the synthesized

beam.

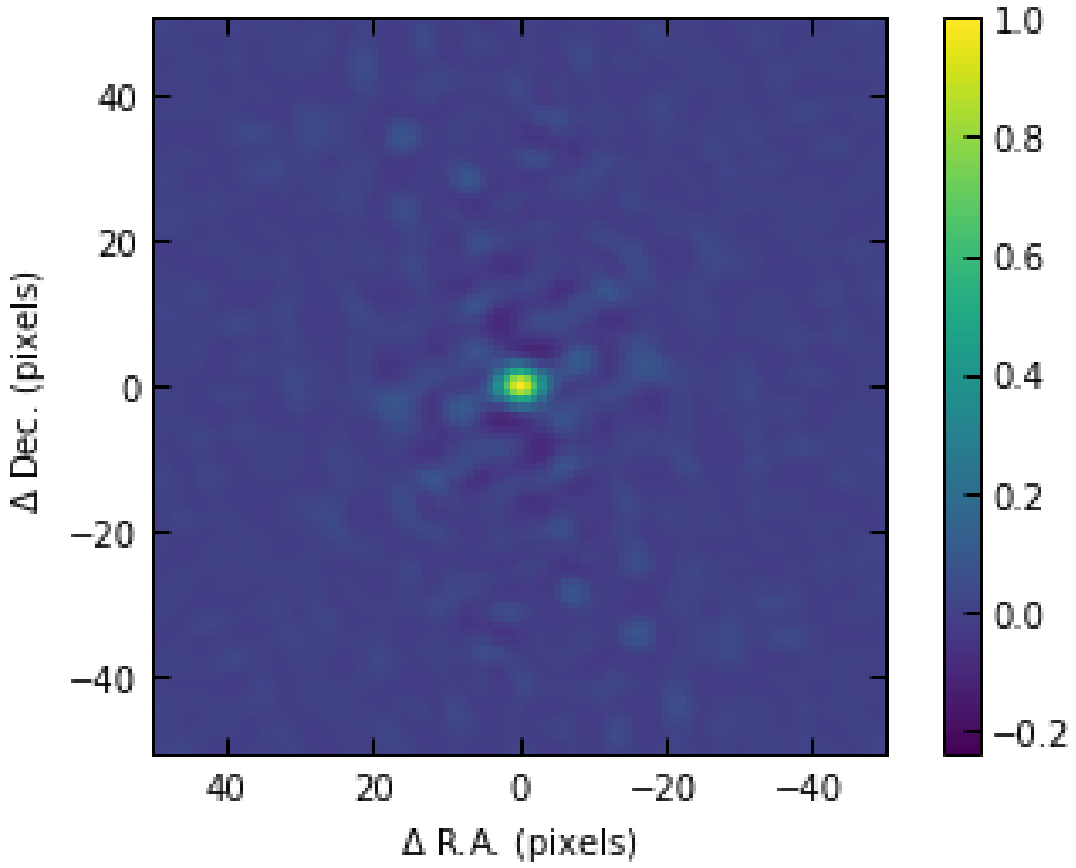

Figure A.4: The point spread function of the observation normalized so that the peak value is 1. Note that the similar pattern can be seen in the noise ACF $\xi(\mathbf{x})$.

A.1.3 Generation of correlated noise from ACF

We have discussed the noise correlation properties which can be fully characterized by the noise ACF. One of the purposes of this appendix is to simulate a correlated noise map which can be used for image analysis, such as Monte Carlo simulation to evaluate the statistical significance and uncertainty in the detection, shape measurement of the source, and etc.

Figure A.5 shows comparison of the noise of the observed data, the noise randomly generated from the measured noise ACF using the joint Gaussian probability distribution (equation A.4; we used the RVS function in the scipy package), and the spatially uncorrelated Gaussian noise, all of which have the same standard deviation. The observed noise and the randomly generated noise using noise ACF are qualitatively similar, which means that noise ACF allows us to capture the correlation properties of noise well. On the other hand, the spatially correlated noise and the spatially uncorrelated noise look completely different, illustrating how dangerous it is to assume naively uncorrelated noise in the image analysis.

To simulate correlated noise from the noise ACF using the joint Gaussian probability distribution is computationally expensive but advantageous that can generate a correlated noise map with proper normalization. For the later analysis, we introduce an efficient way to simulate the correlated noise demonstrated by Britten et al. (2004) for evaluation of X-ray CT scan images of brain. We generated a white Gaussian noise (with arbitral standard deviation) and convolved it with the measured noise ACF to produce the correct noise correlation (i.e., the correct noise power spectrum). We then empirically determined the standard deviation that the white Gaussian noise should have to produce the desired standard deviation of the correlated noise we want to obtain (i.e., the desired normalization of the noise power spectrum).

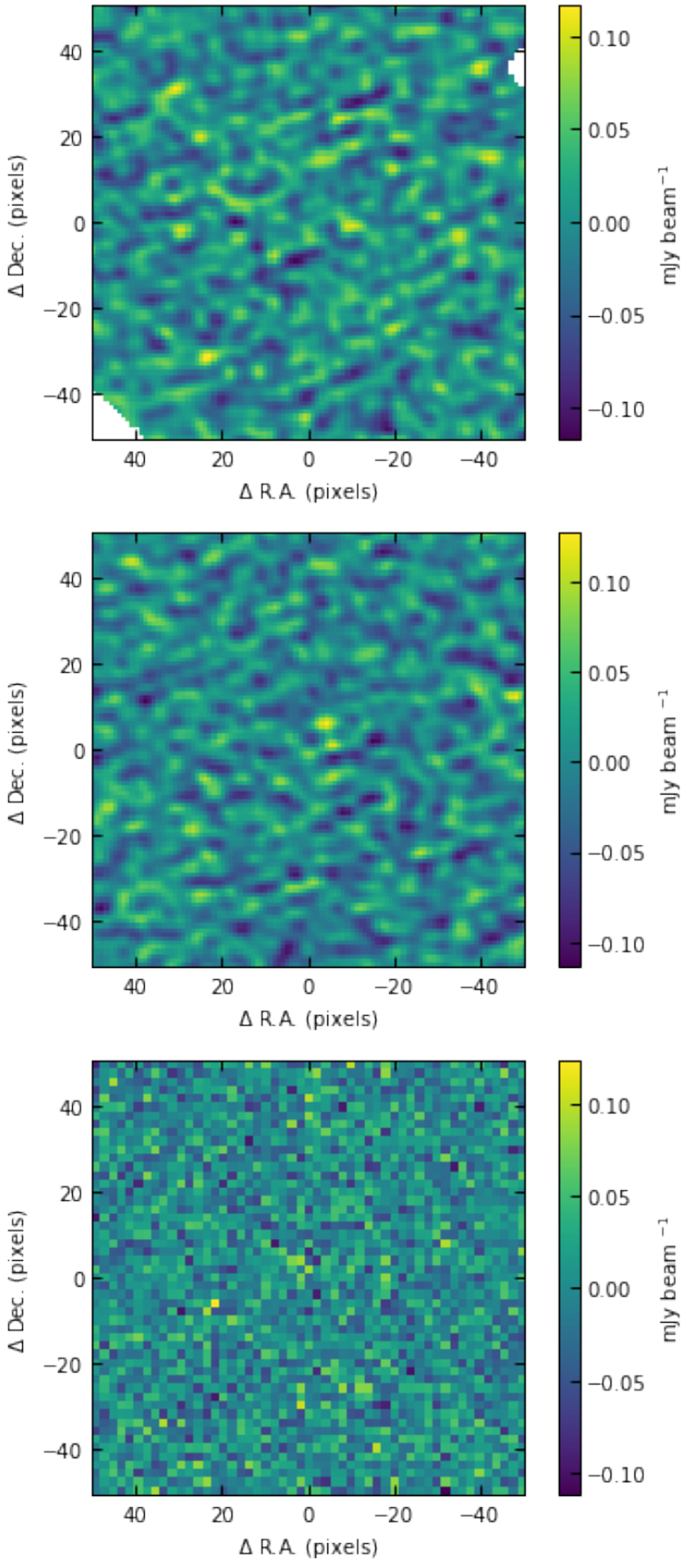

Figure A.5: Noise map in observed data (top), Randomly generated noise map from the measured noise ACF (middle), and uncorrelated noise map (bottom). All of which have the same standard deviation σ_N.

Bibliography

Athanassoula, E. 1992, Monthly Notices of the Royal Astronomical Society, 259, 345, doi: 10.1093/mnras/259.2.345

—. 2005, Monthly Notices of the Royal Astronomical Society, 358, 1477, doi: 10.1111/j.1365-2966.2005.08872.x

Baba, J. 2015, Monthly Notices of the Royal Astronomical Society, 454, 2954, doi: 10.1093/mnras/stv2220

Baba, J., Saitoh, T. R., & Wada, K. 2013, The Astrophysical Journal, 763, 46, doi: 10.1088/0004-637X/763/1/46

Bacon, R., Simien, F., & Monnet, G. 1983, Astronomy and Astrophysics, Vol. 128, p. 405-410 (1983), 128, 405

Bacon, R., Accardo, M., Adjali, L., et al. 2010, 7735, 773508, doi: 10.1117/12.856027

Barnabè, M., Dutton, A. A., Marshall, P. J., et al. 2012, Monthly Notices of the Royal Astronomical Society, 423, 1073, doi: 10.1111/j.1365-2966.2012.20934.x

Barth, A. J., Boizelle, B. D., Darling, J., et al. 2016a, The Astrophysical Journal, 822, L28, doi: 10.3847/2041-8205/822/2/l28

Barth, A. J., Darling, J., Baker, A. J., et al. 2016b, ApJ, 823, 51, doi: 10.3847/0004-637X/823/1/51

Bedregal, A. G., Aragón-Salamanca, A., Merrifield, M. R., & Milvang-Jensen, B. 2006, Monthly Notices of the Royal Astronomical Society, 371, 1912, doi: 10.1111/j.1365-2966.2006.10829.x

Bendinelli, O. 1991, The Astrophysical Journal, 366, 599, doi: 10.1086/169595

Bennett, C. L., Larson, D., Weiland, J. L., & Hinshaw, G. 2014, The Astrophysical Journal, 794, 135, doi: 10.1088/0004-637X/794/2/135

Binney, J., & Tremaine, S. 2008, Galactic Dynamics: Second Edition, by James Binney and Scott Tremaine. ISBN 978-0-691-13026-2 (HB). Published by Princeton University Press, Princeton, NJ USA, 2008.

Blakeslee, J., & John. 2015, HST Proposal id.14219. Cycle 23

Blakeslee, J. P., Jordán, A., Mei, S., et al. 2009, The Astrophysical Journal, 694, 556, doi: 10.1088/0004-637X/694/1/556

Blumenthal, G. R., Faber, S. M., Flores, R., & Primack, J. R. 1986, The Astrophysical Journal, 301, 27, doi: 10.1086/163867

Blumenthal, G. R., Faber, S. M., Primack, J. R., & Rees, M. J. 1984, Nature, 311, 517, doi: 10.1038/311517a0

Boizelle, B. D., Barth, A. J., Darling, J., et al. 2017, The Astrophysical Journal, 845, 170, doi: 10.3847/1538-4357/aa8266

Boizelle, B. D., Barth, A. J., Walsh, J. L., et al. 2019, The Astrophysical Journal, 881, 10, doi: 10.3847/1538-4357/ab2a0a

Bolatto, A. D., Wolfire, M., & Leroy, A. K. 2013, Annual Review of Astronomy and Astrophysics, 51, 207, doi: 10.1146/annurev-astro-082812-140944

Bonaca, A., Hogg, D. W., Price-Whelan, A. M., & Conroy, C. 2019, The Astrophysical Journal, 880, 38, doi: 10.3847/1538-4357/ab2873

Bradley, L., Sipocz, B., Robitaille, T., et al. 2019, Astropy/Photutils: V0.6, Zenodo, doi: 10.5281/zenodo.2533376

Breda, I., Papaderos, P., & Gomes, J. M. 2020, arXiv e-prints, 2006, arXiv:2006.02307

Britten, A. J., Crotty, M., Kiremidjian, H., Grundy, A., & Adam, E. J. 2004, Br J Radiol, 77, 323, doi: 10.1259/bjr/78576048

Bruce, V. A., Dunlop, J. S., McLure, R. J., et al. 2014, Monthly Notices of the Royal Astronomical Society, 444, 1001, doi: 10.1093/mnras/stu1478

Bundy, K., Bershady, M. A., Law, D. R., et al. 2015, The Astrophysical Journal, 798, 7, doi: 10.1088/0004-637X/798/1/7

Burkert, A., Genzel, R., Bouché, N., et al. 2010, The Astrophysical Journal, 725, 2324, doi: 10.1088/0004-637X/725/2/2324

Burkert, A., Förster Schreiber, N. M., Genzel, R., et al. 2016, The Astrophysical Journal, 826, 214, doi: 10.3847/0004-637X/826/2/214

Calistro Rivera, G., Hodge, J. A., Smail, I., et al. 2018, The Astrophysical Journal, 863, 56, doi: 10.3847/1538-4357/aacffa

Cappellari, M. 2002, Monthly Notices of the Royal Astronomical Society, 333, 400, doi: 10.1046/j.1365-8711.2002.05412.x

—. 2008, Monthly Notices of the Royal Astronomical Society, 390, 71, doi: 10.1111/j.1365-2966.2008.13754.x

—. 2017, Mon Not R Astron Soc, 466, 798, doi: 10.1093/mnras/stw3020

—. 2020, Monthly Notices of the Royal Astronomical Society, 494, 4819, doi: 10.1093/mnras/staa959

Cappellari, M., & Copin, Y. 2003, Monthly Notices of the Royal Astronomical Society, 342, 345, doi: 10.1046/j.1365-8711.2003.06541.x

Cappellari, M., & Emsellem, E. 2004, Publications of the Astronomical Society of the Pacific, 116, 138, doi: 10.1086/381875

Cappellari, M., Emsellem, E., Bacon, R., et al. 2007, Monthly Notices of the Royal Astronomical Society, 379, 418, doi: 10.1111/j.1365-2966.2007.11963.x

Cappellari, M., Emsellem, E., Krajnović, D., et al. 2011, Monthly Notices of the Royal Astronomical Society, 413, 813, doi: 10.1111/j.1365-2966.2010.18174.x

Cappellari, M., Scott, N., Alatalo, K., et al. 2013, Monthly Notices of the Royal Astronomical Society, 432, 1709, doi: 10.1093/mnras/stt562

Carilli, C. L., Kohno, K., Kawabe, R., et al. 2002, The Astronomical Journal, 123, 1838, doi: 10.1086/339306

Cautun, M., Benitez-Llambay, A., Deason, A. J., et al. 2019, arXiv e-prints, 1911, arXiv:1911.04557

Condon, J. J. 1997, Publications of the Astronomical Society of the Pacific, 109, 166, doi: 10.1086/133871

Courteau, S., & Dutton, A. A. 2015, The Astrophysical Journal Letters, 801, L20, doi: 10.1088/2041-8205/801/2/L20

Courteau, S., Dutton, A. A., van den Bosch, F. C., et al. 2007, ApJ, 671, 203, doi: 10.1086/522193

Courteau, S., & Rix, H.-W. 1999, The Astrophysical Journal, 513, 561, doi: 10.1086/306872

Courteau, S., Cappellari, M., de Jong, R. S., et al. 2014, Reviews of Modern Physics, 86, 47, doi: 10.1103/RevModPhys.86.47

Croom, S. M., Lawrence, J. S., Bland-Hawthorn, J., et al. 2012, Monthly Notices of the Royal Astronomical Society, 421, 872, doi: 10.1111/j.1365-2966.2011.20365.x

Dame, T. M. 2011, arXiv:1101.1499 [astro-ph]. https://arxiv.org/abs/1101.1499

Davis, B. L., Graham, A. W., & Cameron, E. 2018a, The Astrophysical Journal, 869, 113, doi: 10.3847/1538-4357/aae820

—. 2019, The Astrophysical Journal, 873, 85, doi: 10.3847/1538-4357/aaf3b8

Davis, T. A. 2014, Monthly Notices of the Royal Astronomical Society, 443, 911, doi: 10.1093/mnras/stu1163

Davis, T. A., Bureau, M., Cappellari, M., Sarzi, M., & Blitz, L. 2013a, Nature, 494, 328, doi: 10.1038/nature11819

Davis, T. A., Bureau, M., Onishi, K., et al. 2017, Monthly Notices of the Royal Astronomical Society, 468, 4675, doi: 10.1093/mnras/stw3217

Davis, T. A., & McDermid, R. M. 2017, Monthly Notices of the Royal Astronomical Society, 464, 453, doi: 10.1093/mnras/stw2366

Davis, T. A., Alatalo, K., Bureau, M., et al. 2013b, Monthly Notices of the Royal Astronomical Society, 429, 534, doi: 10.1093/mnras/sts353

Davis, T. A., Bureau, M., Onishi, K., et al. 2018b, Mon Not R Astron Soc, 473, 3818, doi: 10.1093/mnras/stx2600

Dawson, S., McCrady, N., Stern, D., et al. 2003, The Astronomical Journal, 125, 1236, doi: 10.1086/367792

De Breuck, C., Maiolino, R., Caselli, P., et al. 2011, Astronomy and Astrophysics, 530, L8, doi: 10.1051/0004-6361/201116868

de Vaucouleurs, G. 1948, Annales d'Astrophysique, 11, 247

de Zeeuw, P. T., Evans, N. W., & Schwarzschild, M. 1996, Monthly Notices of the Royal Astronomical Society, 280, 903, doi: 10.1093/mnras/280.3.903

de Zeeuw, P. T., Bureau, M., Emsellem, E., et al. 2002, Monthly Notices of the Royal Astronomical Society, 329, 513, doi: 10.1046/j.1365-8711.2002.05059.x

Decarli, R., Walter, F., Venemans, B. P., et al. 2018, ApJ, 854, 97, doi: 10.3847/1538-4357/aaa5aa

Dekel, A., & Burkert, A. 2014, Monthly Notices of the Royal Astronomical Society, 438, 1870, doi: 10.1093/mnras/stt2331

Dekel, A., Birnboim, Y., Engel, G., et al. 2009, Nature, 457, 451, doi: 10.1038/nature07648

Dieleman, S., Willett, K. W., & Dambre, J. 2015, Monthly Notices of the Royal Astronomical Society, 450, 1441, doi: 10.1093/mnras/stv632

Dobbs, C., & Baba, J. 2014, Publications of the Astronomical Society of Australia, 31, e035, doi: 10.1017/pasa.2014.31

Driver, S. P., Allen, P. D., Graham, A. W., et al. 2006, Monthly Notices of the Royal Astronomical Society, 368, 414, doi: 10.1111/j.1365-2966.2006.10126.x

Du, M., Ho, L. C., Debattista, V. P., et al. 2020, The Astrophysical Journal, 895, 139, doi: 10.3847/1538-4357/ab8fa8

Du, M., Ho, L. C., Zhao, D., et al. 2019, The Astrophysical Journal, 884, 129, doi: 10.3847/1538-4357/ab43cc

Dudzevičiūtė, U., Smail, I., Swinbank, A. M., et al. 2020, Monthly Notices of the Royal Astronomical Society, 494, 3828, doi: 10.1093/mnras/staa769

Dutton, A. A., & Macciò, A. V. 2014, Monthly Notices of the Royal Astronomical Society, 441, 3359, doi: 10.1093/mnras/stu742

Dutton, A. A., van den Bosch, F. C., Dekel, A., & Courteau, S. 2007, ApJ, 654, 27, doi: 10.1086/509314

Dutton, A. A., Marshall, P. J., Koo, D. C., et al. 2011, Monthly Notices of the Royal Astronomical Society, 417, 1621, doi: 10.1111/j.1365-2966.2011.18706.x

Dutton, A. A., Treu, T., Brewer, B. J., et al. 2013, Monthly Notices of the Royal Astronomical Society, 428, 3183, doi: 10.1093/mnras/sts262

Dye, S., Eales, S. A., Gomez, H. L., et al. 2021, Monthly Notices of the Royal Astronomical Society, doi: 10.1093/mnras/stab3569

Efstathiou, G., Lake, G., & Negroponte, J. 1982, Monthly Notices of the Royal Astronomical Society, 199, 1069, doi: 10.1093/mnras/199.4.1069

Emsellem, E., Monnet, G., & Bacon, R. 1994a, Astronomy and Astrophysics, Vol. 285, p.723-738 (1994), 285, 723

—. 1994b, Astronomy and Astrophysics, Vol. 285, p.723-738 (1994), 285, 723

Erwin, P., Beckman, J. E., & Pohlen, M. 2005, The Astrophysical Journal, 626, L81, doi: 10.1086/431739

Everall, A., Evans, N. W., Belokurov, V., & Schönrich, R. 2019, Monthly Notices of the Royal Astronomical Society, 489, 910, doi: 10.1093/mnras/stz2217

Fabian, A. C. 2012, Annual Review of Astronomy and Astrophysics, vol. 50, p.455-489, 50, 455, doi: 10.1146/annurev-astro-081811-125521

Ferguson, H. C. 1989, The Astronomical Journal, 98, 367, doi: 10.1086/115152

Ferkinhoff, C., Brisbin, D., Parshley, S., et al. 2013, ApJ, 780, 142, doi: 10.1088/0004-637X/780/2/142

Ferrarese, L., & Merritt, D. 2000, The Astrophysical Journal Letters, 539, L9, doi: 10.1086/312838

Foreman-Mackey, D., Hogg, D. W., Lang, D., & Goodman, J. 2013, Publications of the Astronomical Society of the Pacific, 125, 306, doi: 10.1086/670067

Förster Schreiber, N. M., Genzel, R., Bouché, N., et al. 2009, The Astrophysical Journal, 706, 1364, doi: 10.1088/0004-637X/706/2/1364

Franx, M. 1988, Monthly Notices of the Royal Astronomical Society, 231, 285, doi: 10.1093/mnras/231.2.285

Freeman, K. C. 1970, The Astrophysical Journal, 160, 811, doi: 10.1086/150474

Fujii, M. S., Bédorf, J., Baba, J., & Portegies Zwart, S. 2018, Monthly Notices of the Royal Astronomical Society, 477, 1451, doi: 10.1093/mnras/sty711

Fujimoto, S., Ouchi, M., Ferrara, A., et al. 2019, The Astrophysical Journal, 887, 107, doi: 10.3847/1538-4357/ab480f

Fujimoto, S., Silverman, J. D., Bethermin, M., et al. 2020, The Astrophysical Journal, 900, 1, doi: 10.3847/1538-4357/ab94b3

Gadotti, D. A. 2009, Monthly Notices of the Royal Astronomical Society, 393, 1531, doi: 10.1111/j.1365-2966.2008.14257.x

Gaia Collaboration. 2018, VizieR Online Data Catalog, I/345

Gall, C., Hjorth, J., & Andersen, A. C. 2011, Astron Astrophys Rev, 19, 43, doi: 10.1007/s00159-011-0043-7

Gao, H., & Ho, L. C. 2017, The Astrophysical Journal, 845, 114, doi: 10.3847/1538-4357/aa7da4

Genzel, R., Förster Schreiber, N. M., Lang, P., et al. 2014, The Astrophysical Journal, 785, 75, doi: 10.1088/0004-637X/785/1/75

Genzel, R., Schreiber, N. M., Übler, H., et al. 2017, Nature, 543, 397, doi: 10.1038/nature21685

Gerhard, O. E., & Binney, J. J. 1996, Monthly Notices of the Royal Astronomical Society, 279, 993, doi: 10.1093/mnras/279.3.993

Goldreich, P., & Lynden-Bell, D. 1965, Monthly Notices of the Royal Astronomical Society, 130, 97, doi: 10.1093/mnras/130.2.97

Goodman, J., & Weare, J. 2010, Commun. Appl. Math. Comput. Sci., 5, 65, doi: 10.2140/camcos.2010.5.65

Graham, A. W., & Driver, S. P. 2005, Publications of the Astronomical Society of Australia, 22, 118, doi: 10.1071/AS05001

Green, A. W., Glazebrook, K., McGregor, P. J., et al. 2010, Nature, 467, 684, doi: 10.1038/nature09452

Guilloteau, S., Omont, A., McMahon, R. G., Cox, P., & Petitjean, P. 1997, Astronomy and Astrophysics, 328, L1

Gullberg, B., Swinbank, A. M., Smail, I., et al. 2018, ApJ, 859, 12, doi: 10.3847/1538-4357/aabe8c

Hagen, J. H. J., Helmi, A., de Zeeuw, P. T., & Posti, L. 2019, Astronomy and Astrophysics, 629, A70, doi: 10.1051/0004-6361/201935264

Hattori, K., Valluri, M., & Vasiliev, E. 2020, Action-Based Distribution Function Modelling for Constraining the Shape of the Galactic Dark Matter Halo

Hodge, J. A., Smail, I., Walter, F., et al. 2019, The Astrophysical Journal, 876, 130, doi: 10.3847/1538-4357/ab1846

Hopkins, P. F., Cox, T. J., Younger, J. D., & Hernquist, L. 2009, The Astrophysical Journal, 691, 1168, doi: 10.1088/0004-637X/691/2/1168

Hopkins, P. F., & Quataert, E. 2010, Monthly Notices of the Royal Astronomical Society, 407, 1529, doi: 10.1111/j.1365-2966.2010.17064.x

Hubble, E. P. 1936, Yale University Press ISBN 9780300025002

Iguchi, S. 2005, Publications of the Astronomical Society of Japan, 57, 643, doi: 10.1093/pasj/57.4.643

Inoue, S., Dekel, A., Mandelker, N., et al. 2016, Monthly Notices of the Royal Astronomical Society, 456, 2052, doi: 10.1093/mnras/stv2793

Iodice, E., Spavone, M., Capaccioli, M., et al. 2019, Astronomy and Astrophysics, 623, A1, doi: 10.1051/0004-6361/201833741

Izumi, T., Onoue, M., Matsuoka, Y., et al. 2019, Publications of the Astronomical Society of Japan, 71, 111, doi: 10.1093/pasj/psz096

Jahnke, K., & Macciò, A. V. 2011, The Astrophysical Journal, 734, 92, doi: 10.1088/0004-637X/734/2/92

Jeans, J. H. 1922, Monthly Notices of the Royal Astronomical Society, 82, 122, doi: 10.1093/mnras/82.3.122

Jones, G. C., Carilli, C. L., Momjian, E., et al. 2016, ApJ, 830, 63, doi: 10.3847/0004-637X/830/2/63

Jones, G. C., Carilli, C. L., Shao, Y., et al. 2017, The Astrophysical Journal, 850, 180, doi: 10.3847/1538-4357/aa8df2

Kalnajs, A. J. 1975, La Dynamique des galaxies spirales, 103

Katz, N., & Gunn, J. E. 1991, The Astrophysical Journal, 377, 365, doi: 10.1086/170367

Kent, S. M. 1986, The Astronomical Journal, 91, 1301, doi: 10.1086/114106

Kochanek, C. S., & Rybicki, G. B. 1996, Monthly Notices of the Royal Astronomical Society, 280, 1257, doi: 10.1093/mnras/280.4.1257

Kohandel, M., Pallottini, A., Ferrara, A., et al. 2019, Monthly Notices of the Royal Astronomical Society, 487, 3007, doi: 10.1093/mnras/stz1486

Kormendy, J. 1982, Saas-Fee Advanced Course, 12, 115

Kormendy, J., & Ho, L. C. 2013, Annual Review of Astronomy and Astrophysics, 51, 511, doi: 10.1146/annurev-astro-082708-101811

Kormendy, J., & Kennicutt, Jr., R. C. 2004, Annual Review of Astronomy and Astrophysics, 42, 603, doi: 10.1146/annurev.astro.42.053102.134024

Krajnović, D., Cappellari, M., de Zeeuw, P. T., & Copin, Y. 2006, Monthly Notices of the Royal Astronomical Society, 366, 787, doi: 10.1111/j.1365-2966.2005.09902.x

Lang, P., Wuyts, S., Somerville, R. S., et al. 2014, The Astrophysical Journal, 788, 11, doi: 10.1088/0004-637X/788/1/11

Lang, P., Förster Schreiber, N. M., Genzel, R., et al. 2017, The Astrophysical Journal, 840, 92, doi: 10.3847/1538-4357/aa6d82

Lange, R., Moffett, A. J., Driver, S. P., et al. 2016, Monthly Notices of the Royal Astronomical Society, 462, 1470, doi: 10.1093/mnras/stw1495

Law, D. R., Shapley, A. E., Steidel, C. C., et al. 2012, Nature, 487, 338, doi: 10.1038/nature11256

Lelli, F., Teodoro, E. M. D., Fraternali, F., et al. 2021, Science, 371, 713, doi: 10.1126/science.abc1893

Lin, C. C., & Shu, F. H. 1964, The Astrophysical Journal, 140, 646, doi: 10.1086/147955

Lipka, M., & Thomas, J. 2021, Monthly Notices of the Royal Astronomical Society, 504, 4599, doi: 10.1093/mnras/stab1092

Longair, M. S. 2008, Galaxy Formation

Madau, P., & Dickinson, M. 2014, Annual Review of Astronomy and Astrophysics, 52, 415, doi: 10.1146/annurev-astro-081811-125615

Magorrian, J. 2006, Monthly Notices of the Royal Astronomical Society, 373, 425, doi: 10.1111/j.1365-2966.2006.11054.x

Makarov, D., Prugniel, P., Terekhova, N., Courtois, H., & Vauglin, I. 2014, Astronomy and Astrophysics, 570, A13, doi: 10.1051/0004-6361/201423496

Martinsson, T. P. K., Verheijen, M. A. W., Westfall, K. B., et al. 2013a, A&A, 557, A131, doi: 10.1051/0004-6361/201321390

—. 2013b, Astronomy and Astrophysics, 557, A130, doi: 10.1051/0004-6361/201220515

Mashchenko, S., Wadsley, J., & Couchman, H. M. P. 2008, Science, 319, 174, doi: 10.1126/science.1148666

McAlpine, S., Smail, I., Bower, R. G., et al. 2019, Monthly Notices of the Royal Astronomical Society, 488, 2440, doi: 10.1093/mnras/stz1692

McMullin, J. P., Waters, B., Schiebel, D., Young, W., & Golap, K. 2007, ASPC, 376, 127

Mejía-Restrepo, J. E., Lira, P., Netzer, H., Trakhtenbrot, B., & Capellupo, D. M. 2018, Nature Astronomy, 2, 63, doi: 10.1038/s41550-017-0305-z

Mitsuhashi, I., Matsuda, Y., Smail, I., et al. 2021, The Astrophysical Journal, 907, 122, doi: 10.3847/1538-4357/abcc72

Mitzkus, M., Cappellari, M., & Walcher, C. J. 2017, Monthly Notices of the Royal Astronomical Society, 464, 4789, doi: 10.1093/mnras/stw2677

Mizukoshi, S., Kohno, K., Egusa, F., et al. 2021, The Astrophysical Journal, 917, 94, doi: 10.3847/1538-4357/ac01cc

Mo, H., van den Bosch, F. C., & White, S. 2010, Galaxy Formation and Evolution

Mogotsi, K. M., de Blok, W. J. G., Caldu-Primo, A., et al. 2015, The Astronomical Journal, 151, 15, doi: 10.3847/0004-6256/151/1/15

Monnet, G., Bacon, R., & Emsellem, E. 1992, Astronomy and Astrophysics, Vol. 253, p. 366-373 (1992), 253, 366

Narayanan, D., Krumholz, M. R., Ostriker, E. C., & Hernquist, L. 2012, Monthly Notices of the Royal Astronomical Society, 421, 3127, doi: 10.1111/j.1365-2966.2012.20536.x

Navarro, J. F., Eke, V. R., & Frenk, C. S. 1996, Monthly Notices of the Royal Astronomical Society, 283, L72, doi: 10.1093/mnras/283.3.L72

Navarro, J. F., Frenk, C. S., & White, S. D. M. 1997, The Astrophysical Journal, 490, 493, doi: 10.1086/304888

Neeleman, M., Prochaska, J. X., Kanekar, N., & Rafelski, M. 2020, Nature, 581, 269, doi: 10.1038/s41586-020-2276-y

Noordermeer, E. 2008, Monthly Notices of the Royal Astronomical Society, 385, 1359, doi: 10.1111/j.1365-2966.2008.12837.x

Noordermeer, E., Merrifield, M. R., & Aragón-Salamanca, A. 2008, Monthly Notices of the Royal Astronomical Society, 388, 1381, doi: 10.1111/j.1365-2966.2008.13487.x

North, E. V., Davis, T. A., Bureau, M., et al. 2019, Monthly Notices of the Royal Astronomical Society, 490, 319, doi: 10.1093/mnras/stz2598

Oh, S., Colless, M., Barsanti, S., et al. 2020, Mon Not R Astron Soc, 495, 4638, doi: 10.1093/mnras/staa1330

Onishi, K., Iguchi, S., Davis, T. A., et al. 2017, Monthly Notices of the Royal Astronomical Society, 468, 4663, doi: 10.1093/mnras/stx631

Onishi, K., Iguchi, S., Sheth, K., & Kohno, K. 2015, The Astrophysical Journal, 806, 39, doi: 10.1088/0004-637X/806/1/39

Ostriker, J. P., & Peebles, P. J. E. 1973, The Astrophysical Journal, 186, 467, doi: 10.1086/152513

Ouchi, M., Harikane, Y., Shibuya, T., et al. 2018, Publications of the Astronomical Society of Japan, 70, S13, doi: 10.1093/pasj/psx074

Peebles, P. J. E. 1982, The Astrophysical Journal, 263, L1, doi: 10.1086/183911

Peng, C. Y., Ho, L. C., Impey, C. D., & Rix, H.-W. 2010, The Astronomical Journal, 139, 2097, doi: 10.1088/0004-6256/139/6/2097

Pineda, J. L., Langer, W. D., Velusamy, T., & Goldsmith, P. F. 2013, Astronomy and Astrophysics, 554, A103, doi: 10.1051/0004-6361/201321188

Pinkney, J., Gultekin, K., & Gebhardt, K. 2020, 235, 283.04

Pontzen, A., & Governato, F. 2012, Monthly Notices of the Royal Astronomical Society, 421, 3464, doi: 10.1111/j.1365-2966.2012.20571.x

Pota, V., Forbes, D. A., Romanowsky, A. J., et al. 2013, Monthly Notices of the Royal Astronomical Society, 428, 389, doi: 10.1093/mnras/sts029

Puerari, I., & Dottori, H. A. 1992, Astronomy and Astrophysics Supplement Series, 93, 469

Refregier, A., Kacprzak, T., Amara, A., Bridle, S., & Rowe, B. 2012, Monthly Notices of the Royal Astronomical Society, 425, 1951, doi: 10.1111/j.1365-2966.2012.21483.x

Remijan, A., Biggs, A., Cortes, P., et al. 2019, doi: 10.5281/zenodo.4511522

Ren, J., Zheng, X. Z., Valls-Gabaud, D., et al. 2020, Monthly Notices of the Royal Astronomical Society, 499, 3399, doi: 10.1093/mnras/staa2985

Riechers, D. A., Walter, F., Carilli, C. L., Bertoldi, F., & Momjian, E. 2008, The Astrophysical Journal Letters, 686, L9, doi: 10.1086/592834

Rizzo, F., Vegetti, S., Powell, D., et al. 2020, Nature, 584, 201, doi: 10.1038/s41586-020-2572-6

Roberts, M. S., & Haynes, M. P. 1994, Annual Review of Astronomy and Astrophysics, 32, 115, doi: 10.1146/annurev.aa.32.090194.000555

Rubin, V. C., Ford, Jr., W. K., & Thonnard, N. 1978, The Astrophysical Journal, 225, L107, doi: 10.1086/182804

—. 1980, The Astrophysical Journal, 238, 471, doi: 10.1086/158003

Rybicki, G. B. 1987, 127, 397, doi: 10.1007/978-94-009-3971-4_41

Saglia, R. P., Opitsch, M., Erwin, P., et al. 2016, The Astrophysical Journal, 818, 47, doi: 10.3847/0004-637X/818/1/47

Sánchez, S. F., Kennicutt, R. C., Gil de Paz, A., et al. 2012, Astronomy and Astrophysics, 538, A8, doi: 10.1051/0004-6361/201117353

Sarzi, M., Iodice, E., Coccato, L., et al. 2018, Astronomy and Astrophysics, 616, A121, doi: 10.1051/0004-6361/201833137

Schulze, A., & Wisotzki, L. 2014, Monthly Notices of the Royal Astronomical Society, 438, 3422, doi: 10.1093/mnras/stt2457

Schwarzschild, M. 1979, The Astrophysical Journal, 232, 236, doi: 10.1086/157282

Seigar, M. S., Bullock, J. S., Barth, A. J., & Ho, L. C. 2006, ApJ, 645, 1012, doi: 10.1086/504463

Sersic, J. L. 1968, Cordoba

Shapiro, K. L., Genzel, R., Förster Schreiber, N. M., et al. 2008, The Astrophysical Journal, 682, 231, doi: 10.1086/587133

Shields, G. A., Menezes, K. L., Massart, C. A., & Vanden Bout, P. 2006, The Astrophysical Journal, 641, 683, doi: 10.1086/500542

Silk, J. 1968, The Astrophysical Journal, 151, 459, doi: 10.1086/149449

Smith, M. D., Bureau, M., Davis, T. A., et al. 2019, Monthly Notices of the Royal Astronomical Society, 485, 4359, doi: 10.1093/mnras/stz625

Sofue, Y., Honma, M., & Omodaka, T. 2009, Publications of the Astronomical Society of Japan, 61, 227, doi: 10.1093/pasj/61.2.227

Sofue, Y., Koda, J., Nakanishi, H., & Onodera, S. 2003, Publications of the Astronomical Society of Japan, 55, 59, doi: 10.1093/pasj/55.1.59

Somerville, R. S., & Davé, R. 2015, Annual Review of Astronomy and Astrophysics, 53, 51, doi: 10.1146/annurev-astro-082812-140951

Tabor, M., Merrifield, M., Aragón-Salamanca, A., et al. 2017, Monthly Notices of the Royal Astronomical Society, 466, 2024, doi: 10.1093/mnras/stw3183

Tabor, M., Merrifield, M., Aragon-Salamanca, A., et al. 2019, 15, 1

Tacchella, S., Carollo, C. M., Renzini, A., et al. 2015, Science, 348, 314, doi: 10.1126/science.1261094

Tacconi, L. J., Genzel, R., & Sternberg, A. 2020, Annual Review of Astronomy and Astrophysics, 58, 157, doi: 10.1146/annurev-astro-082812-141034

Tadaki, K., Iono, D., Yun, M. S., et al. 2018, Nature, 560, 613, doi: 10.1038/s41586-018-0443-1

Taranu, D. S., Obreschkow, D., Dubinski, J. J., et al. 2017, The Astrophysical Journal, 850, 70, doi: 10.3847/1538-4357/aa9221

Thater, S., Krajnović, D., Nguyen, D. D., Iguchi, S., & Weilbacher, P. M. 2020, 353, 199, doi: 10.1017/S1743921319008445

Toft, S., Smolčić, V., Magnelli, B., et al. 2014, The Astrophysical Journal, 782, 68, doi: 10.1088/0004-637X/782/2/68

Toomre, A. 1964, The Astrophysical Journal, 139, 1217, doi: 10.1086/147861

Tsukui, T., & Iguchi, S. 2021, Science, 372, 1201, doi: 10.1126/science.abe9680

van den Bergh, S. 1998, Galaxy Morphology and Classification

Van Den Bosch, R. C., Van De Ven, G., Verolme, E. K., Cappellari, M., & De Zeeuw, P. T. 2008, Monthly Notices of the Royal Astronomical Society, 385, 647, doi: 10.1111/j.1365-2966.2008.12874.x

Van Den Bosch, R. C. E., & Van De Ven, G. 2009, Mon Not R Astron Soc, 398, 1117, doi: 10.1111/j.1365-2966.2009.15177.x

van der Kruit, P. C., & Allen, R. J. 1978, Annual Review of Astronomy and Astrophysics, 16, 103, doi: 10.1146/annurev.aa.16.090178.000535

van Dokkum, P., Conroy, C., Villaume, A., Brodie, J., & Romanowsky, A. J. 2017, The Astrophysical Journal, 841, 68, doi: 10.3847/1538-4357/aa7135

Vasiliev, E., & Valluri, M. 2019, Proc. IAU, 14, 176, doi: 10.1017/S1743921319008706

Vazdekis, A., Ricciardelli, E., Cenarro, A. J., et al. 2012, Monthly Notices of the Royal Astronomical Society, 424, 157, doi: 10.1111/j.1365-2966.2012.21179.x

Vega-Ferrero, J., Domínguez Sánchez, H., Bernardi, M., et al. 2021, Monthly Notices of the Royal Astronomical Society, 506, 1927, doi: 10.1093/mnras/stab594

Wada, K., & Habe, A. 1992, Monthly Notices of the Royal Astronomical Society, 258, 82, doi: 10.1093/mnras/258.1.82

Wagg, J., Carilli, C. L., Wilner, D. J., et al. 2010, Astronomy and Astrophysics, 519, L1, doi: 10.1051/0004-6361/201015424

Wagg, J., Carilli, C. L., Aravena, M., et al. 2014, The Astrophysical Journal, 783, 71, doi: 10.1088/0004-637X/783/2/71

Walsh, J. L., Barth, A. J., Ho, L. C., & Sarzi, M. 2013, ApJ, 770, 86, doi: 10.1088/0004-637X/770/2/86

Walsh, J. L., van den Bosch, R. C. E., Barth, A. J., & Sarzi, M. 2012, The Astrophysical Journal, 753, 79, doi: 10.1088/0004-637X/753/1/79

Wasserman, A., Romanowsky, A. J., Brodie, J., et al. 2018, The Astrophysical Journal, 863, 130, doi: 10.3847/1538-4357/aad236

Wegg, C., Gerhard, O., & Bieth, M. 2019, Monthly Notices of the Royal Astronomical Society, 485, 3296, doi: 10.1093/mnras/stz572

Williams, M. J., Bureau, M., & Cappellari, M. 2009, Monthly Notices of the Royal Astronomical Society, 400, 1665, doi: 10.1111/j.1365-2966.2009.15582.x

Willmer, C. N. A. 2018, The Astrophysical Journal Supplement Series, 236, 47, doi: 10.3847/1538-4365/aabfdf

Wisnioski, E., Förster Schreiber, N. M., Wuyts, S., et al. 2015, The Astrophysical Journal, 799, 209, doi: 10.1088/0004-637X/799/2/209

Wuyts, S., Förster Schreiber, N. M., Wisnioski, E., et al. 2016, The Astrophysical Journal, 831, 149, doi: 10.3847/0004-637X/831/2/149

Young, L. M., Scott, N., Serra, P., et al. 2014, Monthly Notices of the Royal Astronomical Society, 444, 3408, doi: 10.1093/mnras/stt2474

Yuan, T., Richard, J., Gupta, A., et al. 2017, The Astrophysical Journal, 850, 61, doi: 10.3847/1538-4357/aa951d

Zanella, A., Daddi, E., Magdis, G., et al. 2018, Monthly Notices of the Royal Astronomical Society, 481, 1976, doi: 10.1093/mnras/sty2394

Zeng, G., Wang, L., & Gao, L. 2021, Monthly Notices of the Royal Astronomical Society, 507, 3301, doi: 10.1093/mnras/stab2294

Zhao, H. 1996, Monthly Notices of the Royal Astronomical Society, 278, 488, doi: 10.1093/mnras/278.2.488

Zhu, L., van de Ven, G., Méndez-Abreu, J., & Obreja, A. 2018a, Monthly Notices of the Royal Astronomical Society, 479, 945, doi: 10.1093/mnras/sty1521

Zhu, L., Romanowsky, A. J., van de Ven, G., et al. 2016, Mon Not R Astron Soc, 462, 4001, doi: 10.1093/mnras/stw1931

Zhu, L., Ven, G. V. D., Bosch, R. V. D., et al. 2018b, Nature Astronomy, 2, 233, doi: 10.1038/s41550-017-0348-1

Zolotov, A., Dekel, A., Mandelker, N., et al. 2015, Monthly Notices of the Royal Astronomical Society, 450, 2327, doi: 10.1093/mnras/stv740

Zwicky, F. 1933, Helvetica Physica Acta, 6, 110